EFFECT OF DEFORMATION ON CORROSION OF Al-Mn ALLOYS

By

JUTATIP NAMAHOOT

A thesis submitted to
The University of Birmingham
for the degree of
DOCTOR OF PHILOSOPHY

Metallurgy and Materials
School of Engineering
The University of Birmingham
September 2004

ABSTRACT

Wrought Al-Mn alloys can develop a thin deformed layer on the surface as a result of hot and cold rolling. Subsequent heat-treatment precipitates fine secondary intermetallic particles which effect corrosion susceptibility. This work focuses on the effect of surface preparation and deformation on the electrochemical behaviour of Al-Mn alloys.

The first part of the work investigated the effect of surface preparation such as mechanical grinding and polishing, alkaline etching and desmutting, and nitric acid treatment on electrochemical behaviour of an Al-1Mn-0.4Fe-0.3Si model alloy. Different surface preparations of this alloy show different electrochemical behaviour.

In the second part of the work, the electrochemical reactivity of the surface layers of commercial rolled AA3005 sheet was investigated by profiling through the surface with GDOES (glow discharge optical emission spectroscopy). The microstructure and electrochemical reactivity was examined at different depths in order to compare the behaviour of the surface layers with that of the bulk alloy.

In order to understand the role of deformation on corrosion behaviour of Al-Mn alloy, an Al-1Mn-0.4Fe-0.3Si model alloy was deformed by uniaxial compression and equal channel angular extrusion (ECAE) and followed by annealing. It was found that deformation is likely to have two effects on the surface of Al-Mn alloy. One effect is to cause the precipitation of particles that act as local cathodes and pit initiation sites. The other effect is that formation of precipitates will deplete the adjacent matrix in solute, making it more susceptible to dissolution.

ACKNOWLEDGEMENTS

I would like to thank my supervisor, Dr Alison J. Davenport for continued encouragement and very good supervision over this project.

I would like to thank Dr Rajan Ambat for his invaluable supervision, experimental help and discussion.

I would like to thank Dr Geoff M. Scamans, Dr Andreas Afseth, Calum Campbell and Gavin Brown in Alcan Laboratory, Banbury for helping on GDOES, Wyko, TEP measurements, providing materials and discussion.

I would like to thank Dr P.B. Prangnell and Dr Pete Apps of the Manchester Materials Science Centre, for ECAE.

I would like to thank for the help from Chris Hardy, Dr Mark Ashworth, Dave Price, John Farmer, Paul Stanley at the Department of Metallurgy and Materials for Auger Surface Depth profile analysis, uniaxial compression, GDOES, and EBSD.

I would like to thank Dr Brian Connolly for help on providing some useful books using in literature review.

I would like to thank the help from Sumathy Arumuganathar and Manthana Jariyaboon for FEG ESEM.

I would like to thank all the students of the electrochemical group for their experimental help and the staff in this school for their kind help.

I would like to thank the Royal Thai government for sponsoring this project and for financial support.

Finally, I would like to thank my parent, my brothers and my grand parent for their grateful kind support throughout the past four years.

TABLE OF CONTENTS

Chapter 1 Introduction

Al-3XXX wrought alloys are widely used for architectural applications, cooking utensils, bodies of beverage cans, packaging, chemical equipment, pressure vessels, and heat exchangers [1-6]. These products are usually used in sheet form. Both the hot and cold rolling that are used in aluminium alloy sheet production result in a high level of enhanced surface shear deformation. The hot rolling process, or the subsequent heat treatment in the case of cold rolling, cause precipitation of fine intermetallic particles in this deformed layer, resulting in a higher dispersoid density and lower solute levels compared with the bulk of the material where the precipitation is sluggish in the absence of stress [7, 8]. This deformed surface layer has different electrochemical properties and microstructural characteristics compared with the underlying bulk microstructure that affects corrosion susceptibility [9-12].

Deformation is likely to have two effects on the electrochemical behaviour of aluminium alloys. One effect is to cause the precipitation of particles that act as local cathodes and pit initiation sites. The other effect is that the formation of precipitates will deplete the adjacent matrix in solute, making it more susceptible to dissolution [13-17]. Filiform corrosion behaviour of aluminium alloys is generally controlled by the presence of this micro-deformed layer at the surface, which results in the precipitation of very fine intermetallic particles during subsequent heat treatment [13, 14, 18]. Preventing the formation of a deformed layer by a modified fabrication process or removal of the layer

by etching or alternative surface treatment eliminates or significantly reduces the corrosion susceptibility [19, 20].

Many surface preparation procedures such as grinding, machining and sand blasting also generate a deformed layer at the surface [21-24]. The difference in surface morphology and enhanced deformation at the surface together determine the susceptibility of the surface to corrosion [21-23].

The aim of this project is to study the effect of surface preparation and deformation on the electrochemical behaviour of Al-Mn alloys. This is done by investigating the effect of various surface preparation methods for aluminium alloys on corrosion behaviour, profiling the electrochemical reactivity of the active layer on rolled aluminium alloy sheet, and investigating the surface deformation effect in rolled sheets by uniaxial deformation and ECAE processing.

Chapter 2 Literature Review

2.1 Metallurgy of 3XXX Aluminium Alloys

In the binary Al-Mn alloy system, the maximum solubility of manganese in the α-solid solution is 1.82 wt% at the eutectic temperature of 658.5°C, the solubility decreasing with decreasing temperature [1-4]. Alloys in this group, Al-Mn, and Al-Mn-Mg, are generally not age-hardenable. These alloys tend to be used when moderate strength combined with high ductility, good weldability, good formability, and excellent corrosion resistance are required. In sheet form, the strength is achieved by application of various degrees of strain hardening, and in some cases by intermediate annealing [25-27]. Commercial Al-Mn alloys generally contain 0.25–1.25 wt% manganese [3-5, 17]. In these alloys, Fe and Si are normally present as impurities, and sometimes Cu, Mg and Zn are also added as minor alloying elements [2-4, 17]. The 3003 alloy is one of the most popular alloys in this group, which has good formability, very good resistance to corrosion, and good weldability [1]. The composition, melting range, density and tensile properties of selected Al-Mn alloys are included in Tables 2.1, 2.2 and 2.3, respectively.

Table 2.1 Compositions of selected non-heat-treatable wrought Al-Mn alloys. [2, 3, 6, 28-30]

British Registered Designation	ISO Designation	Si	Fe	Cu	Mn	Mg	Zn	Cr	Ti	Al
3003	AlMn1Cu	0.6	0.7	0.05–0.20	1.0–1.5	–	–	–	–	Remainder
3103	AlMn1	0.5	0.7	0.10	0.9–1.5	–	–	–	–	Remainder
3004	AlMn1Mg1	0.3	0.7	0.25	1.0-1.5	0.8–1.3	0.25	–	–	Remainder
3005	AlMn1Mg0.5	0.6	0.7	0.30	1.0–1.5	0.2-0.6	0.25	0.10	–	Remainder
3105	AlMnMg	0.6	0.7	0.30	0.3–0.8	0.2–0.8	0.40	0.20	0.10	Remainder

Table 2.2 The melting range and density of selected non-heat-treatable wrought Al-Mn alloys. [28]

British Registered Designation	Melting range (°C)	Density (kg/m^3) × 10^3
3003	643–655	2.73
3103	640–655	2.73
3203	643–655	2.73
3004	–	2.72
3104	–	2.72
3204	–	2.71
3005	629–654	2.73
3105	629–655	2.72

Table 2.3 Typical mechanical properties and applications of selected non-heat-treatable wrought Al-Mn alloys. [2, 3, 5, 6, 25, 26, 29]

British Registered Designation	Temper	0.2% proof stress (MPa)	Tensile strength (MPa)	Elongation (% in 50 mm)	Typical applications
3003	F	35	120	28	rigid containers, cooking utensils, pressure vessels, heat exchanger materials, chemical equipment
	O	41	110	40	
	H14	144	151	16	
	H18	185	200	4	
	H121	82	117	110	
	H183	–	185	–	
	H191	–	206	–	
	H231	103	130	48	
	H271	–	172	48	
	H281	165	185	41	
3103	F	35	120	28	heat exchanger materials
	O	70	112	24	
	H12	–	120-145	9	
	H14	140	155	6	
	H16	–	160-195	4	
	H18	185	195	4	
3004	O	70	180	20	rigid containers, bodies of beverage cans, storage tanks, packaging materials
	H38	250	280	5	
3005	F	50	120	14	roofing and siding sheets, furniture, false ceilings, aerials and antennae, ladders, rolling shutters, mobile homes, rain carrying goods, heat insulation sheets, heat exchanger materials
	O	55	130	25	
	H18	225	240	4	
	H191	226	240	14	
	H192	261	268	21	
	H281	199	213	21	
	H292	192	220	21	
	H39	199	226	27	
3105	O	–	110	20	General sheet materials, plate, extrusions
	H12	115	130	5	
	H14	145	160	4	
	H16	170	185	3	
	H18	190	215	2	

Note F: As fabricated
O: Annealed, soft
H12: Strain-hardened, quarter hard
H14: Strain-hardened, half hard
H16: Strain-hardened, three quarter hard
H18: Strain-hardened, fully hard
H38: Strain-hardened and stabilized, fully hard
H39: Strain-hardened and stabilized, extra hard

2.1.1 Al-Mn-Fe-Si Phase Diagrams

2.1.1.1 Al-Mn System

The equilibrium Al-Mn phase diagram is shown in Figure 2.1 [4]. The aluminium solid solution alloy is face-centred cubic. The phase in equilibrium with it is Al_6Mn, which is orthorhombic. This phase forms an eutectic with aluminium at approximately 1.8 wt% Mn at 658.5°C. The Al_6Mn phase has a limited range of primary crystallisation; above 4.1 wt% Mn, it forms by a peritectic reaction from Al_4Mn. Al_4Mn is usually reported as hexagonal [4, 31, 32].

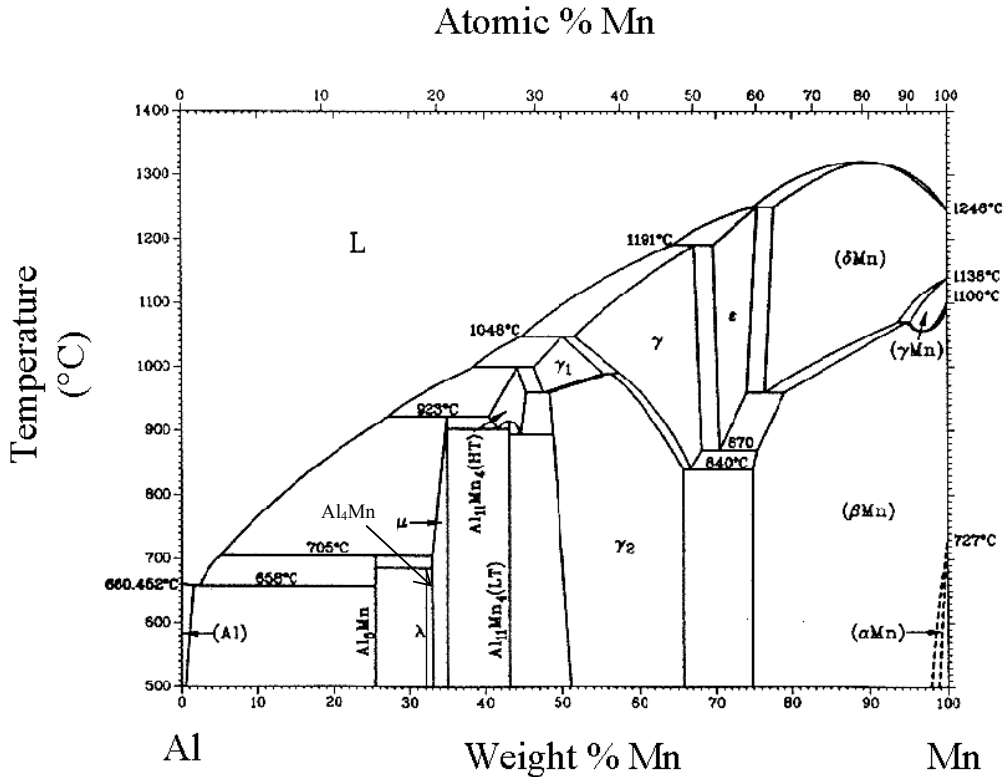

Figure 2.1 Equilibrium diagram of the Al-Mn system [4].

2.1.1.2 Al-Fe-Mn System

There are three primary phases in the Al-Fe-Mn system; Al, Al_3Fe, and $Al_6(MnFe)$ [4, 33]. $Al_6(MnFe)$ is similar to the Al_6Mn phase in which up to 1.5 wt% of the manganese can be replaced by iron, with only a slight change of lattice parameters [3, 4, 17]. If the manganese content exceeds 4 wt%, Al_4Mn may also appear.

The maximum solubility of iron in aluminium is 0.03–0.04 wt%, and this is unchanged in the ternary alloys. On the other hand, the manganese solubility is decreased. The maximum solubility of manganese in iron-bearing alloys may be approximately one half of that in the binary aluminium-manganese alloys [4]. Al_3Fe is monoclinic. Up to 2 wt% Fe can be replaced by manganese with practically no change in structure.

2.1.1.3 Al-Mg-Mn System

In this system, $Al_{18}Mg_3Mn_2$ forms in alloys with magnesium content above the limit of solubility (3–17 wt% Mg depending on temperature) [4]. $Al_{18}Mg_3Mn_2$ has a range of composition 10–12 wt% Mg and14–18 wt% Mn. It is cubic.

In the solid state, $Al_{18}Mg_3Mn_2$ can be in equilibrium with Al_8Mg_5 and Al_6Mn. Both magnesium and manganese reduce each other solid solubilities. At eutectic

temperature, magnesium solubility is down to 12 wt% Mg from 17.4 wt% Mg in the manganese-free alloy and the manganese solubility is down to 0.5 wt% from the 1.8 wt% in magnesium-free alloys.

2.1.1.4 Al-Fe-Mn-Si System

The binary and ternary diagrams have limited application because commercial aluminium alloys always contain appreciable amounts of both iron and silicon, which significantly affect the microstructure. The main secondary phase in the quaternary system is α-$Al_{15}(MnFe)_3Si_2$ [4]. The structure of α-$Al_{15}(MnFe)_3Si_2$ is cubic, and is formed by the replacement of manganese atoms in $Al_{15}Mn_3Si_2$ by iron atoms. Depending on the composition of the alloy and heat-treatment, other secondary phases might appear, such as binary Al_3Fe and tertiary $Al_6(MnFe)$, and silicon-containing phases such as Al_8Fe_2Si and Al_5FeSi [4].

Al_8Fe_2Si, also designated α–(FeSi) or $Al_{12}Fe_3Si_2$, has a range of composition 30–33 wt% Fe and 6–12 wt% Si. It is hexagonal, and can dissolve little or no manganese. Al_5FeSi, also designated as β–(FeSi), has a range of composition 25–30 wt% Fe and 12–15 wt% Si. It is monoclinic. It crystallises as thin platelets, which in section appear as thin needles [4, 34, 35].

In most of the commercial alloys, $Al_6(MnFe)$ undergoes a peritectic reaction by which it transforms into α-$Al_{15}(MnFe)_3Si_2$ [4].

2.1.2 Intermetallic Particles in 3XXX Aluminium Alloys

2.1.2.1 Constituent Particles

Intermetallic phases formed during the solidification of the alloys are generally referred to as constituent or insoluble particles, and usually have dimensions of several micrometres [3], although this depends on solidification conditions. As equilibrium conditions are rarely obtained during typical solidification processes, the composition of the constituent particles may differ from equilibrium values, and in addition, significant amounts of alloying elements may be retained in supersaturated solid solution [4, 8].

In as cast 3XXX ingots, the aluminium matrix phase is dendritic. Between dendrite arms is the eutectic mixture, which contains the coarse Fe-rich intermetallic constituent particles [7]. The particles are of two major types: the orthorhombic $Al_6(MnFe)$, which tends to form larger particles, and the cubic α–Al(MnFe)Si [4, 7, 8, 17, 36, 37]. α–Al(MnFe)Si results from a peritectic reaction of the $Al_6(MnFe)$ with the remaining liquid [4].

The relative amounts of $Al_6(MnFe)$ and α−Al(MnFe)Si phases are determined by the specific alloy composition and solidification rate [7, 36]. For a given alloy, the higher the solidification rate, the finer the intermetallic particles [25, 38].

Fe, being highly insoluble in Al, has the largest effect on the volume fraction of constituent particles. Most commercial as-cast 3XXX ingots contain the $Al_6(MnFe)$ phase rather than the α−Al(MnFe)Si phase as constituent particles. In roll-casting of 3003, however, where the solidification rates are much higher, the α−Al(MnFe)Si phase dominates [7].

The exact composition of the two phases may vary quite significantly, and in particular, the iron to manganese ratio can vary across a wide range [13]. Relevant literature gives the stoichiometry of α-Al(MnFe)Si as either α-$Al_{12}(MnFe)_3Si$ [7, 17, 35, 37, 39] or α-$Al_{15}(MnFe)_3Si_2$ [4]. These differences are probably due to Al atoms substituting for Si atoms [40]. The α-Al(MnFe)Si phase has higher hardness than the $Al_6(MnFe)$ phase [36, 41]. Both $Al_6(MnFe)$ and α-Al(MnFe)Si have solution potentials almost the same as that of the solid solution matrix [17].

The characterisation of intermetallic particles in AA3004 was carried out by Merchant et al. [38]. They found that AA3004, when cast as a thick ingot (650 mm) with direct chill (DC) casting, solidified with the intermetallic particles enveloping the dendrites as faceted platelike phases. When cast as a thin (12 mm) strip, it solidified

with the intermetallic particles enveloping the dendrites as fine network consisting of rodlike growth forms. The as-cast intermetallic structure of strip, in particular, is unstable because of irregular branched-rod morphology and a high density of growth defects. Because of a greater tendency of the Fe atoms to segregate, the intermetallics formed during solidification contain relatively more Fe than Mn. Ingot-sourced sheet is populated predominantly with larger constituent particles, whereas strip-sourced sheet is populated with smaller constituent particles.

2.1.2.2 Precipitation Processes

During subsequent thermo-mechanical processing (homogenisation, hot and cold rolling, and annealing) the composition of the smaller constituent particles may change significantly, and supersaturated elements may be precipitated as finer intermetallic particles [38, 42-44]. Particles precipitated from solid solution are usually referred to as secondary precipitates or dispersoid particles [4].

Any Mn, Fe, and Si that are supersaturated in the matrix can precipitate as a result of appropriate thermomechanical treatment. The precipitation occurs initially on appropriately oriented primary particles, and eventually as fine secondary precipitates. In general, Si enhances precipitation of Fe; Fe, Cu, Mg, and Si enhance precipitation of Mn; while Fe, Si, and Cr (if present) enter the primary phase during thermal exposure [38, 45]. Mn, Si, and Cr (but not Fe) are usually present in the secondary precipitates [38].

During homogenisation in as-cast 3XXX ingots, the supersaturated Mn, Fe and Si in the matrix precipitate as fine dispersoid particles of α-Al(MnFe)Si and/or Al_6(MnFe) [7]. Moreover, Mn diffuses more rapidly and enters secondary precipitates of Al_6(MnFe) until the phase has achieved the maximum Mn content at $Al_6(Mn_{0.5}Fe_{0.5})$ [38].

During high temperature soaking, both the primary intermetallic particles and the secondary intermetallic particles (dispersoid particles) are generally dissolved in the matrix [25, 37, 43]. On the other hand, soaking at a low or medium temperature results in the precipitation of numerous secondary intermetallic particles [25]. The dissolution kinetics of the non-equilibrium secondary intermetallic particles during heat-treatment are controlled by the diffusion of Mn in the α-matrix [37].

2.1.2.3 Effect of Mechanical Deformation on Precipitation

Enhanced deformation of aluminium alloys has an effect on precipitation kinetics. Luiggi [46-48] studied the effect of plastic deformation on the precipitation kinetics of AA3003, which contains Al_6(MnFe) and α-$Al_{12}(MnFe)_3Si$ intermetallic particles, using the thermoelectric power (TEP) technique. It was found that Mn diffusion is the dominant process in the precipitation kinetics. Deformation reduces the temperatures at which precipitation starts. Furthermore, at the same annealing temperature, a higher level of deformation does significantly increase the rate of precipitation.

Senkov et al. [49] found that severe plastic deformation of an Al-Fe alloy leads to microstructural refinement and formation of a nanocrystalline structure in an aluminium-based matrix with a homogeneous distribution of small secondary phase particles.

Scamans et al. [50] investigated the correlation between the amount of surface deformation induced by various grinding practices and subsequent annealing on corrosion behaviour of AA3005. It was found that grinding of aluminium alloys surfaces produces ultra-fine grain sized deformed surface layers with fine intermetallic particles.

2.1.3 Microstructure of Rolled Aluminium Sheet

The microstructure and texture of rolled aluminium alloys are dependent on various processing parameters such as alloy composition, casting method (e.g. solidification rate), pre- and post-hot rolling treatments (e.g. homogenisation temperature and time, and cold rolling reduction). One parameter that is found to impact significantly on the evolution of microstructure and texture is the type of intermetallic particles through their chemistry, size and interparticle spacing [7].

Hot rolling progressively makes the microstructure more homogeneous by breaking up the cell structure, fracturing the constituent particles, and distributing the constituent and dispersoid particles more uniformly throughout the microstructure [38]. Recrystallisation, even after extensive hot rolling, results in a flat, elongated grain structure, indicating that the microstructure is still layered with the remnants of the ingot

structure. Final cold rolling to thin gauge sheet results in a more homogeneous microstructure with a very fine grained microstructure and uniformly distributed constituent and dispersoid particles [7].

The microstructure of hot rolled and cold rolled aluminium alloys has been investigated during the past decade by several researchers [9-11, 13, 14, 20, 36, 51]. Fishkis and Lin [10] investigated a hot rolled Al-Mg alloy. They found that the heavily deformed micrograined layer at the surface of hot rolled aluminium alloy sheet can be attributed to a higher shear deformation at the surface. This produces fine intermetallic particles as a result of fragmentation of larger intermetallic particles exposed at the surface and an additional number of fine dispersoid particles nucleated during further annealing.

In hot rolled AA3004 with 2.3 mm thickness, Kamat and Saimoto [8] found that the large intermetallic particles, in the range of 5–60 μm^2, such as $Al_6(MnFe)$ and α-Al(MnFe)Si, have significant variation in size from the surface to centre with an increase in size towards the centre. The area fraction of small $MgSi_2$ intermetallic particles (< 0.5 μm) started to increase considerably towards the end of recrystallisation.

Afseth et al. [13, 14] investigated the effect of thermo-mechanical processing of AA3005. It was found that both hot and cold rolling resulted in enhanced surface shear deformation and the formation of a thin deformed layer of metal at the surface with fine secondary intermetallic particles during subsequent heat-treatment which differs from the

underlying bulk. It was observed that the near surface region of the material contained a smaller number of larger, intermetallic particles than the underlying bulk.

2.1.4 Equal Channel Angular Extrusion (ECAE)

Equal channel angular extrusion (ECAE) is a special deformation technique originally developed by Segal [52] in 1971, in which a billet is subjected to very high plastic strain without experiencing any overall change in the billet's shape.

In ECAE, the material is deformed successively by simple shear at the crossing plane of the two channels (the shear plane). The orientation of the shear plane with respect to the long-axis of the extruded specimen depends on the intersecting angle between the two channels [53, 54].

The principle of ECAE is illustrated schematically in Figure 2.2. A billet, in the form of a rod, is machined to fit within the entrance channel of an ECAE die. Then it is extruded through the die until it emerges from the exit channel. Within the die, the channel bends abruptly through an angle Φ, so that the billet undergoes strain by simple shear as it passes through the shear plane at the point of intersection of the two channels. It is possible to define another internal angle ψ, which delineates the outer arc of curvature where the two channels intersect [55].

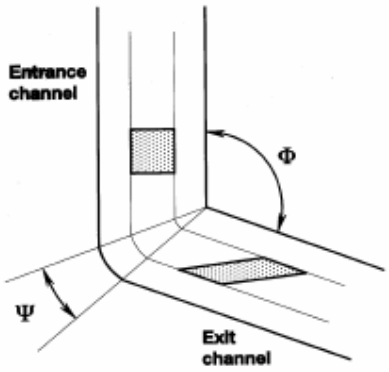

Figure 2.2 The principle of ECAE showing the shearing of a cubic element and the two angles Φ and ψ [56].

By considering an ECAE die having angles of $\Phi = 2\phi$ and $\psi = 0°$, it was shown by Segal [55], that the total strain imposed on the sample in a single passage through the die, ε_1, is given by Equation 2.1.

$$\varepsilon_1 = \frac{2}{\sqrt{3}}\cot\phi \qquad 2.1$$

Subsequently, Iwahashi et al. [56] also included the angle ψ and showed from first principles that ε_1 is given more explicitly by Equation 2.2.

$$\varepsilon_1 = \frac{2}{\sqrt{3}}\left[\cot\left(\frac{\phi}{2}+\frac{\psi}{2}\right)\right] + \psi\left[\sin\left(\frac{\phi}{2}+\frac{\psi}{2}\right)\right]^{-1} \qquad 2.2$$

A consequence of Equation 2.2 is that multiple passes through the same die results in an accumulated strain, ε_N, again without experiencing any overall change in the cross-

sectional dimensions. It is obtained simply by multiplying the strain per pass by the number of passes, *N*, as shown in Equation 2.3.

$$\varepsilon_N = N\varepsilon_N \qquad 2.3$$

However, the above analysis is an idealised case. It assumes no friction, and that the entire cross section of the sample is sheared equally as it flows through the deformation zone. The analysis also does not take into account normal strains experienced by the sample due to bending and unbending as it flows through the deformation zone, especially when the die corners are not sharp. [57, 58]

In ECAE, the strain path can be varied by rotating the billet between extrusion cycles to develop different microstructures [52, 59]. The possibility of rotating the sample between repeated passes has been defined in four different processing routes, route A, B_A, B_C, and C [60]. In route A, the sample is extruded repetitively without any rotation. In route B_A, the sample is rotated by 90° in alternate directions through 0°, -90°, 0°, -90° between each pass and in route B_C, the sample is rotated by 90° in the same direction through 0°, -90°, -180°, -270° between each pass. In route C, the sample is rotated by 180° between each pass.

Langdon and coworkers [59, 61-64], Chakkingal et al. [65] and Chang et al. [66] have investigated the development of microstructure and the influence of above processing route during ECAE for pure aluminium.

Gholinia et al. [67] have investigated the effect of strain path on the development of deformation structures in Al-Mg alloys processed by ECAE. They found that with a constant strain path (route A) and ±90° rotation (route B_A), fibrous grain structures are produced (Figure 2.3(a) and (b)), but the grains become elongated at a lower rate with ±90° rotation. For the +180°, and +90° rotation processing routes (route C and route B_C), that result in fully redundant strains every two and four cycles, respectively, the appearance of the grains is very similar to that in the original cast material, despite a total effective strain of 2.7 (Figure 2.3(c) and (d)). However, there is evidence of a deformation substructure developing within the grains. The work of Gholinia et al. demonstrated that the most efficient processing route for forming a submicron grain structure by severe deformation via ECAE is to maintain a constant strain path, and the least effective is to reverse the shear in each alternate cycle, by rotating the billet through 180° (Figure 2.4(a) and (b)). From Figure 2.4(a), it can be seen that there are low angle boundaries within many of the submicron grains. In Figure 2.4(b) low angle boundaries can be identified within the grains and the material thus contains larger regions comprised entirely of subgrains as opposed to submicron grains. Both forms of 90° rotation (Figure 2.4(c) and (d)) gave a greater extent of grain refinement than 180° rotation, but were less efficient, in terms of forming new high angle grain boundary area, than deformation with a constant strain path.

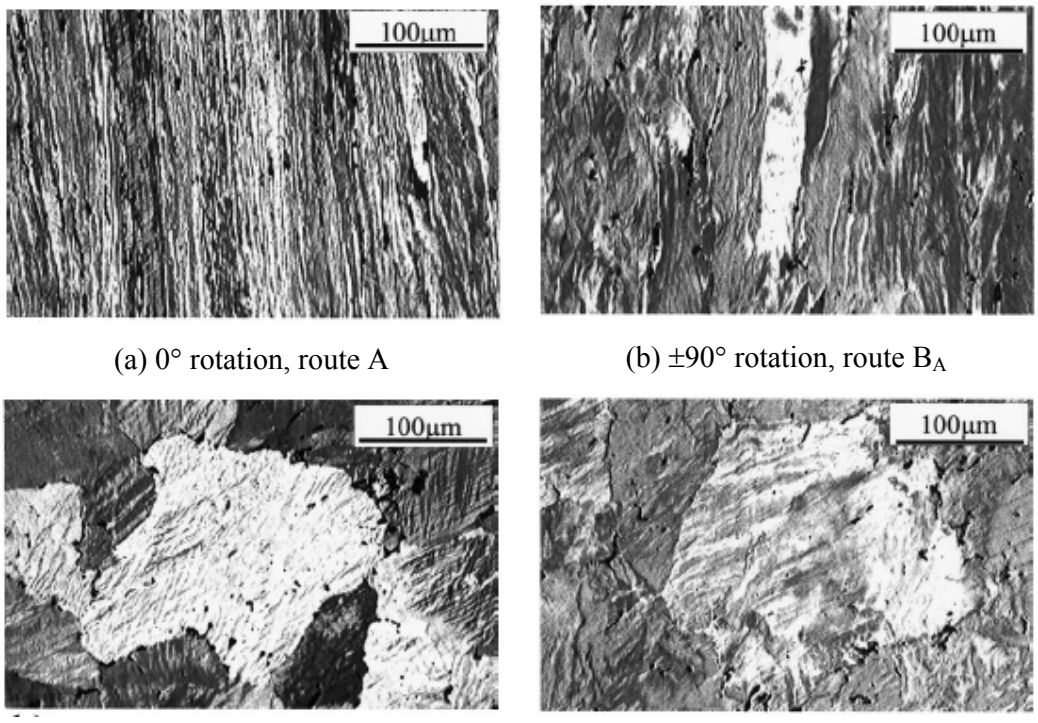

(a) 0° rotation, route A

(b) ±90° rotation, route B_A

(c) 180° rotation, route C

(d) +90° rotation, route B_C

Figure 2.3 Optical micrographs of extruded Al-Mg billets after four extrusion cycles for the four different processing routes investigated: (a) constant strain path, route A, (b) ±90° rotation, route B_A, (c) +180° rotation, route C and (d) +90° rotation, route B_C. [67]

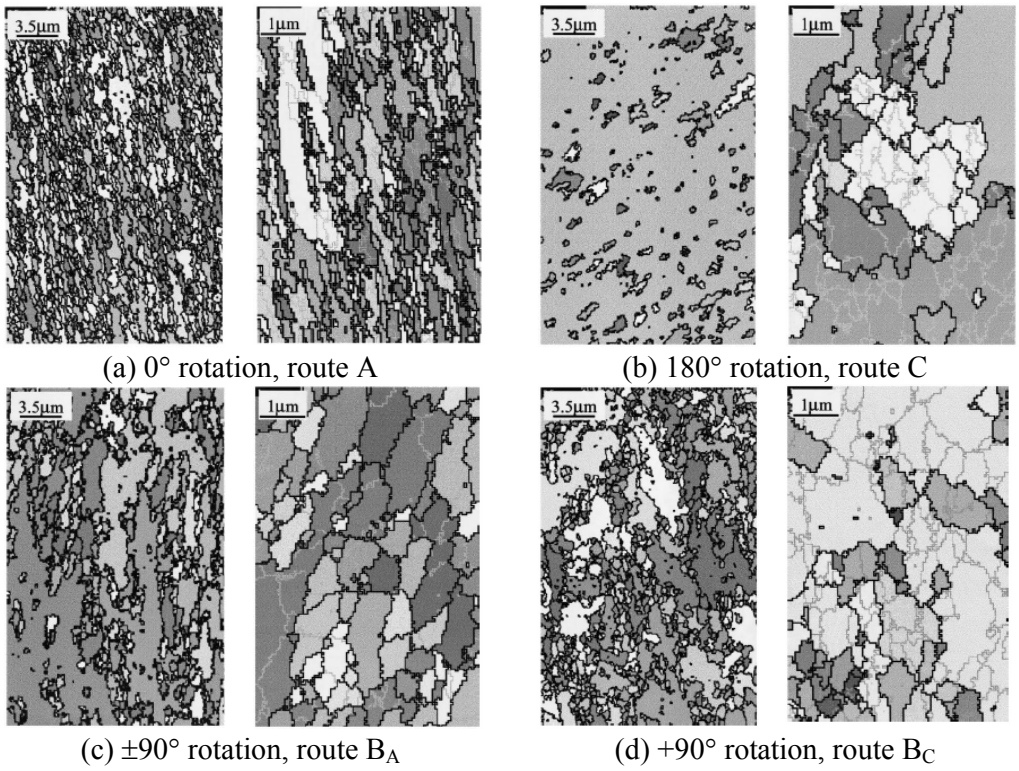

Figure 2.4 EBSD (electron backscattered diffraction) orientation data from Al-Mg billets after 16 extrusion cycles showing large maps of reconstructed grain structures, with only the high angle grain boundaries highlighted, and higher magnification smaller area maps, including both the high and low angle boundaries, for each of the four processing routes: (a) no rotation, (b) 180° rotation, (c) ±90° rotation and (d) +90° rotation. The high and low angle boundaries are indicated by dark and light lines, respectively. [67]

ECAE processing also affects primary and secondary intermetallic particles in aluminium alloys, as reported by Stolyarov and Lapovok [68]. They investigated the structure of Al-5 wt% Fe alloy processed by ECAE and found that the structure of the cast alloy consisted of the Al matrix, large primary (10 × 80 μm) and fine (about 2 μm) $Al_{13}Fe_4$ intermetallic particles. ECAE of the cast alloy leads to fracture of both intermetallic particles and to formation of secondary intermetallic particles of more uniform shape and size than in the initial state.

2.2 Corrosion of Aluminium and Its Alloys

2.2.1 Electrochemistry of Aluminium in Aqueous Environments

High purity aluminium (99.999%) has an excellent resistance to corrosion in neutral environments because an alumina (Al_2O_3) film, a passive film, forms on the surface by following equation:

$$2Al + 3H_2O \rightarrow Al_2O_3 + 6H^+ + 6e^- \qquad 2.4$$

This film is bonded strongly to its surface and, if damaged, re-forms immediately in most environments. The film that develops in normal dry atmospheres grows to thicknesses much greater than 1 nm [69]. The film is highly resistant to dissolution in neutral environments, but is soluble in both acidic and aqueous environments, as shown in potential-pH diagram (Figure 2.5) [70]. The passive oxide film is also a good insulator. It does not allow electrons that are produced by oxidation reaction of aluminium to transfer at the film/solution interface where oxygen reduction, Equation 2.5, occurs.

$$O_2 + 2H_2O + 4e^- \rightarrow 4OH^- \qquad 2.5$$

The passive film is often assumed to be a simple inert layer covering the underlying metal and blocking access of the environment to the metal. The reality is

much more complicated. This film can have a range of thickness, structure, composition, and protectiveness depending on alloy composition, environment, potential and exposure history [69, 71-73].

The corrosion resistance of aluminium can be anticipated on thermodynamic "potential-pH" diagram or Pourbaix diagram (Figure 2.5), on which the thermodynamic metal-water reactions are represented [69, 70]. This diagram shows: (1) The areas where the metal will corrode through by the formation of soluble compounds; (2) the passive areas where solid phases form; (3) the immune areas where the metal is thermodynamically stable [69, 70, 74-76].

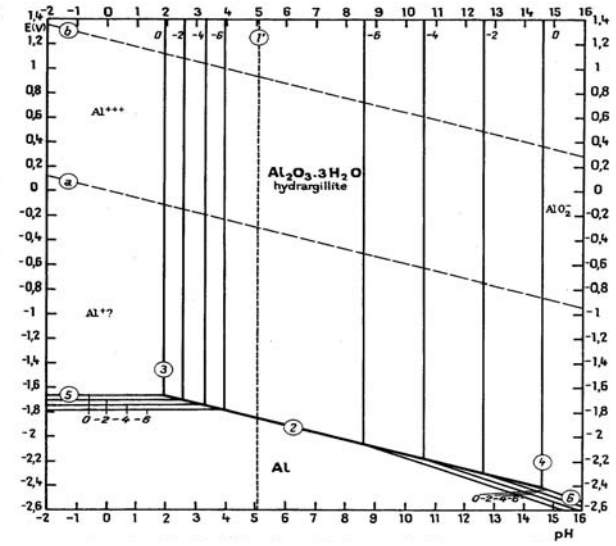

Figure 2.5 The potential-pH diagram of aluminium-water system at 25°C [70].

As shown in Figure 2.5, aluminium is passive (is protected by its oxide film) in the pH range of about 4 to 9 in most aqueous solutions [69, 75]. The limits of this range,

however, vary somewhat with temperature and the presence of substances that can form soluble complexes or insoluble salts with aluminium [69].

From Figure 2.5, in low pH acidic environments, aluminium will dissolve as aluminium ions (Al^{3+}) by the following anodic dissolution reaction:

$$Al \rightarrow Al^{3+} + 3e^{-} \qquad 2.6 \text{ (solid line 5)}$$

In alkaline environments, aluminium will dissolve as aluminate ions, $Al(OH)_4^-$, by the following equation:

$$Al + 4OH^{-} \rightarrow Al(OH)_4^{-} + 3e^{-} \qquad 2.7 \text{ (solid line 6)}$$

(note: $Al(OH)_4^-$ is equivalent to AlO_2^- [77])

As stated above, a passive film is stable in most aqueous solutions within the pH range 4–9. However, the passive film becomes unstable in the regions of acidity and alkalinity. Thus, it will react as shown by these following equations:

In acidic conditions: $Al_2O_3 + 6H^{+} \rightarrow 2Al^{3+} + 3H_2O$ 2.8 (solid line 3)

In alkaline conditions: $Al_2O_3 + 3H_2O + 2OH^{-} \rightarrow 2Al(OH)_4^{-}$ 2.9 (solid line 4)

Pure aluminium has very low yield strength (7-11 MPa) [2]. Its strength can be increased by alloying with metals such as Cu, Mg, Mn and Zn [1, 2, 30, 69, 71, 74]. Hence, many commercial aluminium alloys contain one or more of these elements. However, the presence of the alloying elements has some adverse effects on corrosion behaviour. These elements form intermetallic particles whose oxides are semiconductors, and better sites for electrochemical reaction than the matrix which is covered with alumina, which is an insulator films [16, 17, 71, 72, 74, 78-82]. Therefore, they allow the cathodic reaction (Equation 2.5) to occur, as will be described in the following sections.

2.2.2 Pitting Corrosion of Aluminium Alloys

Pitting corrosion is a form of highly localised corrosion occurring on a metal surface. Pitting is commonly observed under conditions where there is little or no uniform corrosion. It typically occurs as a process of local anodic dissolution where metal loss is exacerbated by the presence of a small anode and a large cathode [69, 71] as shown in Figure 2.8. The extent of pitting corrosion can vary greatly depending on the exposure conditions and surface conditions of the materials. Pits in aluminium alloys are typically associated with intermetallic particles [16, 78-84].

2.2.2.1 Pit Propagation

The mechanism of pit growth is shown schematically in Figure 2.6. It can be controlled by charge-transfer processes (activation), ohmic effects, mass transport [85], or some combination of these factors [86].

The anodic dissolution results in cations, Al^{3+}, and then hydrolysis leads to drop in pH, Equation 2.10.

$$Al^{3+} + H_2O \rightarrow AlOH^{2+} + H^+ \qquad 2.10$$

These ions are positive, so Cl^- ions are drawn into the pit to balance charge (Figure 2.6). Both a low pH and high chloride concentration favour dissolution over repassivation.

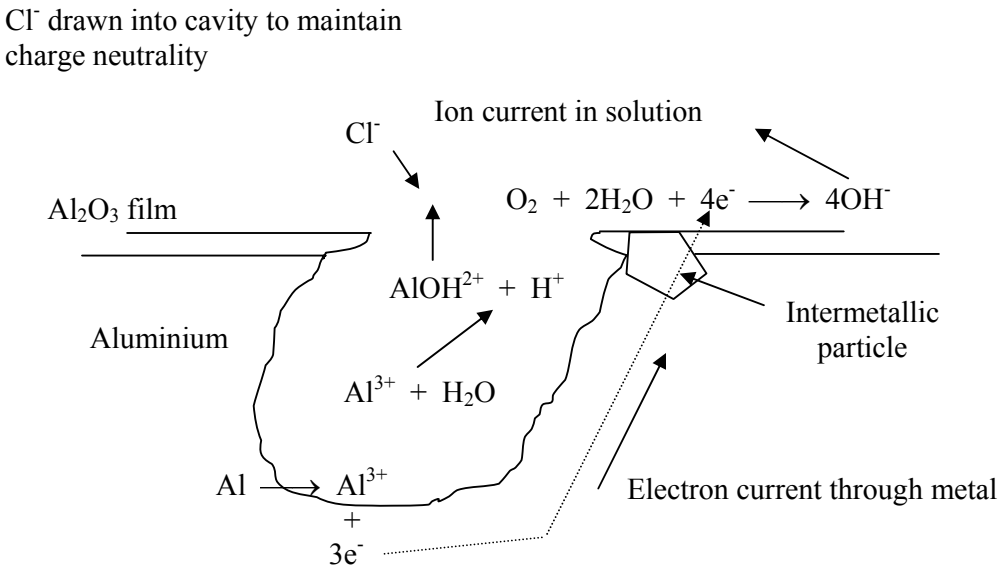

Figure 2.6 The mechanism pit growth in an aluminium alloy exposed to a chloride solution [87].

Pit stability depends on the maintenance of a pit electrolyte composition and pit bottom potential that are severe enough to prevent repassivation of the dissolving metal surface at the bottom of the pit [88]. In other words, the current density at the pit surface is high enough so that the rate of production of cations is greater than the rate that they

can diffuse out from pit. Several researchers have suggested that pit covers [89-92] help to maintain an aggressive local chemistry inside of the pit, playing an important role in controlling pit stability.

The stability of pits can be explained by Fick's first law [93]:

$$i^* = \frac{nFDC^*}{x} \qquad 2.11$$

where i^* is the minimum anodic current density for stabilising the pit, n is the number of electrons transferred in the anodic dissolution, F is the Faraday constant, D is the cation diffusion coefficient within the pit, C^* is the concentration of dissolved cations at the bottom of the pit required to prevent repassivation, and x is the depth of the pit.

From Equation 2.11, it can be seen that very small pits (small x) require a high critical current density. This requires the sample to be at a high potential which explains why a critical pitting potential (E_{pit}) is often observed. A pitting potential is a critical potential which must be exceeded for pits to develop.

Galvele [94] provided a detailed analysis of the influence of pit chemistry changes on pit growth and stability. The concentration of various ionic species at the bottom of a model one-dimensional pit geometry was determined as a function of current density

based on material balance that considered generation of metal ions by dissolution, outward diffusion, and thermodynamic equilibrium of various reactions such as metal ion hydrolysis. Galvele found that a critical value of the factor $x \cdot i$ (where x is pit depth and i is current density), corresponded to a critical pit acidification for sustained pit growth. This value can be used to determine the current density required to initiate or sustain pitting at a defect of a given size. A critical value of $x \cdot i$ for pit stability of Al has been suggested to be 0.2 Am^{-1} [95].

If the rate of cation production at the bottom of the pit is greater than the rate of escape from the mouth of pit, then the accumulation of cations within the pit will lead to supersaturation of the salt solution, and thus precipitation of a salt film. Many groups have observed the precipitation of salt films within pits, and these salt films are believed to play an important role in the stability of pits [88, 90, 96-99]. A necessary condition for pit repassivation is dissolution of the salt film [88].

A number of environmental and material parameters are critical to the pitting process, such as potential, alloy composition, electrolyte concentration, and temperature. Pit growth in aluminium and aluminium alloys has been studied by many researchers, e.g. [82, 86, 88, 94, 100-110]. The pit growth kinetics on aluminium was studied by using a metal foil technique by Hunkeler and Bohni [111]. They found the pit growth rate is not only time dependent, but also markedly influenced by the applied potential and the chloride concentration of the electrolyte.

Addition of foreign ions either accelerates or inhibits pit growth depending on the type and concentration of the ions added. For example, the addition of SO_4^{2-} and NO_3^- ions into NaCl solution impedes pit initiation on pure aluminium, but enhances pit growth [112, 113]. In the presence of SO_4^{2-} ions, it appears that pits grow preferentially in the lateral direction. In the presence of NO_3^- ions, the pits observed grow preferentially in the downward direction.

As mentioned above, as pit stability depends on the product $x \cdot i$, large pits are more stable (require a lower pit current density than small ones). It is therefore not clear how small pits can nucleate and grow into larger ones without protection. Such protection is generally provided for small pits by remnants of the passive film, which provides an additional diffusion barrier to the escape of cations. Small pits that grow with the protection of the passive film are known as metastable pits.

2.2.2.2 Metastable Pitting

Metastable pits are pits that initiate and grow for a limited period, of the order of seconds or less, before repassivating, whereas stable pits survive the metastable stage and continue to grow [114]. Metastable pits can form at potentials far below the pitting potential (which is associated with the initiation of stable pits), and during the induction time before the onset of stable pitting at potentials above the pitting potential [115]. During open circuit potential measurements, these events are characterised by potential transients in the active direction of open circuit. Metastable pitting has been observed on

aluminium [95, 116]. The number of metastable pitting events has been shown to be a function of the potential, the potential scan rate, the chloride concentration, the oxide thickness, and the alloy composition [115].

The average metastable pit current density was found to increase with increasing applied potential. Metastable pit growth is stabilised by the resistance associated with the passive film [91]. Metastable pits tend to repassivate before a salt film precipitated because of a violent rupture of their passive film covers, which dilutes the local pit environment, whereas the current associated with stable pits fluctuates after the time required for salt film precipitation, but then continues to increase.

If the conditions are such that a salt film can form, the pit has a greater chance of surviving the rupture of the cover and becoming a stable pit because of the buffering action of the salt, which can replenish the pit environment by dissolving.

2.2.2.3 Pit Initiation

In high purity metals, it is thought that pits can initiate at defects in the passive film [71, 74, 117-122]. However, in commercial alloys, pits are generally associated with second-phase particles [16, 17, 78-84].

2.2.2.3.1 Pit initiation at passive film defects

There are many mechanisms of pit initiation that have been proposed for passive surfaces; these can be arranged in three main groups: penetration mechanisms, adsorption mechanisms and film breaking mechanisms [117, 123]. These mechanisms are described in terms of pure metal systems.

(a) Penetration mechanism

The penetration mechanism (Figure 2.7(a)) requires transfer of aggressive anions, such as Cl^-, through the passive film to the metal/oxide interface, where aggressive dissolution is promoted [117, 123]. The high electric field strength and a high defect concentration within the presumably severely disordered structure of the passive film may explain this transfer. This mechanism is supported by the existence of an induction time for pitting following the introduction of chloride into an electrolyte.

On the basis of these ideas, Macdonald and co-workers [118, 119] described passive film growth by the movement of point defects under the influence of an electric field. The major point defects in an oxide film are assumed to be holes and metal and oxide vacancies. Transport of vacancies across the film controls the film growth. The point-defect model has been used to explain pit initiation by assuming that aggressive ions (chloride ions), are adsorbed and incorporated at the outer surface where they are annihilated by the oxidative injection of cations from the metal. However, if the flux of vacancies is larger than can be accommodated by oxidation, the vacancies will condense at the metal/film interface to form a void that is the first step in the pitting process according to this model.

(b) Adsorption mechanism

The mechanism is based on the competitive adsorption of chloride ions and oxygen as shown in Figure 2.7(b) [117, 123]. The theory is based upon the suggestion that areas of local thinning of the passive film occur locally because of some local adsorbed species, and this leads to a local increase in electric field strength [120, 121]. This increase in the electric field strength may eventually lead to complete breakdown and the formation of a pit.

(c) Film breaking mechanism

It is considered that the thin passive film is in a continual state of breakdown and repair [30, 117, 123]. Mechanical stresses at weak sites and flaws resulting from electrostriction and surface tension effects may cause the local breakdown events [122]. In non-aggressive environments, these local breakdown sites will rapidly repair. This mechanism is illustrated schematically in Figure 2.7(c). In fact, the background passive current density may come from a summation of many such breakdown and repair events. The film-breaking model really involves initiation based on pit growth stability. According to this model, breakdown will only lead to pitting under conditions where pit growth is possible.

(a) Penetration mechanism

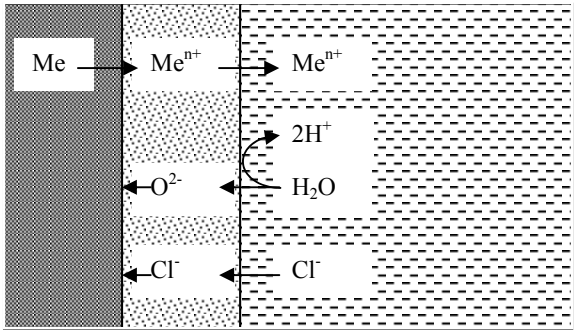

(b) Adsorption mechanism

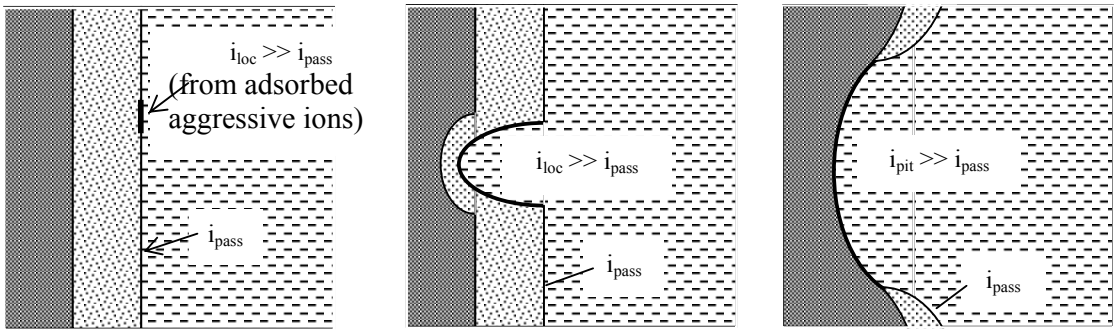

(c) Film breaking mechanism

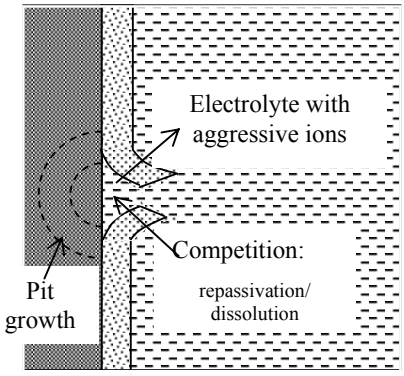

Figure 2.7 Schematic diagram demonstrating pitting initiation at passive film: (a) Penetration mechanism, (b) Adsorption mechanism, and (c) Film breaking mechanism [117].

2.2.2.3.2.Pit initiation at intermetallic particles

In the case of aluminium alloys, many studies have shown that pits initiate at intermetallic particles [104, 108, 124, 125]. Intermetallic particles often have corrosion potentials which differ greatly from the corrosion potential of the aluminium matrix and will cause galvanic corrosion. Both cathodic and anodic intermetallic particles can cause corrosion to aluminium. The mechanism of pit initiation at intermetallic particles will be given in Section 2.2.3.2.

2.2.3 Corrosion of Aluminium Alloys

2.2.3.1 Cathodic reactivity of intermetallic particles

Intermetallic particles contain transition metal whose oxides are semiconductors, and better sites for electrochemical reaction than the matrix which is covered with alumina, which is an insulator [16, 17, 71, 72, 74, 78-82]. . Intermetallic particle are thus preferential sites for the cathodic reactions, particularly oxygen reduction (Figure 2.8). They also frequently show lower active dissolution rates than the matrix [81, 108, 124, 126]. Thus, their corrosion potentials tend to be significantly higher than that of the matrix.

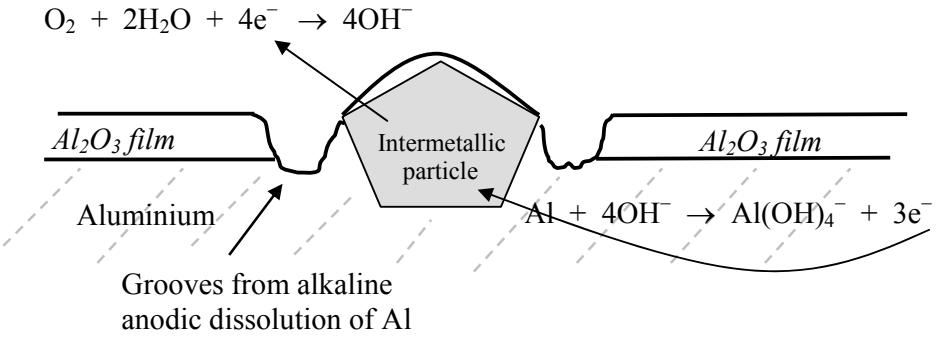

Figure 2.8 Diagram illustrating the formation of grooves around a cathodic intermetallic particle in an unbuffered solution [87].

Because of the local cathodic reactions at intermetallic particles, a local pH increase can develop in the solution around the particle (Equation 2.5). Hydroxide ions disslove the passive film over the aluminium matrix, as shown by Equation 2.9. As a consequence, the film around particle breaks down and developes grooves around the particle.

Generally, iron-containing intermetallic particles such as Al_3Fe, α-AlFeSi, $Al_6(MnFe)$, α-Al(MnFe)Si, Al(MnFeCr) and Al_7Cu_2Fe, are cathodic with respect to the aluminium matrix [16, 19, 39, 78, 79, 81, 126-131]. Corrosion potential measurements on various intermetallic particles and aluminium in a NaCl-H_2O_2 solution (58.5 g NaCl and 9 mL 30% H_2O_2) are shown Table 2.4 [132-134].

Büchler et al. used a fluorescence dye in combination with conventional fluorescence microscopy and near-field scanning optical microscopy to investigate the

localised corrosion behaviour of AA2024 [135] and AA6061 [129]. The fluorescein allowed to identify the cathodic reduction sites.

Table 2.4 Approximate corrosion potential (E_{corr}) of aluminium and some intermetallic particles (mV, SCE) based on ASTM G69 (NaCl-hydrogen peroxide solution) [132-134].

Alloy or metal or intermetallic particles	E_{corr} (mV, SCE)
Al	-760
Al_6Mn	-760
$Al_6(MnFe)$	-763 to -737
$\alpha-Al_{12}(MnFe)_3Si$	-747
Al_3Fe	-470

2.2.3.2 Pit initiation at intermetallic particles

As mentioned earlier, pits can initate at intermetallic particles. Support for the concept of particle-induced pitting corrosion is provided by in situ observations of pit nucleation and growth [108, 124] and post-pitting examinations by scanning electron microscopy [108]. Rynders et al. [81] used in situ AFM to study the corrosion behaviour of Fe-rich intermetallic particles on AA6061 by monitoring shape evolution at the nanoscale near individual, well-characterised intermetallic particles during initial stages of dissolution.

Seri [126] investigated the effect of Al_3Fe intermetallic particles on the pitting behaviour of aluminium alloys and found the extent of dissolution around the intermetallic particles depended on NaCl concentrations and that dilute NaCl solutions (0.01-0.1 M) resulted in greatest dissolution around intermetallic particles.

Intermetallic particles containing Al-Si-Mg found in AA6065 are nucleation sites for pits studied by Guillaumin and Mankowski [83]. It was found that pits first developed within the grains.

Pit initiation in AA2024-T3 was found to occur in the matrix adjacent to intermetallic particles such as AlCuFeMn, which act as cathodes, and Al_2CuMg, which act as anodes [80, 106]. Pitting, however, leads to a preferential dissolution of Mg and Al at Al_2CuMg. The Cu-rich remnants act then as cathodes [80, 82].

2.2.3.3 Role of Solute Content in Corrosion

The corrosion resistance has been enhanced by alloying aluminium with a variety of solute elements, including Mn, Cr, Ta, Mo, W, Ti, Nb, Cu, Si, Zn and V [136-146]. For these alloying additions to be effective, they typically must be in solid solution at concentrations greatly exceeding the equilibrium solubility. Generally, it is found that increased solute content improves pitting resistance [136-146].

Moffat and co workers [136] investigated pitting corrosion of electrodeposited Al-Mn alloys. A supersaturated face-centred cubic (fcc) phase was produced with up to 5 at% Mn. Deposits containing 5-22 at% Mn were composed of a glassy phase in combination with a supersaturated (1 at% Mn) fcc phase, while alloys with 22-26 at% Mn were single-phase metallic glasses. They found that for single phase Al-Mn alloys, the breakdown potential of supersaturated fcc $Al_{97}Mn_3$ is 250 mV greater than that of

aluminium while glassy $Al_{74}Mn_{26}$ exhibits a 400 mV increase. In contrast, the dual phase material exhibited pitting potentials closer to that of aluminium due to selective pitting of the (1 at% Mn) fcc phase. The enhanced pitting resistance of single-phase Al-Mn alloys is remarkable in view of the reactive nature of elemental Mn. They also found that the pitting and repassivation potentials of both aluminium and Al-Mn alloys are separated (E_{pit}–E_{repass}) by less than 50 mV. This small difference suggests that the air-formed oxide film on Al-Mn alloys does not play a main role in the increased pitting potentials observed for these alloys. Rather, manganese acts to hinder the pit growth kinetics associated with aluminium. Frankel et al. [138] found that the repassivation potentials of sputter-deposited Al-Mn alloys are not a strong function of solute concentration. However, Al-Mn alloys pitted at potentials just above their repassivation potentials. Increased Mn content in solid solution improves pitting resistance.

As mentioned earlier, enhanced deformation and annealing on aluminium alloys leads to precipitation with corresponding solute depletion [46-48]. In case of 3XXX series aluminium alloys, enhanced deformation such as hot rolling, cold rolling [11, 14, 18, 147] and grinding [50], leads to preferential precipitation of fine intermetallic particles in the surface layer during high temperature heat treatment. This phenomenon causes depletion of the more noble alloying elements, e.g., Mn, in the matrix in this region, thereby increasing dissolution of the alloy relative to the bulk. Afseth and coworkers [14, 18, 147] investigated the corrosion behaviour of AA3005 hot rolled and cold rolled sheet. It was found that preferential precipitation of a fine dispersion of intermetallic particles of the α-$Al_{12}(MnFe)_3Si$ phase occurred in the surface layer during high temperature heat treatment.

2.2.3.4 Corrosion of 3XXX Aluminium Alloys

For aluminium alloys 3XXX series, belonging to the Al–Mn–Fe–Si system, it is known that the electrochemical properties of the different intermetallic phases are strongly influenced by iron content. High iron content results in electrochemically noble intermetallic particles acting as efficient catalysts for cathodic reactions [17]. The enrichment of iron increases the corrosion potential of the intermetallic particles so that increases the rate of electrochemical reduction process [15, 39]. On the other hand, increasing levels of both manganese and silicon in the intermetallic phases result in a decrease in the rate of the localised reduction reactions [15, 16].

The effect of increasing manganese in the alloy is to increase the manganese in solid solution up to ~0.4% and to increase the manganese concentration in the intermetallic particles. Electrochemically, increasing manganese in solid solution increases the resistance to dissolution, whereas increasing manganese in the intermetallic particles decreases their cathodic reactivity. Decreasing the rate of both anodic and cathodic reactions will therefore decrease the extent of overall corrosion [17].

Nisancioglu [148] has suggested how to improve the corrosion resistance of Al-Mn alloys. He suggested that either small size, low volume fraction of intermetallic phases or high Mn content in the matrix and in the intermetallic phases might improve corrosion resistance of Al-Mn alloys. The former factor reduces the effective area which

catalyses electrochemical reactions of the cathodic nature. The latter factor reduces the galvanic potential difference between the matrix and the intermetallic phases.

2.2.4 Effect of Deformation on Corrosion of Aluminium Alloys

Both hot and cold rolling on aluminium alloys generate the deformed layer and many surface preparation procedures such as grinding, machining, dimpling, sand blasting etc. also generate a deformed layer at the surface [21-24, 50]. This deformed layer has an effect on corrosion resistance [21-23, 50].

As mentioned earlier, the formation of a highly deformed layer at the surface of rolled aluminium alloy sheet results from shear deformation during rolling. Subsequent annealing leads to enhanced precipitation of fine intermetallic particles in the surface layers. These layers have high electrochemical reactivity, in particular, a strong susceptibility to filiform corrosion as will be discussed below [9, 13, 14, 45, 149-151]. This deformed layer also has a detrimental effect on other types of localised corrosion. Ambat et al. [11, 152] investigated the very thin deformed layer in Al-1Mn-0.4Fe-0.3Si model alloy and AA3005 rolled sheet, 1.0 mm thick, and found that both the anodic and cathodic reactivity of the deformed layer, approximately 1 μm, were significantly higher than that of the bulk. An increased number of fine intermetallic particles in the surface layer as compared with the bulk of the materials was consistent with this result.

As mentioned above, not only the deformed layer on rolled aluminium alloys has a detrimental effect on corrosion resistance but also the deformed layer developed on the aluminium surfaces by grinding, machining, and dimpling. Scamans et al. [50] investigated the correlation between the amount of surface deformation induced by various grinding practices and subsequent annealing on corrosion behaviour of hot rolled AA3005. It was found that grinding of aluminium alloys surfaces produces ultra-fine grain sized deformed surface layers with fine intermetallic particles resulting in promoted susceptibility to filiform corrsosion. Leggat and Taylor [153] studied the effect of micron-scale surface deformation on the corrosion behaviour of coil-coated AA5182. They found that dimples were introduced into the coil-coated sheet by feed rollers during can end manufacturing. As a result of micron-scale surface deformation, the damaged oxide film and second-phase precipitation were proposed as the mechanism of increased corrosion susceptibility. Forsyth [22] studied corrosion behaviour on machined surfaces of AA7010 in seawater. It was found that the deformed material is more susceptible to corrosion than the undeformed material. Moreover, any bruising of the machined surface, such as that arising from chip build up and clogging, increased the corrosion susceptibility [21, 22].

2.2.5 Filiform Corrosion of Aluminium Alloys

Filiform corrosion (FFC) is a type of localised corrosion in the form of thread-like filaments that have considerable length but little width or depth, propagating on coated surfaces of steel, aluminium, magnesium and other metals [74, 154, 155]. It was first investigated by Sharman in 1944 [156], first detected on aluminium in 1960's in the aircraft industry [157, 158] and first observed on architectural aluminium in the early 1980's [157-159]. FFC occurs in a high relative humidity, and marine and industrial environments which particularly enhance filament growth [159]. However, Marsh et al. [160] found that FFC can occur on epoxy coated AA3003 H14 under both immersed and humid conditions.

FFC arises from the combined effect of several factors such as a coating defect, oxygen, an aggressive atmosphere, a high relative humidity (between 70% and 95% relative humidity for aluminium), a moderately high temperature, the nature of the substrate, and the pretreatment given to the metal surface [161].

2.2.5.1 Mechanism of Filiform Corrosion

The mechanism of FCC on aluminium is an example of differential aeration cell. A typical filament can be divided into two main areas: the head and the tail. The head contains a salt solution while the tail is composed of dry corrosion products and is

considered an inactive zone. Electrochemical reactions are produced in the head which encloses well defined anodic area at the front and a cathodic area at the rear [29].

2.2.5.1.1 Initiation of Filiform Corrosion

FFC of aluminium alloys usually starts on a bare metal surface at a coating defect such as a cut edge or scratch on which aqueous solution containing aggressive ions (e.g. Cl^-, Br^-, F^-, SO_4^{2-}) can accumulate under conditions of high relative humidity [161]. Then, the metal substrate undergoes slight corrosion by the reaction: $Al \rightarrow A1^{3+} + 3e^-$, concentrated at the oxygen–deficient metal/electrolyte/coating interface, while the reaction: $O_2 + 2H_2O + 4e^- \rightarrow 4OH^-$, predominates on the bare metal. The schematic diagram is shown in Figure 2.9 [162].

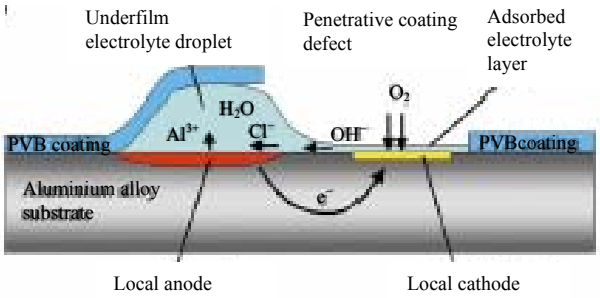

Figure 2.9 Schematic diagram showing the processes involved during the initiation of filiform corrosion on aluminium alloy [162].

As the aqueous solution volume increases, electrochemical processes develop. The oxygen-deficient zone becomes an anode, resulting in the undercutting of coating as

the aluminium dissolution proceeds. Aggressive anions, Cl^- ions, will migrate beneath the delaminated coating to maintain charge neutrality, and water will be drawn in by osmosis to produce an electrolyte droplet [163]. The tail of the filament, where oxygen is readily available, will be the cathode.

2.2.5.1.2 Propagation of the Corrosion Filaments

FFC on aluminium alloys propagates by anodic undermining [163]. The bare metal substrate is oxidised at the front of the head and oxygen is reduced at the rear of the head, as shown schematically in Figure 2.10.

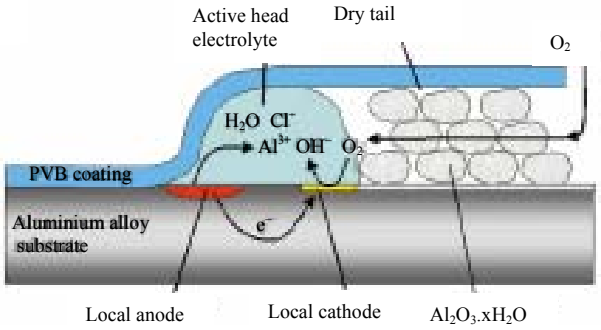

Figure 2.10 Schematic diagram showing the processes involved during the propagation of filiform corrosion on aluminium alloy [162].

Hydrolysis of Al^{3+} ions eventually produces the water insoluble corrosion products, $Al(OH)_3$ and H^+ ions, keeping the anodic site acidic (pH 1-2) [155, 164]. The net cathodic reaction in the tail will keep the tail at a high pH (pH 10) [158, 163]. These electrochemical reactions will cause a driving force for the migration of Cl^- ions towards

the anodic site. Once, the Cl^- ions are in the anodic area at the front of the head. Then, they will drive dissolution of the underlying alloy [165].

The $Al(OH)_3$ corrosion product left behind in the tail region slowly loses water and is converted to porous hydrated aluminium (III) oxide ($Al_2O_3.xH_2O$) [166]. O_2 can diffuse through the porous tail. The tip of the head of the filiform has the lowest oxygen concentration because it has the longest transport path. Combined low pH and oxygen deficiency at the head may result in a secondary cathodic reaction involving hydrogen evolution: $2H^+ + 2e^- \rightarrow H_2$.

Several authors have reported the occurrence of H_2 gas bubbles within filament heads produced on aluminium surfaces [158, 167, 168]. As noted by Slabaugh et al. [167], the small hydrogen bubbles formed depart from the head front and tended to gather as larger bubbles at the back.

The driving force for the directed growth process of FFC is believed to be an oxygen concentration cell between the front and the back of the active head [169]. Therefore, FFC is closely related to crevice and pitting corrosion. The FFC process resembles the growth stage of the pitting corrosion of aluminium alloys. Leth-Olsen and Nisancioglu [170] examined FFC morphologies on a rolled AA3105 coated by wet polyurethane paint after various pretreatment processes. Filaments were shown to propagate by formation of successive pits, in which the exposed intermetallic particles

acted as cathodic sites. Oxygen reducing at these sites diffused to the sites from the tail end of the filaments.

Schmidt and Stratmann [171] investigated FFC on AA2024 by using the scanning Kelvin probe. Results confirmed the galvanic coupling of the active head (anode) with a more active to the cathodically-active tail.

2.2.5.2 Role of the Deformed Layer in Filiform Corrosion

The FFC behaviour of rolled aluminium alloys is controlled predominantly by the presence of a heavily deformed layer at the alloy surface comprising fine alloy grains with oxide-decorated boundaries with fine distribution of intermetallic particles [9, 20, 149-151, 172]. Poor FFC resistance is related to the presence of a higher density of fine intermetallic particles in the surface layers than in the underlying bulk [13, 14]. It is suggested that enhanced secondary precipitation of intermetallic particles in the deformed layer during high temperature exposure, e.g., during hot rolling or annealing steps, is the main contributing factor to the observed poor FFC resistance [14].

Afseth et al. [13] studied the effect of thermo-mechanical processing on FFC of AA3005. They found that hot rolled material showed poor FFC resistance and that heat treatment of both the as hot rolled and subsequently cold rolled samples resulted in a drastic loss of corrosion resistance. TEM investigation of the AA3005 cold rolled sheet revealed a highly deformed near-surface region with approximately 1 μm thickness as

shown in Figure 2.11, which was caused by shear deformation of the surface during rolling. A drastic loss of FFC resistance of this alloys takes place as a result of annealing at temperatures in excess of 350°C [14].

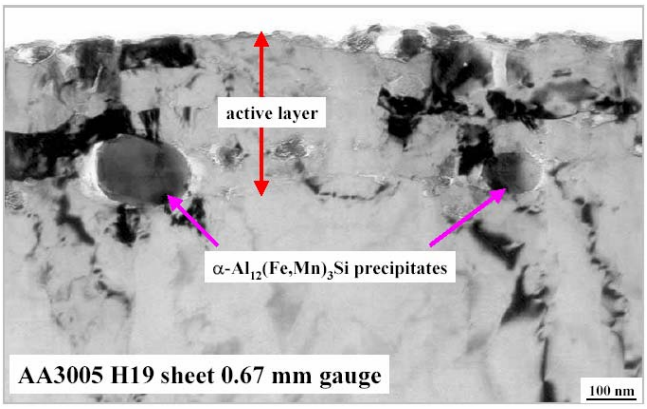

Figure 2.11 TEM micrograph of a highly deformed near-surface region with approximately 1 μm thickness on AA3005 [173].

FFC of cold rolled sheets of binary aluminium model alloys of the systems Al-Mn and Al-Fe was investigated by Afseth and co-workers [174]. They found that the presence of secondary precipitates is a necessity for FFC to occur. Supersaturated solid solution alloys of Al-Mn or Al-Fe systems did not support FFC. Heat treatment of Al-Mn alloy results in precipitation of Al_6Mn, which has electrochemical properties similar to that of the aluminium rich matrix. It did not impair the corrosion properties. However, heat treatment of Al-Fe alloy caused precipitation of Al_3Fe resulting in extensive FFC.

FFC resistance may be readily achieved by removing the deformed, electrochemically reactive, surface layer using the appropriate surface treatment [149]. Zhou et al. [23] investigated the effect of surface treatment on FFC of AA5004 sheet.

They found that the near surface microstructure significantly influenced FFC susceptibility. As-rolled and mechanically ground alloy surfaces (Figure 2.12(a) and (b)) that have heavily deformed layers, are susceptible to FFC. A high FFC resistance results from removal of the deformed layer by appropriate cleaning of the surface by caustic etching, caustic etching and desmutting, or acid cleaning as shown in Figures 2.12(c), (d) and (e).

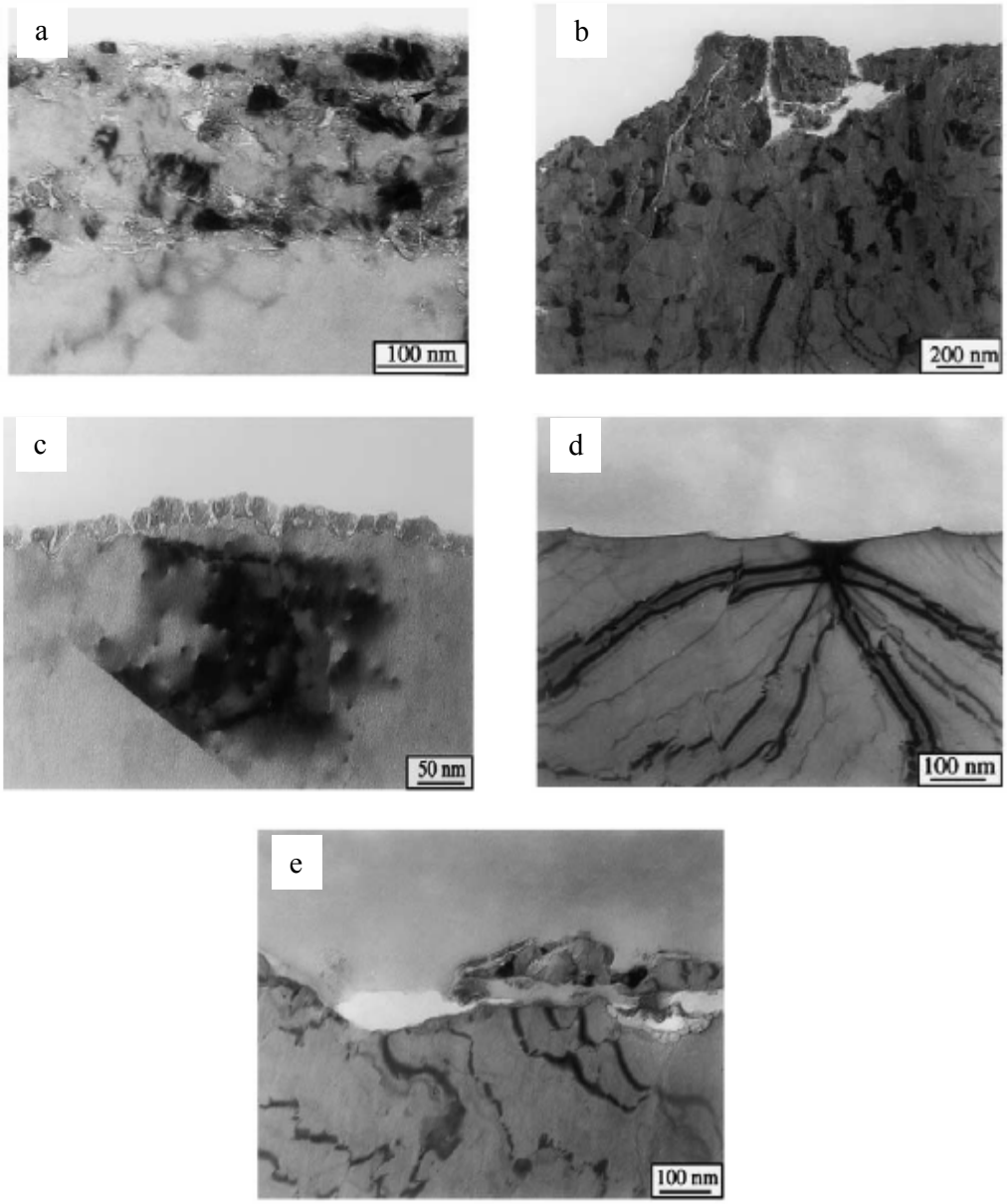

Figure 2.12 Transmission electron micrographs of ultramicrotomed cross sections of the AA5004 H14: (a) as-rolled; (b) mechanically ground; (c) caustic etched; (d) caustic etched and desmutted; (e) acid cleaned [23].

2.3 Surface Finishing of Aluminium Alloys

Surface finishing treatments are generally designed to minimise the corrosion susceptibility of surfaces. Most aluminium alloys are subjected to surface finishing in order to provide a clean and corrosion-resistant surface for subsequent treatment with conversion coating and paint [175]. In order to obtain a strong and stable bond between the metal and the paint, the naturally formed surface oxide on aluminium has to be removed and replaced with a new, continuous, solid, and corrosion resistance oxide layer [176, 177].

Traditional surface cleaning involves the use of organic solvents to remove any lubricant, alkaline cleaners such as sodium hydroxide to remove the oxide and any deformed layers, and acid cleaners such as nitric acid to deoxidise and desmut the surface [175].

2.3.1 Degreasing

Degreasing removes organic contaminants, such as oils and greases as well as solid dirt particles from surfaces [175]. Non-inflammable chlorinated hydrocarbon solvents, such as trichloroethane, trichloroethylene, tetrachloroethylene has been employed for vapour degreasing [175, 178]. Organic solvents such as acetone, ethanol, methyl-ethyl-ketone (MEK) are also used for degreasing [179]. Recently, organic solvents are being replaced by water-based cleaners such as Brulin 815 DG (an alkaline cleaner), Parker Amchem Ridoline 53 (a slicated alkaline cleaner), Sanchem 500 (a non-

silicated mild alkaline cleaner), and Novaclean 120 (a mildly alkaline solution containing surfactants) for environment reasons [180, 181].

2.3.2 Alkaline Etching

Alkaline pretreatment has been used for surface cleaning of aluminium and its alloys prior to electrograining, anodising, conversion coating etc. for architectural, automotive, aerospace and packaging applications [39]. Alkaline cleaners such as sodium hydroxide remove the oxide and any thin deformed layer form cold rolling. However, the cleaning process builds up a layer on the surface containing a concentration of alloying elements [182]. It leaves a black smut on the surface [178] which in the case of AA2024 and AA7016 leads to a dramatic enrichment of the surface with copper [182, 183].

Alkaline etching produces changes in the microstructure, morphology, chemistry, and composition of the surface. Koroleva et al. [39, 184] found that during alkaline etching of high purity aluminium, the dissolution of aluminium proceeds through dissolution of the oxide film present on the surface. For Al-Mn alloys, fine scalloped textures are generated on the surface after etching. An increase in etching time increases the dissolution of aluminium, but does not change the apperance of the texture. Moreover, the rate of aluminium dissolution increases with the temperature of the alkaline solution, resulting in transformation of the scalloped texture into a continuous and distinct cellular texture with increased cell sizes [184]. They also found that silicon-containing phases such as α-AlFeSi, α-AlFeCuSi, and α-AlMnSi dissolve more slowly

than the aluminium matrix in sodium hydroxide solution. Al_3Fe, $Al_6(MnFe)$, and $Al_6(MnCu)$ dissolve at a similar rate to the aluminium matrix, whereas the Al_3Mn phases dissolve at a faster rate than the matrix [39]. Lunder and Nisancioglu and Leth-Olsen et al. [20, 182] studied NaOH etched aluminium surfaces. They found that alloying components that accumulated in the oxide developed over the matrix had a detrimental effect on corrosion resistance.

2.3.3 Desmutting or Deoxidising

Desmutting or deoxidising is commonly used as part of multistep pretreatment processes before conversion coating or anodising. It is included to remove surface intermetallics and a layer left by alkaline cleaning, which comprises basic oxides and aluminosilicates [175].

Hughes et al. [185] studied deoxidation of AA2024 T3 with various acids. They found that HNO_3, H_2SO_4, and H_3PO_4 treatments showed very little attack observed on either the constituent particles or the matrix. Iron, magnesium, and manganese were preferentially dissolved from the surface, leaving an insoluble copper rich smut. The exceptions were the HNO_3 combinations, leaving a surface free of copper rich smut.

Chapter 3 Experimental Method

This work focuses on the electrochemical behaviour of Al-Mn alloys affected by deformation and surface preparation. This work aims to study the effect of surface preparation on the electrochemical behaviour of an Al-1Mn-0.4Fe-0.3Si model alloy in the form of cold rolled sheet. The electrochemical behaviour of the active deformed layer on the surface of a comercial AA3005 alloy cold rolled sheet will be investigated. To simulate the high deformation in deformed layers in a bulk material, the deformed structures produced by using uniaxial compression and equal channel angular extrusion (ECAE) on an as-cast Al-1Mn-0.5Fe-0.4Si model alloy will be investigated.

3.1 Materials

3.1.1 Composition

The materials used for this investigation were a 3XXX analogue model Al-Mn-Fe-Si alloy and a commercial 3005 alloy, which were supplied by Alcan International. The chemical composition of the alloys given by the manufacturer is shown in Table 3.1.

Table 3.1 Nominal composition of the Al-Mn-Fe-Si model alloy and the commercial 3005 alloy (wt%) supplied by Alcan International

Alloys	Element (wt%)								
	Mn	Mg	Fe	Si	Cu	Cr	Zn	Ti	Al
Model	1.0	-	0.4	0.3	-	-	-	-	Bal.
AA3005	1.12	0.55	0.39	0.12	0.008	0.007	0.010	0.005	Bal.

The model Al-Mn-Fe-Si alloy in the form of cold rolled sheet (~1.0 mm thickness) was used for the investigation of surface preparation, while that in the form of as cast billet with approximate dimension of 80×125×24 mm^3 was used for the study of the effect of uniaxial compression and ECAE (equal channel angular extrusion) processing. The 3005 alloy in the form of cold rolled sheet (~0.67 mm thickness) was used for the investigation of active surface layers.

3.1.2 Heat treatment

The model Al-Mn-Fe-Si alloy in the form of cold rolled sheet was solution heat treated at 635°C for 2 h and water quenched, while that in the form of cast billet was solution heat treated at 635°C for 10 h and water quenched. Then, they were annealed at 400°C for 2 h and furnace cooled in order to precipitate intermetallic particles.

The commercial 3005 alloy rolled sheet was annealed at 450°C for 2 h and slowly cooled in the furnace to obtain maximum precipitation of intermetallic particles [14].

3.2 Investigation of the effect of deformation

The effect of deformation on precipitation of intermetallic particles and its effect on corrosion behaviour were investigated in the Al-Mn-Fe-Si model alloy by uniaxial compression to different levels and by ECAE.

3.2.1 Uniaxial compression

Uniaxial compression was carried out on a cube sample (10×10×10 mm) which was solution heat treated at 635°C for 10 h and water quenched prior to deformation. Each specimen was then uniaxially compressed by using a servo-hydraulic testing machine at a ram speed 0.2 mm/min. Specimens were deformed to 10%, 25%, 50% and 80%. Then, they were annealed at 400°C for 2 h and furnace cooled in order to precipitate intermetallic particles.

3.2.2 Equal channel angular extrusion (ECAE)

For studying the effect of deformation by ECAE, the model Al-Mn-Fe-Si alloy billet was solution heat treated at 635°C for 10 h and water quenched. Cylindrical rods of 15 mm diameter and 100 mm length were prepared from the homogenised billet (Figure 3.1).

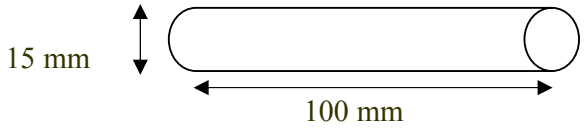

Figure 3.1 Cylindrical rod of model Al-Mn-Fe-Si alloy

ECAE processing was carried out at the Manchester Materials Science Centre. The die angle for the extrusion was $2\phi = 120°$ as given in Figure 3.2. ECAE processing was performed at room temperature without any rotation between passes using colloidal graphite as a lubricant. The rods were pressed with a ram speed 40 mm/min. The cycle was repeated each time, ensuring that the sample remained in the same orientation on each pass. Samples were pressed 3, 10 and 15 times. Following ECAE processing, the rods were heat-treated at 400°C for 2 h and furnace cooled in order to homogenise and to assist precipitation of intermetallic particles. Then, the rods were sectioned perpendicular to the extrusion direction to study the effect of deformation.

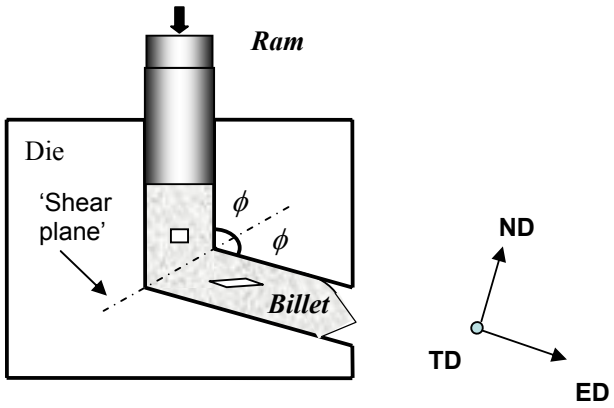

Figure 3.2 Schematic diagram representing the ECAE process, showing how the die's 'shear plane' rotates through an angle of 120°. ED is the extrusion direction, TD is the transverse direction normal to the page and ND is the vertical direction relative to the billet's axis in the die's symmetry plane [57].

3.3 Surface preparation

The following conditions of surface preparation (Table 3.2) were used in the present study to evaluate the effect of the surface preparation on the electrochemical behaviour of the model Al-1Mn-0.4Fe-0.3Si alloy.

Table 3.2 Surface preparation

Condition	Symbol	Surface preparation method
1	As received + HNO_3	as received + acetone 2 min* + concentrated HNO_3 30 s + rinsed in deionised water
2	1 μm + HNO_3	ground with 1200 grit SiC paper + polished with 6 μm diamond paste + polished with 1 μm diamond paste + acetone 2 min* + concentrated HNO_3 30 s + rinsed in deionised water
3	1 μm, etched 45 s + HNO_3	ground with 1200 grit SiC paper + polished with 6 μm diamond paste + polished with 1 μm diamond paste + acetone 2 min* + etched in 2.5 M NaOH 60°C for 45 s + concentrated HNO_3 30 s + rinsed in deionised water
4	1200 SiC + HNO_3	ground with 1200 grit SiC paper + acetone 2 min* + concentrated HNO_3 30 s + rinsed in deionised water
5	1200 SiC, etched 45 s + HNO_3	ground with 1200 grit SiC paper + acetone 2 min* + etched in 2.5 M NaOH 60°C for 45 s + concentrated HNO_3 30 s + rinsed in deionised water
6	1200 SiC, etched 270 s + HNO_3	ground with 1200 grit SiC paper + acetone 2 min* + etched in 2.5 M NaOH 60°C for 270 s + concentrated HNO_3 30 s + rinsed in deionised water
7	GDOES + HNO_3	sputtered by glow discharge optical emission spectroscopy (GDOES) for 200 s + acetone 2 min* + concentrated HNO_3 30 s + rinsed in deionised water
8	1 μm	ground with 1200 grit SiC paper + polished with 6 μm diamond paste + polished with 1 μm diamond paste + acetone 2 min*
9	1200 SiC	ground with 1200 grit SiC + acetone 2 min*
10	GDOES	GDOES sputtered for 200 s (3.6 μm depth) + acetone 2 min*

Note: *Degreasing in acetone was performed in an ultrasonic bath for 2 minutes.

For the investigation of the effect of deformation on the corrosion behaviour of the Al-Mn-Fe-Si model alloy, the specimens were prepared by method 2. The size of these specimens was 15×15×1 mm^3.

The electrochemical behaviour of the active surface layer on commercial rolled AA3005 sheet was profiled at different depths using GDOES (glow discharge optical emission spectrometry) sputtering (model no: JY 5000 RF). GDOES allows rapid elemental depth profiling at low vacuum. It is applicable to conductive and non-conductive substrates, with a depth resolution of ~5 nm with ~50 μm depth capacity. The sample surface was sputtered with argon ions. The sputtering rate was ~2 μm/min. The GDOES sputtering was acquired using the following parameters:

Method parameters:

Analysis mode:	Normal
High dynamic detection:	No 24
Centre line:	Al 396
Flushing time:	20 s
Preintegration time:	30 s
Measurement time:	3-150 s

RF Generator:

Pressure:	500 Pa
Power:	28 W
Module:	500

Phase:	480
Duty cycle:	1

The as-received material was annealed at 450°C for 2 h and furnace cooled to obtain maximum precipitation of intermetallic particles. The annealed samples were etched to different depths, 0.02, 0.13, 0.4, 1 and 2 μm, with GDOES.

For all the corrosion experiments of the active surface layer on commercial rolled AA3005 sheet, only the crater area was exposed (0.13 cm^2) with the other area lacquered. Before lacquering, the specimens were degreased in acetone for 2 minutes and immersed in concentrated HNO_3 for 30 s, followed by rinsing in deionised water.

3.4 Microstructural characterisation

3.4.1 Hardness measurements

Hardness measurements were made using a Mitutoyon MVK-H1 Vickers microhardness tester. The samples were mounted using cold mounting resin and ground to a 1200 grit finish on SiC paper and then polished using 6 μm diamond paste. The hardness was measured using 50 g load and readings were taken in 9 different areas on the sample. Three measurements were made on each area. The schematic diagram

indicated the location of microhardness measurements is shown on Figure 3.3. This was made for ECAE samples.

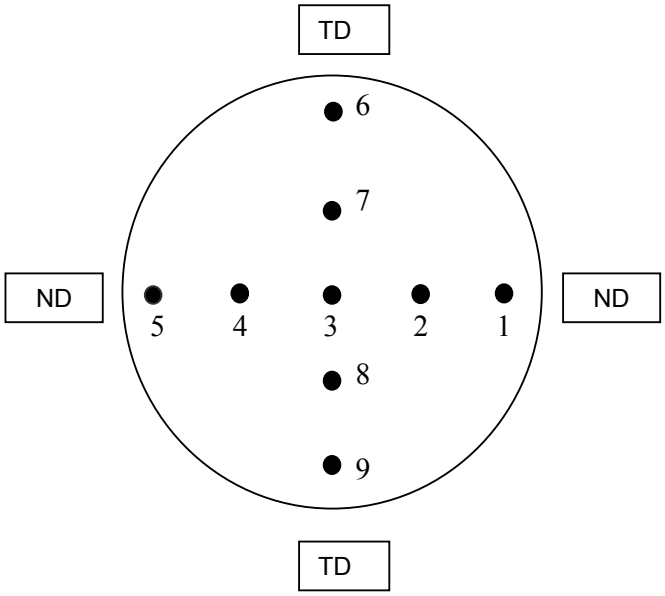

Figure 3.3 Schematic showing areas where hardness measurements were taken (TD is transverse direction and ND is the vertical direction relative to the billet's axis in the die's symmetry plane as defined in Figure 3.2)

3.4.2 Thermoelectric power measurements

The manganese content in the matrix of the Al-Mn-Fe-Si model alloy after different levels of ECAE processing and heat treatment was determined using thermoelectric power (TEP) measurements at Alcan International. The thermoelectric effects are associated with the flux of electrons when a material is subjected to electrical potential gradients or to temperature gradients [46]. Thermoelectric power is a proportionality coefficient between both the electron flux and the gradients used to measure the TEP of metals and alloys with respect to a reference metal. TEP depends

only on the nature of the materials involved and not on their form. High purity aluminium was used as a reference metal in this study. The calculation of %Mn in solid solution was made using values for specific resistivity and specific thermoelectric power as reported by Borrelly et al. [186].

3.4.3 Microscopy

Scanning interferometry

The surface topography, surface roughness profiles of the samples after surface preparation under different conditions (1-7, as described in Table 3.2) and depth calibration of the GDOES crater were carried out using a Wyko vertical scanning interferometry (VSI) surface profiler.

Scanning electron microscope (SEM)

Scanning electron microscopy (JEOL 5410, JEOL 6300 and Philips XL 30) was used for microstructural characterisation of the surface morphology before and after corrosion testing. An epoxy replica technique was employed to study the internal structure of the pits [110, 187]. The sample was placed in a mounting cap in a desiccator, which was evacuated using a rotary pump. A mixture of Epofix resin and hardener was poured on to the cup under vacuum and air was slowly admitted. After curing the epoxy, the specimen was immersed in 2.5 M NaOH solution at room temperature to dissolve the

aluminium. Then, the replica of the corroded surface was coated with gold for examination by SEM.

The chemical composition of intermetallic particles was analysed using energy dispersive spectroscopy (EDS) with a Vantage system attached to the SEM JOEL 6300. The accelerating voltage of the SEM was set up at 15 kV with a 15 mm working distance. The correction method used for the quantitative analysis was ZAF (Z = atomic number, A = absorption, and F = fluorescence).

In order to quantify the distribution of intermetallic particles on the surface of the alloys, the samples were polished to 1 μm. Backscattered electron images were obtained in order to achieve high contrast between the particles and the matrix. A total 50 random images were taken for each sample, corresponding to a studied area of 0.5 mm^2. Intermetallic particles of 1 μm diameter or more were counted, using KS300 image analysis software.

Crystallographc orientation

The crystallographic orientation of individual grains was obtained using electron backscattered diffraction (EBSD) on the SEM JEOL 840A operating at 20 kV with the sample tilted at 70° toward the EBSD detector. The crystal orientation maps were automatically generated by Inca software.

3.4.4 Surface analysis

Auger surface depth profile measurement

The oxide film thickness and the surface composition were determined by Auger spectroscopy, (Escalab II, V.G. Scientific.). The surface depth composition profile can be generated by Auger analysis combined with argon ion sputtering. The sputtering rates or depths were calculates by comparison with a known standard.

The samples were cut into 1×1 cm^2 section, then ground down to a 1200 grit finish on SiC paper and polished with 6 μm and then 1 μm diamond paste, respectively.

Auger analysis experiment were performed under a base pressure of 10^{-9} mbar. Auger spectra were collected using a 5 kV primary electron beam with a current of 150 nA. The scanning ion gun was operated at 3 kV in argon gas at 10^{-5} mbar using a current density of 1.25 $\mu A/cm^2$. The etch rate was ~0.2 nm/min which has been calculated from a standard silicon overlay on titanium.

An initial spectrum was collected for each sample before sputtering to characterise the as-received surface. Subsequent spectra were then collected, in a cyclic manner. A series of scans separated by a sputter rate enables the presence of thin surface films to be detected and characterised. Data acquisition was then continued using simultaneous

analysis and sputtering to remove material at an increased rate. The survey scans were acquired using the following parameters:

Energy range	20-750 eV
Step size	1.0 eV
No of scans / depth	10
Dwell time	0.1 seconds
Pass energy (CRR)	4
Source	MCD3

3.5 Electrochemical measurements

3.5.1 In-situ observation of corrosion

The corrosion behaviour of Al-1Mn-0.4Fe-0.3Si alloy with different surface preparations and AA3005 rolled sheet that had been etched to different depths with GDOES was monitored in 1 M HCl using a video camera attached to an optical microscope.

3.5.2 Potentiodynamic polarisation

Anodic and cathodic sweeps were carried out in order to characterise the surface of the alloy using a "flat cell" with an exposed surface area of 0.19 cm^2 defined by a Viton o-ring pressed against the metal. The flat cell contained 350 ml of the electrolyte,

0.85 M NaCl acidified to pH 3 by addition of acetic acid, using a standard three-electrode configuration. A saturated calomel reference electrode and a platinum counter electrode were used, as shown in Figure 3.4.

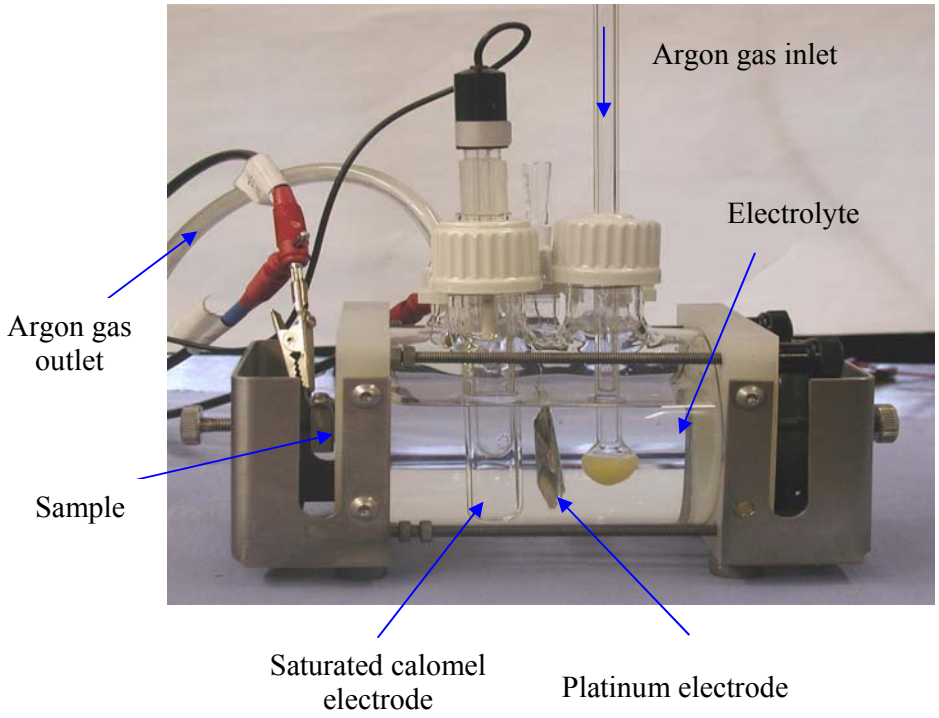

Figure 3.4 Flat cell

The OCP (open circuit potential) was measured for 5 minutes before potentiodynamic sweeps were carried out. Electrochemical measurements were performed with a Solartron Corrosion Measurements System (Model No. 1285).

The anodic and cathodic sweeps were carried out at a scanning rate of 1 mV/s from the OCP. A fresh sample was used for each measurement. In order to correlate the corrosion attack on different specimens, the anodic polarisation curves were stopped

at -0.5 V(SCE). For all anodic sweeps, the solution was de-aerated with argon gas for 30 minutes prior to the first experiment and for 15 minutes between subsequent experiments. The cathodic polarisation sweeps were carried out in naturally aerated solution stopped at potential -1.25 V(SCE). All measurements were carried out at room temperature.

3.5.3 Potentiostatic polarisation

The samples were prepared then treated as required (see Section 3.3). Potentiostatic measurements were performed in a de-aerated solution of 0.85 M NaCl pH 11.5 at an applied potential of –1.0 V(SCE) in the flat cell.

All electrochemical experiments were carried out at least twice to assess the reproducibility.

Chapter 4 Effect of Surface Preparation on Electrochemical Behaviour of Al-1Mn-0.4Fe-0.3Si

4.1 Microstructure of alloy

The microstructure of the model alloy Al-1Mn-0.4Fe-0.3Si cold rolled sheet after solution heat-treatment and subsequent annealing is shown in Figure 4.1.

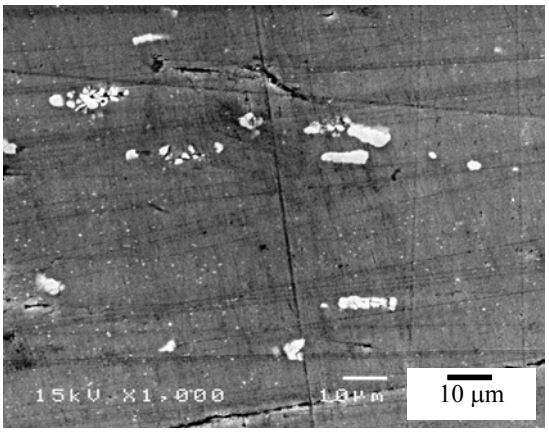

Figure 4.1 SEM image of solution heat-treated and subsequently annealed Al-1Mn-0.4Fe-0.3Si cold rolled sheet.

About 150 intermetallic particles with a size more than 1 μm were analysed with EDX and found to contain Fe, Mn and Si. A typical example is shown in Figure 4.2. Figures 4.3–4.5 show the concentration of Mn vs. Fe, Mn vs. Si and Fe vs. Si, respectively, in the intermetallic particles. The average %Mn, %Fe and %Si are 13% ± 2%, 10% ± 2%, and 8% ± 1%, respectively. The iron to manganese ratio is 0.8 ± 0.2.

This composition is close to α-$Al_{12}(Fe,Mn)_3Si$ phase, which was also found in a rolled AA3005 analogue model alloy (Al-1Mn-0.5Mg-0.4Fe-0.3Si), studied by Afseth and co-workers [45]. They found that this alloy contains only α-$Al_{12}(Fe,Mn)_3Si$ phase with an iron to manganese ratio of 0.7.

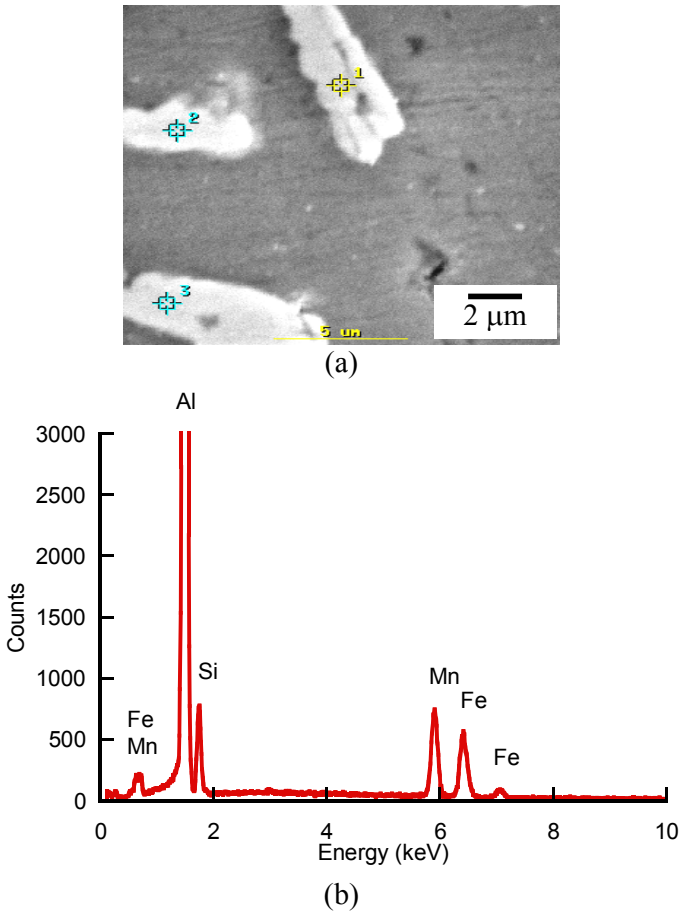

Figure 4.2 Particle analysis for Al-1.0Mn-0.4Fe-0.3Si cold rolled sheet after solution heat-treatment and subsequent annealing: (a) SEM picture and (b) EDX spectrum of particle 1.

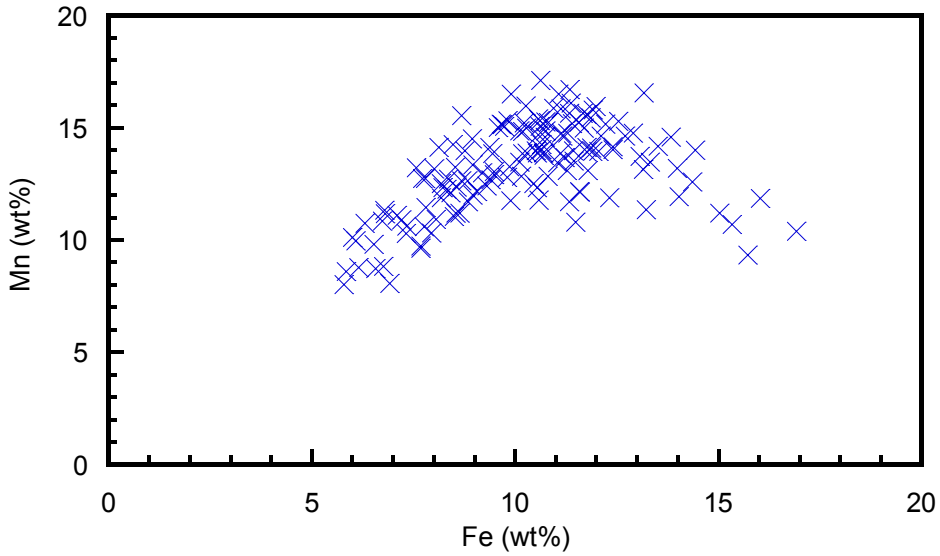

Figure 4.3 %Mn vs. %Fe in intermetallic particles of Al-1Mn-0.4Fe-0.3Si cold rolled sheet after solution heat-treatment and subsequent annealing determined from EDX.

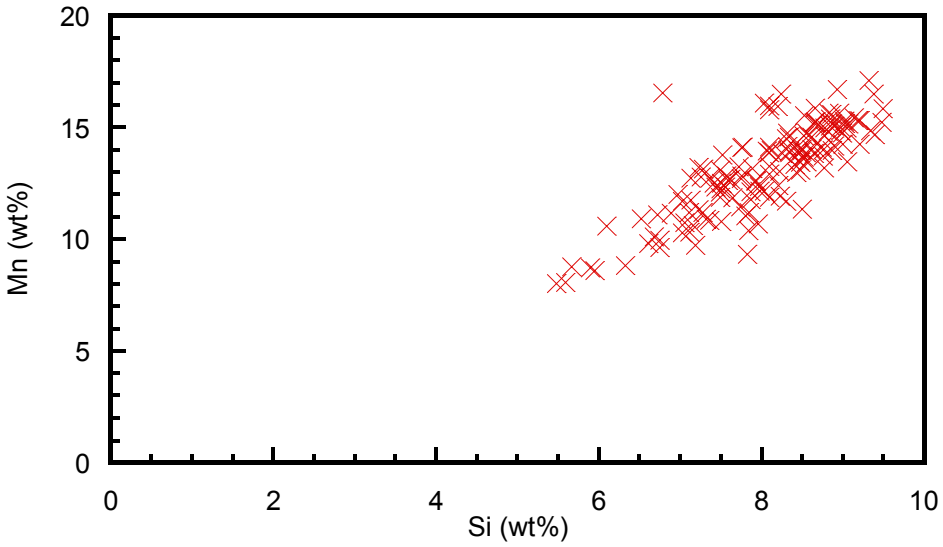

Figure 4.4 %Mn vs. %Si in intermetallic particles of Al-1Mn-0.4Fe-0.3Si cold rolled sheet after solution heat-treatment and subsequent annealing determined from EDX.

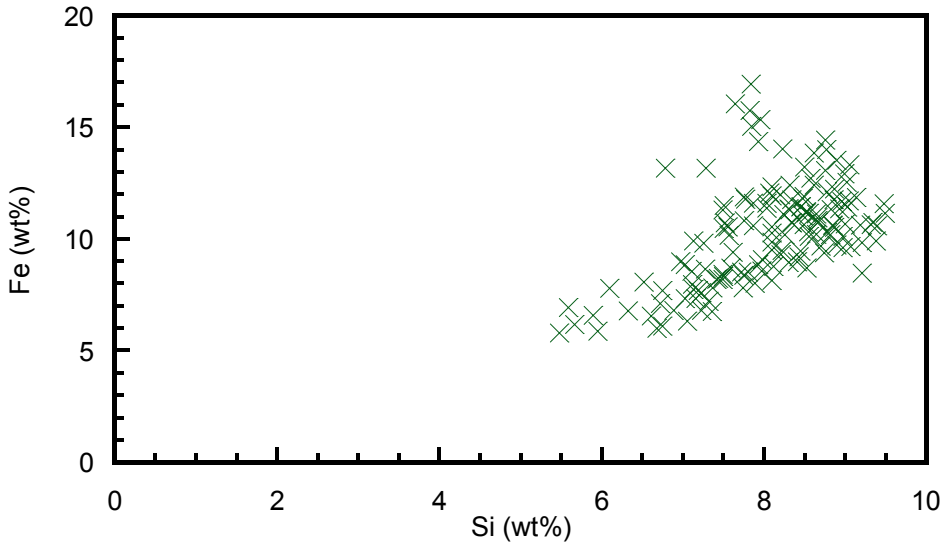

Figure 4.5 %Fe vs. %Si in intermetallic particles of Al-1Mn-0.4Fe-0.3Si cold rolled sheet after solution heat-treatment and subsequent annealing determined from EDX.

4.2 Characterisation of the alloy surface after different surface treatments

4.2.1 Topography of prepared surface

The SEM pictures, surface topography and surface roughness profiles of the samples after surface preparation under different conditions (1–7, as described in Section 3.3 and Table 3.2) are shown in Figures 4.6–4.12. The surface roughness was determined using a white light interference microscope (Wyko). It is quoted as the root-mean-square roughness, Rq, and values are shown in Table 4.1. Rq(X) and Rq(Y) are measured in two perpendicular directions on the surface.

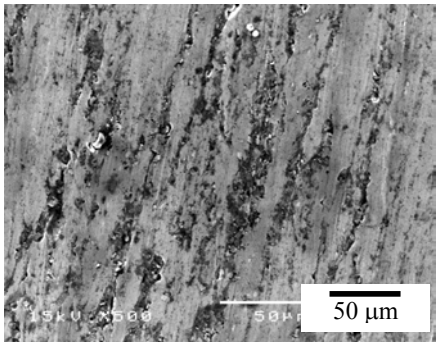

(a)

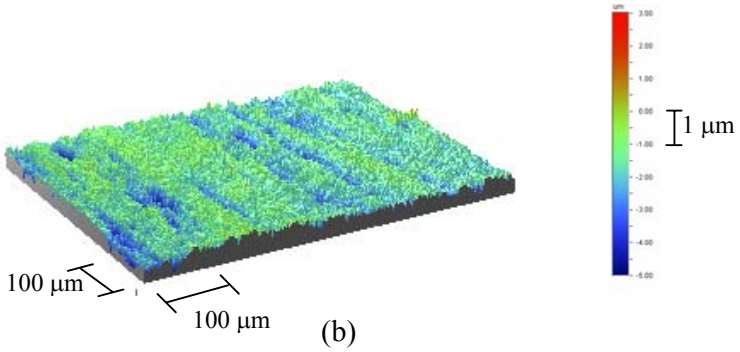

(b)

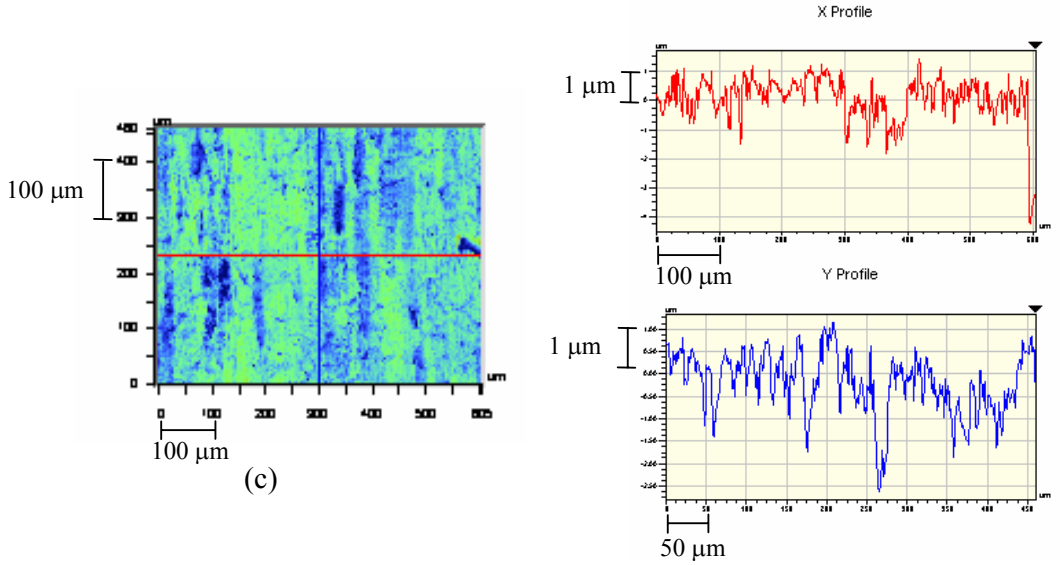

(c)

Figure 4.6 Surface morphology of the as received sample after degreasing in acetone and dipping in concentrated HNO_3: (a) SEM image, (b) surface topography and (c) surface roughness profile (y-axis is the rolling direction).

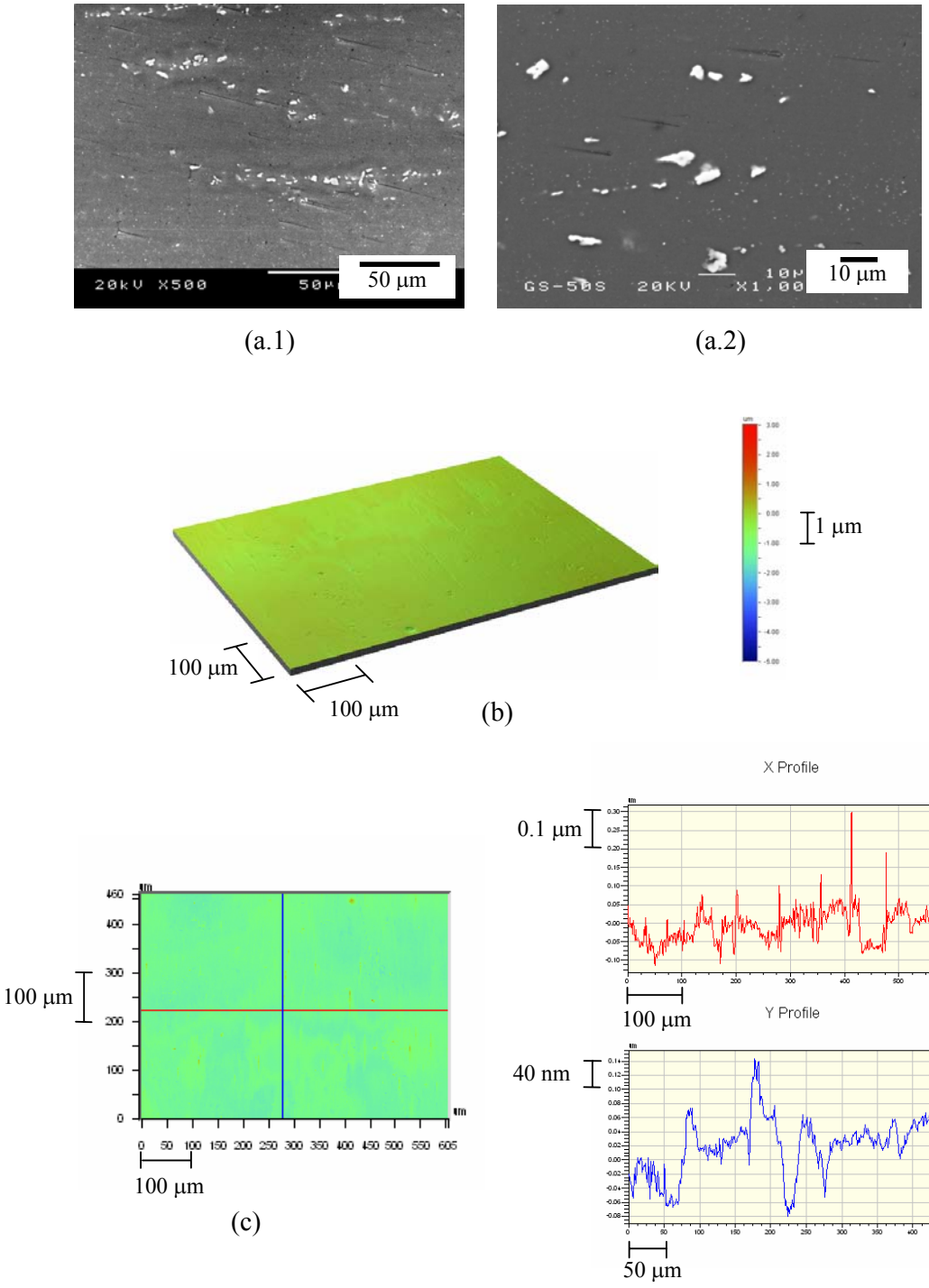

Figure 4.7 Surface morphology after polishing with 1 µm diamond paste, degreasing in acetone and dipping in concentrated HNO_3: (a.1) SEM image, (a.2) BS-SEM image, (b) surface topography and (c) surface roughness profile.

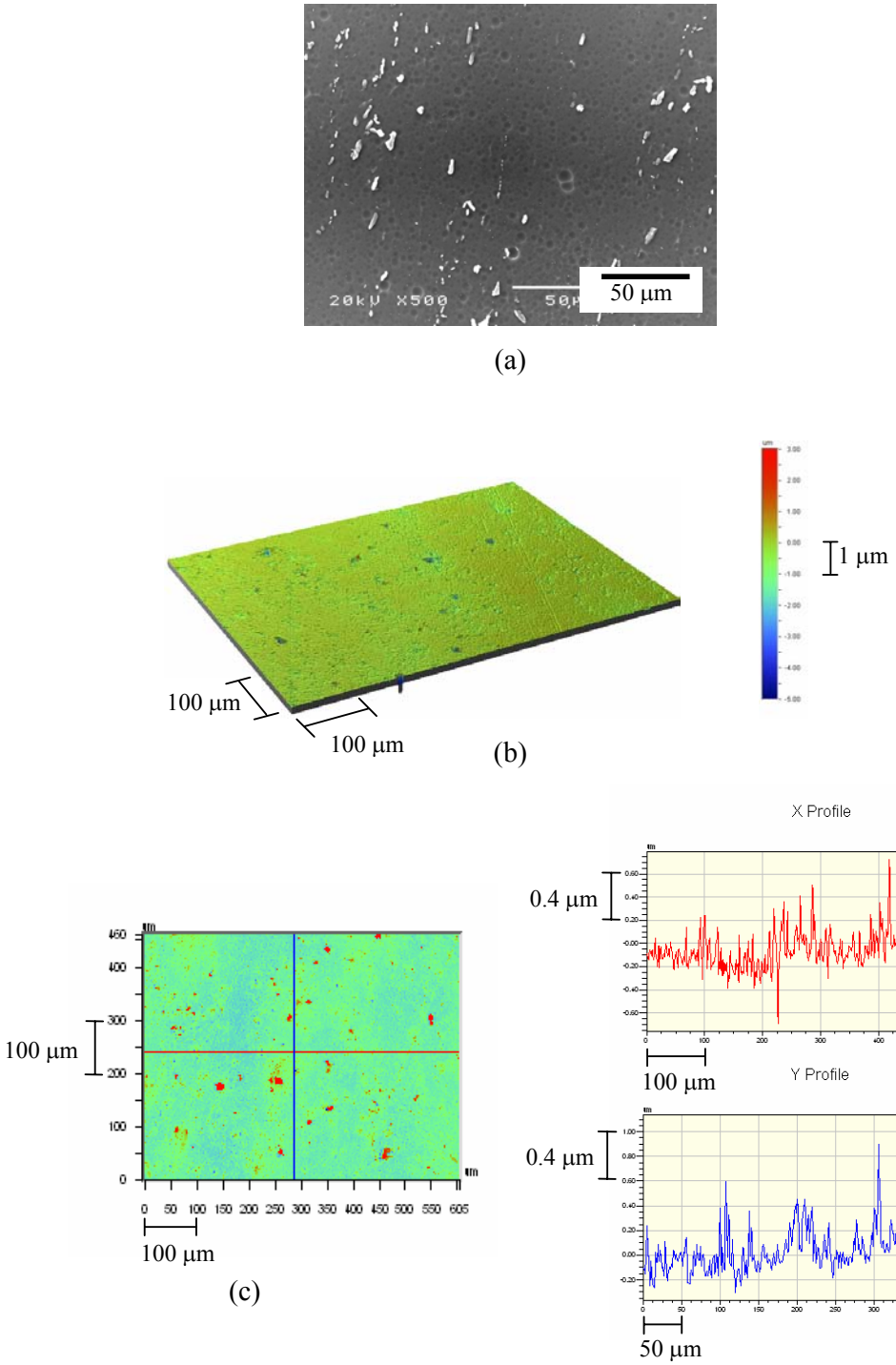

Figure 4.8 Surface morphology after polishing with 1 µm diamond paste, degreasing in acetone, alkaline etching for 45 s, and desmutting in concentrated HNO_3 for 30 s: (a) SEM image, (b) surface topography and (c) surface roughness profile.

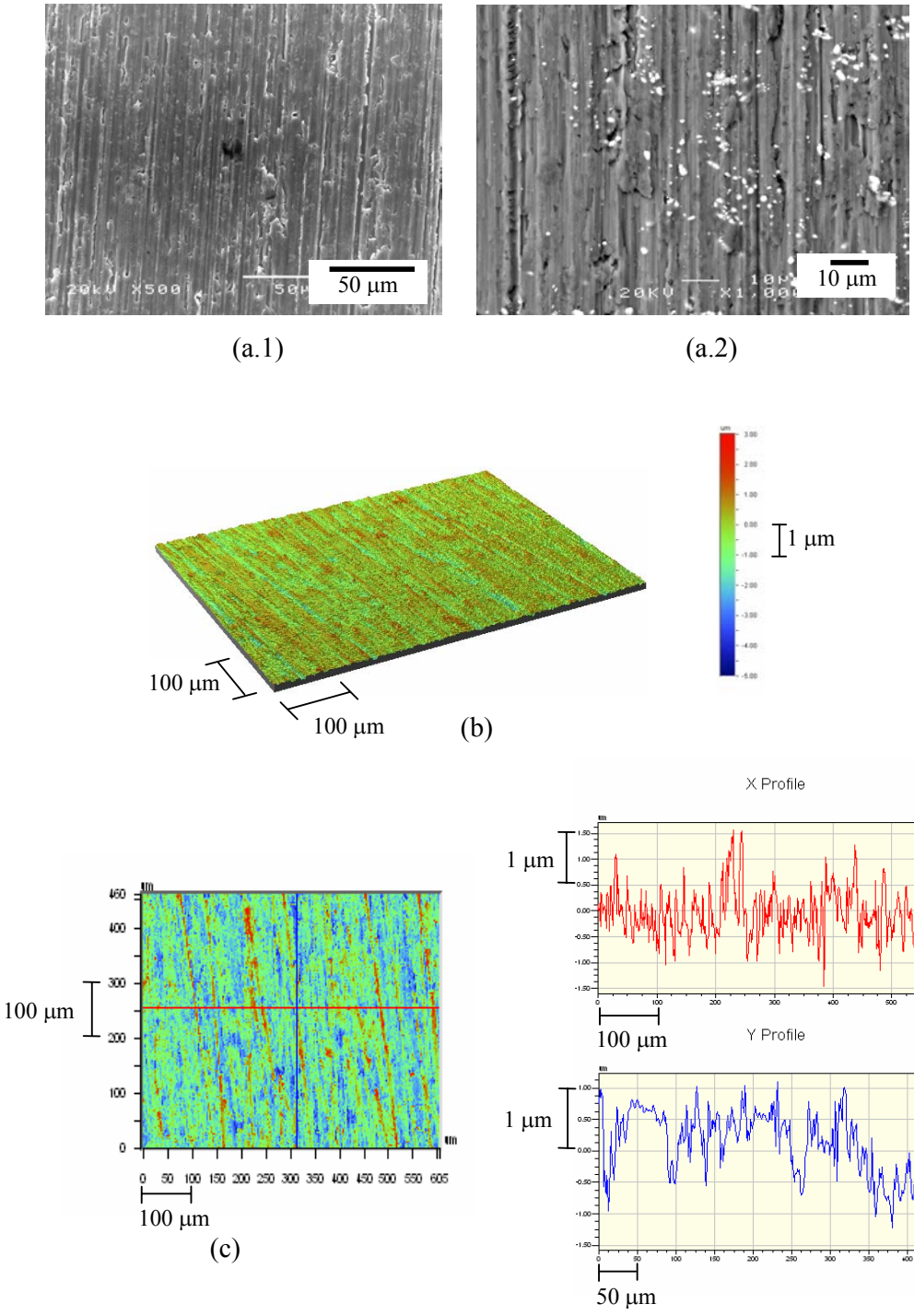

Figure 4.9 Surface morphology after grinding with 1200 SiC paper, degreasing in acetone and dipping in concentrated HNO_3: (a.1) SEM image, (a.2) BS-SEM image, (b) surface profile and (c) surface roughness topography.

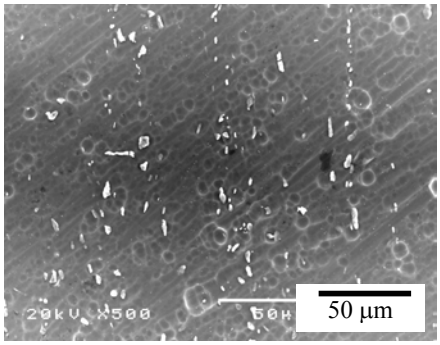

(a)

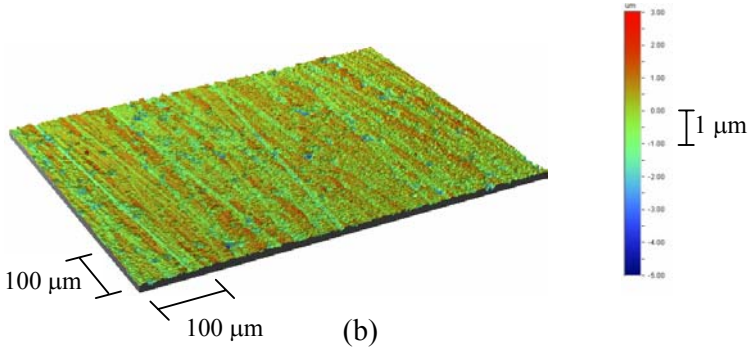

(b)

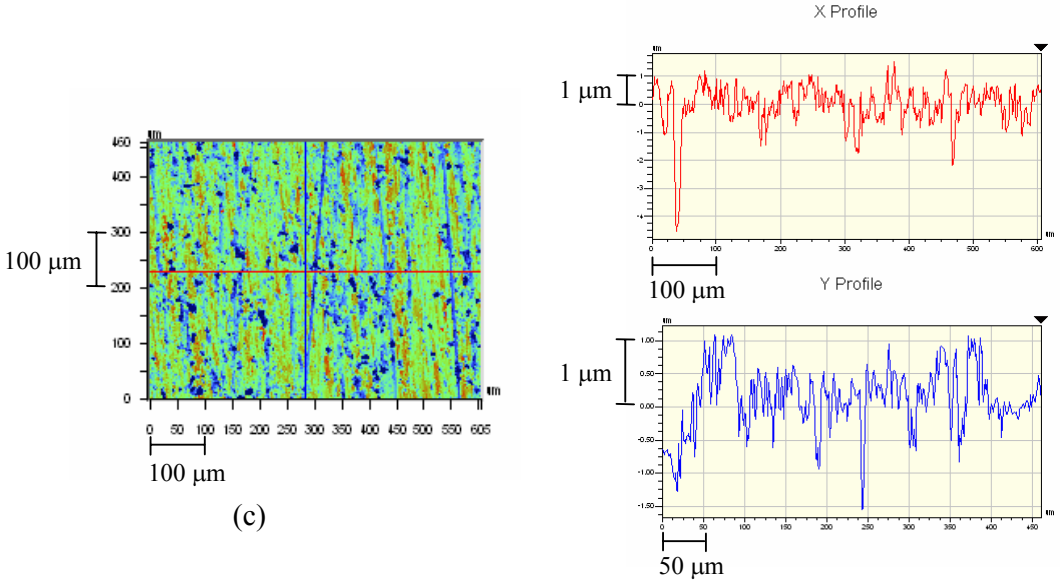

(c)

Figure 4.10 Surface morphology after grinding with 1200 SiC paper, degreasing in acetone, alkaline etching for 45 s and desmutting in concentrated HNO_3 for 30 s: (a) SEM image, (b) surface profile and (c) surface roughness topography.

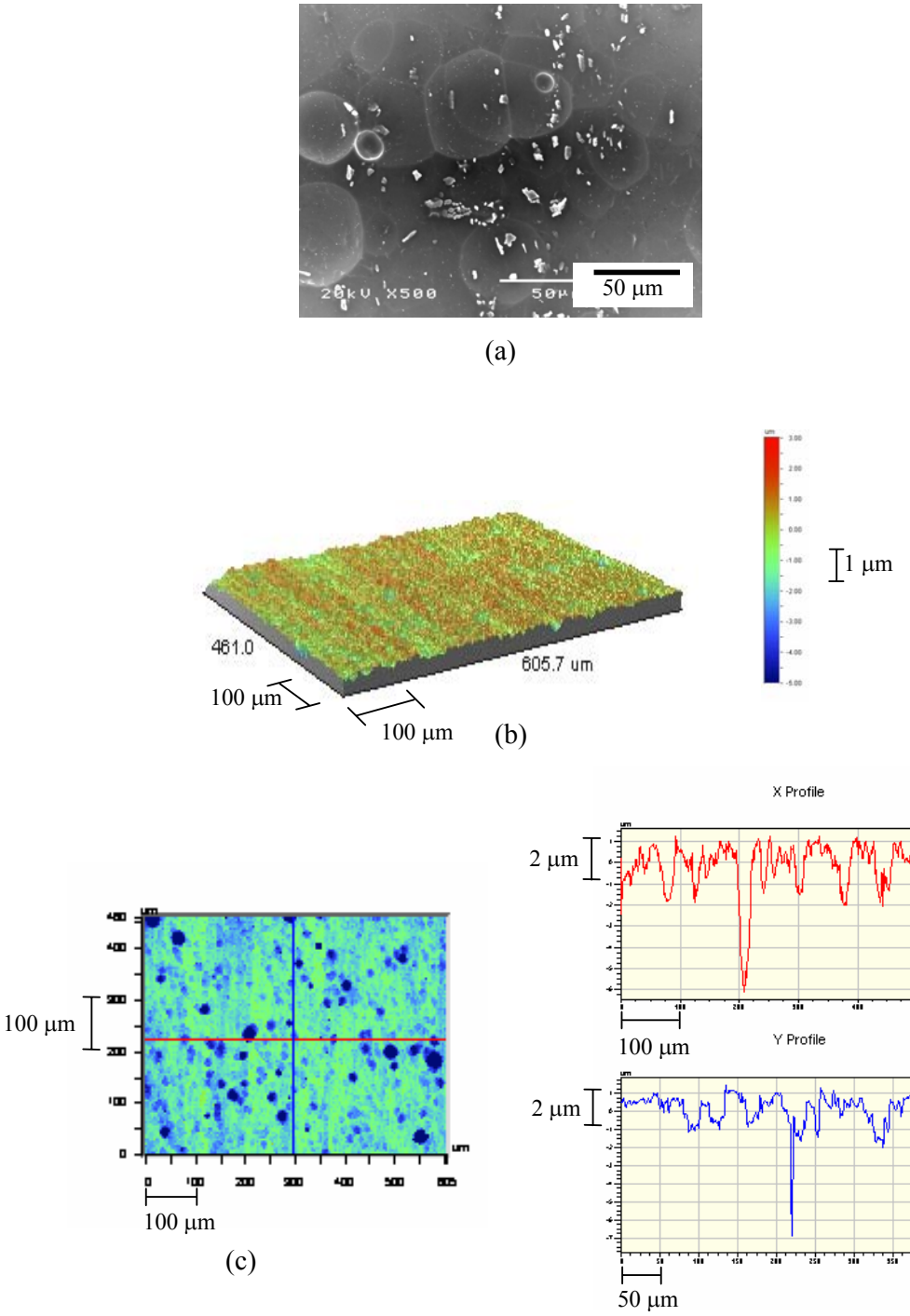

Figure 4.11 Surface morphology after grinding with 1200 SiC paper, degreasing in acetone, alkaline etching for 270 s and desmutting in concentrated HNO_3 for 30 s: (a) SEM image, (b) surface profile and (c) surface roughness topography.

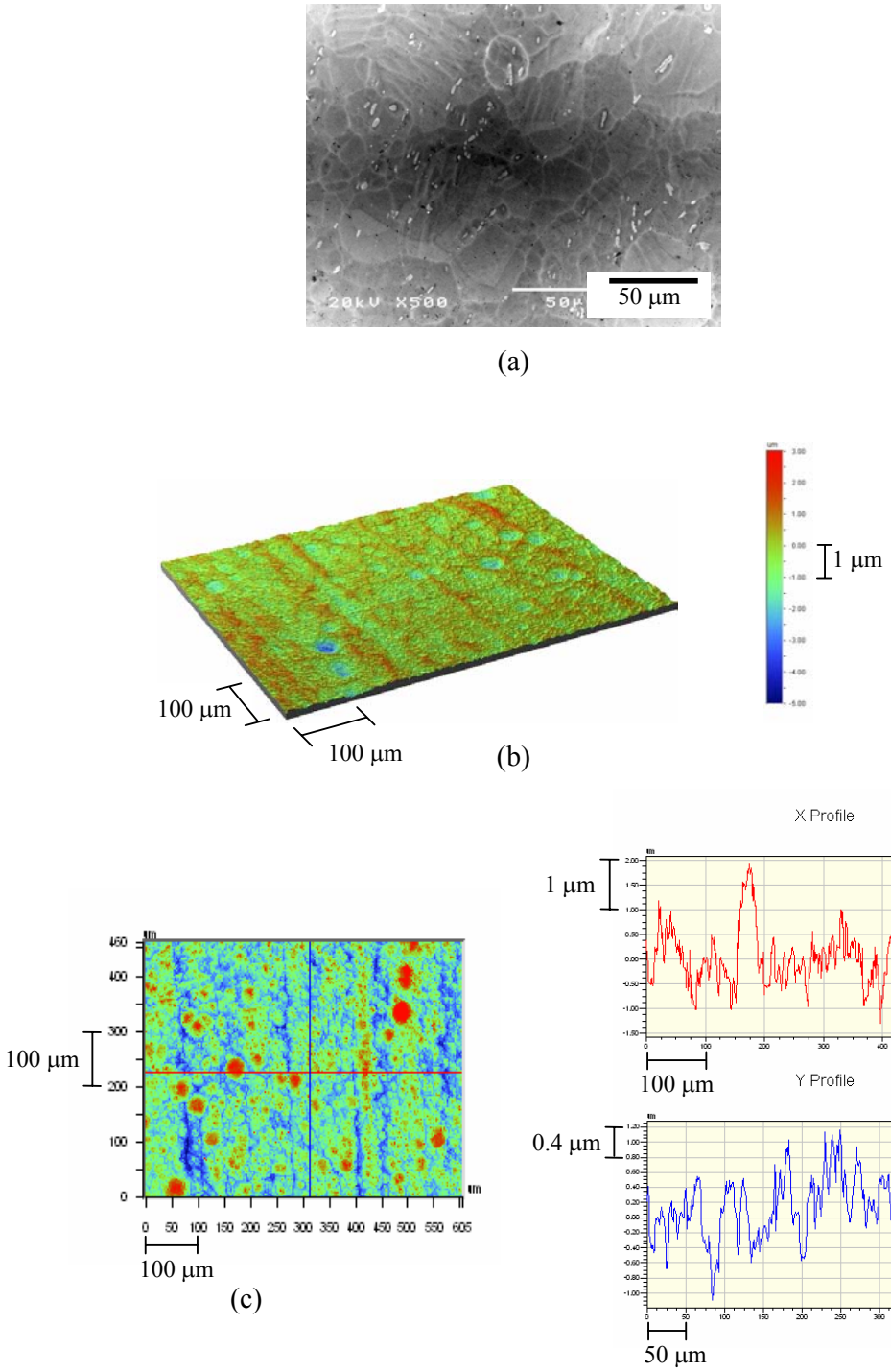

Figure 4.12 Surface morphology after GDOES sputtering for 200 s, degreasing in acetone and dipping in concentrated HNO_3: (a) SEM image, (b) surface profile and (c) surface roughness topography.

Table 4.1 Root-mean-square roughness of surfaces after the surface preparation shown in Figures 4.6(c)–4.12(c) (Rq (X): Root-mean-square roughness according to X-Profile and Rq (Y): Root-mean-square roughness according to Y-Profile as shown in Figures 4.6(c)–4.12(c))

Condition and surface roughness	Rq (X) (μm)	Rq (Y) (μm)	Rq (average) (μm)
1. As received + HNO_3	0.78	0.68	0.73
2. 1 μm + HNO_3	0.04	0.04	0.04
3. 1 μm, etched 45 s + HNO_3 30 s	0.15	0.18	0.16
4. 1200 SiC + HNO_3	0.45	0.55	0.50
5. 1200 SiC, etched 45 s + HNO_3 30 s	0.76	0.47	0.62
6. 1200 SiC, etched 270 s + HNO_3 30 s	1.15	1.19	1.17
7. GDOES + HNO_3	0.58	0.44	0.51

The "as received" surface has an average Rq of 0.60 μm. Figure 4.6 and Table 4.1 indicate that the 1 μm polished sample has the smoothest surface. Alkaline etching and desmutting in concentrated HNO_3 is found to increase the average Rq from 0.04 to 0.16 μm. Grinding with 1200 grit SiC paper gives a roughness greater than that of 1 μm polishing. Furthermore, the 1200 grit ground surface (Figure 4.9-(a.2)) shows more broken constituent intermetallic particles than the 1 μm polished surface (Figure 4.7-(a.2)). Etching the 1200 grit ground sample for 45 s and desmutting in HNO_3 does not significantly increase the surface roughness. However, increasing the etching time does give a significant increase in roughness, as shown in Figure 4.11. The average Rq increases from 0.62 to 1.17 μm for etching times of 45 s and 270 s. For the GDOES-sputtered sample, the average Rq is 0.51 μm, similar to the 1200 grit ground sample.

The SEM images of etched and desmutted samples (Figure 4.8, 4.10 and 4.11) show that intermetallic particles are exposed on the surface more than on unetched samples because the intermetallic particles dissolve more slowly than the matrix in sodium hydroxide. It also shows that there are holes developing on the etched surface, as shown in Figure 4.8, 4.10 and 4.11. This might be as a result of some intermetallic particles being removed from the surface during etching. The GDOES sputtered surface has intermetallic particles exposed on the surface (Figure 4.12).

The crater formed after etching the surface of the model alloy Al-1Mn-0.4Fe-0.3Si cold rolled sheet after solution heat-treatment and subsequent annealing with GDOES for 200 s was examined with white light interferometry. The image of the GDOES crater and depth profile of the etched area are shown in Figure 4.13(a) and (b). The crater has a diameter of ~4 mm, and a depth of ~3.6 μm, determined from the average of X and Y profiles as shown in Figure 4.13(b). The GDOES sputtered surface at this depth represents the bulk material [11].

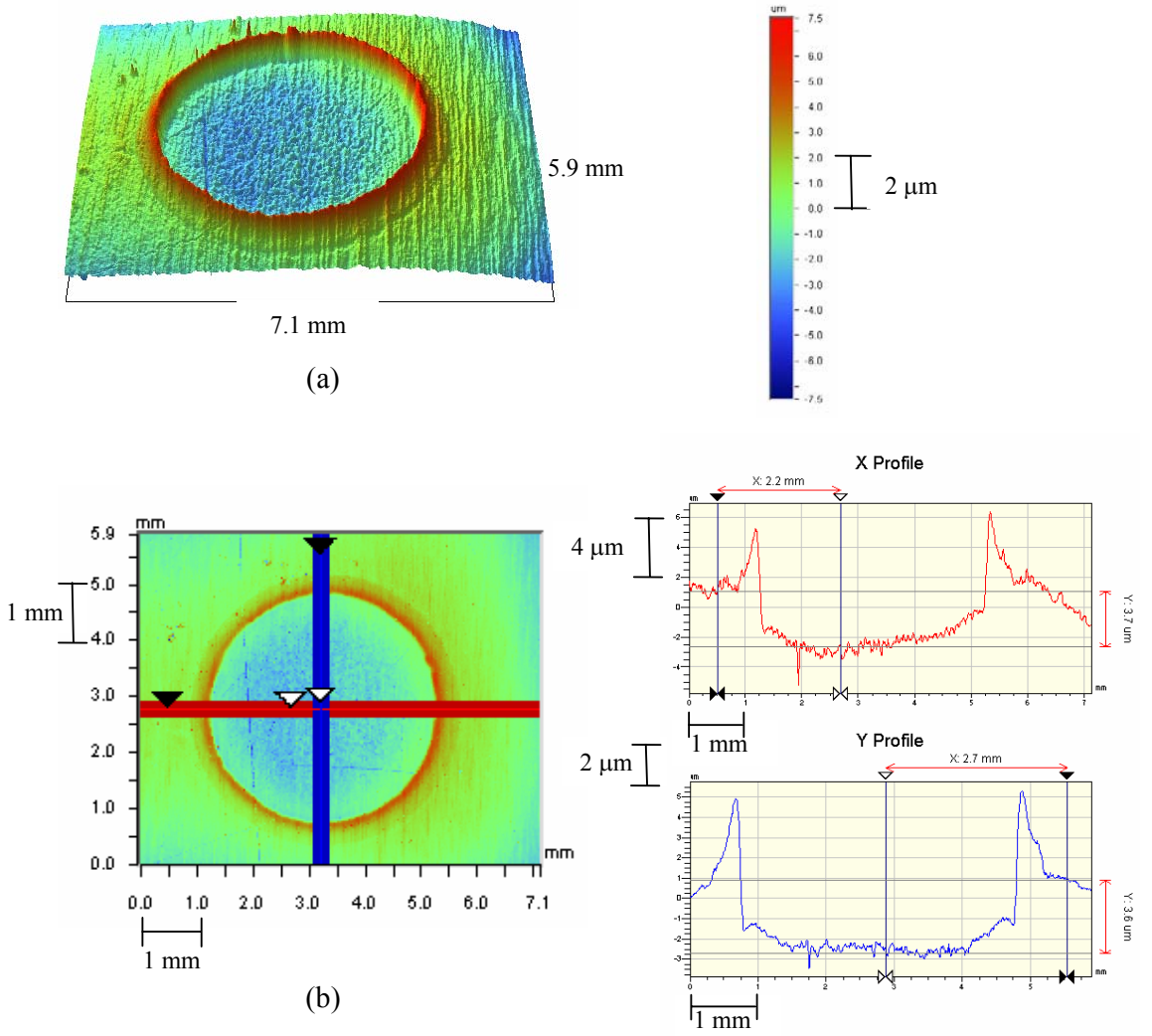

Figure 4.13 GDOES crater on Al-1Mn-0.4Fe-0.3Si cold rolled sheet after solution heat-treatment and subsequent annealing for 200 s etching (~3.6 µm depth) (a) view of crater with shoulder, (b) depth profiles.

4.2.2 Auger depth profiles

Auger depth profiles of surfaces prepared according to condition 2 (1 µm + HNO_3) and 8 (1 µm) for the Al-1Mn-0.4Fe-0.3Si alloy are shown in Figure 4.14. The intersection of oxygen and aluminium metal profiles represents the approximate position

of the oxide-metal interface [188]. Therefore, the oxide film on the 1 μm polished surface with the concentrated HNO_3 treatment is approximately 4 nm and without the concentrated HNO_3 treatment is approximately 6 nm. Thus, HNO_3 treatment leads to a thinner film.

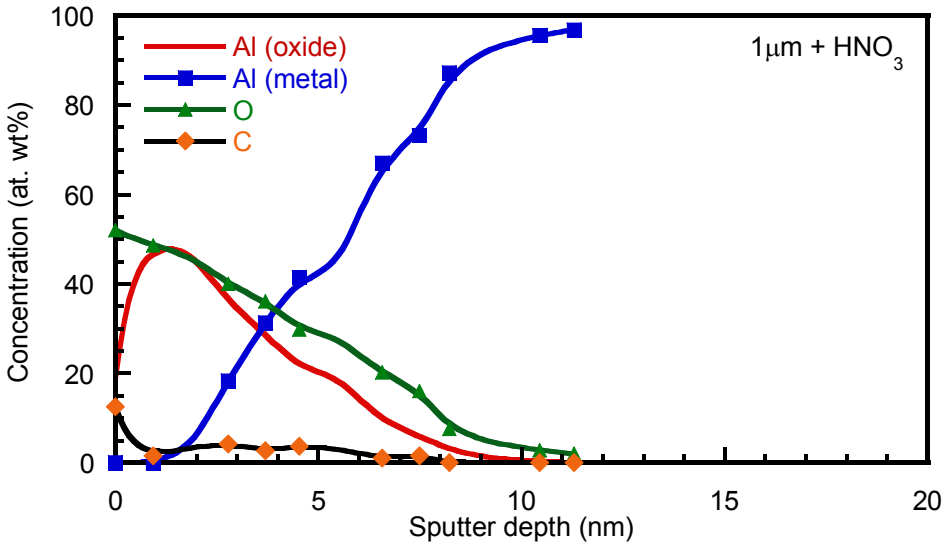

(a)

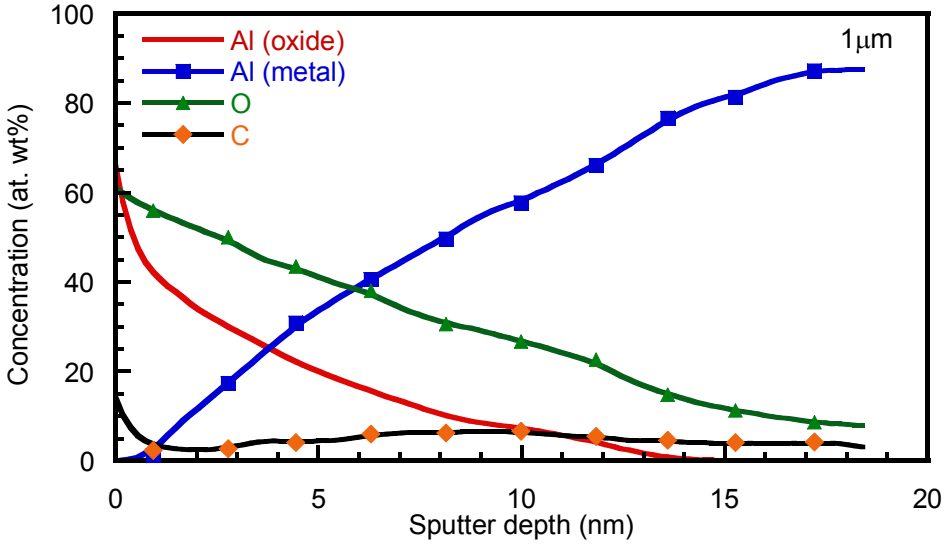

(b)

Figure 4.14 Auger depth profiles of samples of Al-1Mn-0.4Fe-0.3Si prepared by (a) 1 μm polishing, degreasing in acetone and dipping in concentrated HNO_3 and (b) 1 μm polishing and degreasing in acetone.

4.3 Corrosion measurements

4.3.1 In-situ observation of corrosion

The corrosion reactions occurring at the surface of a specimen in naturally aerated 1 M HCl after different surface preparations were recorded using a video camera attached to an optical microscope. Figure 4.15 shows still images taken from the video during an immersion test for 8 minutes. Small hydrogen bubbles are seen to evolve across the surface. The as received and 1200 grit ground samples show numerous sites of hydrogen evolution, in which each site is quite small. In comparison, the 1 μm polished sample and etched samples show fewer, larger bubbles. Etching the 1 μm polished sample for 45 s and desmutting in concentrated HNO_3 slightly decrease the number of sites for the hydrogen evolution reaction.

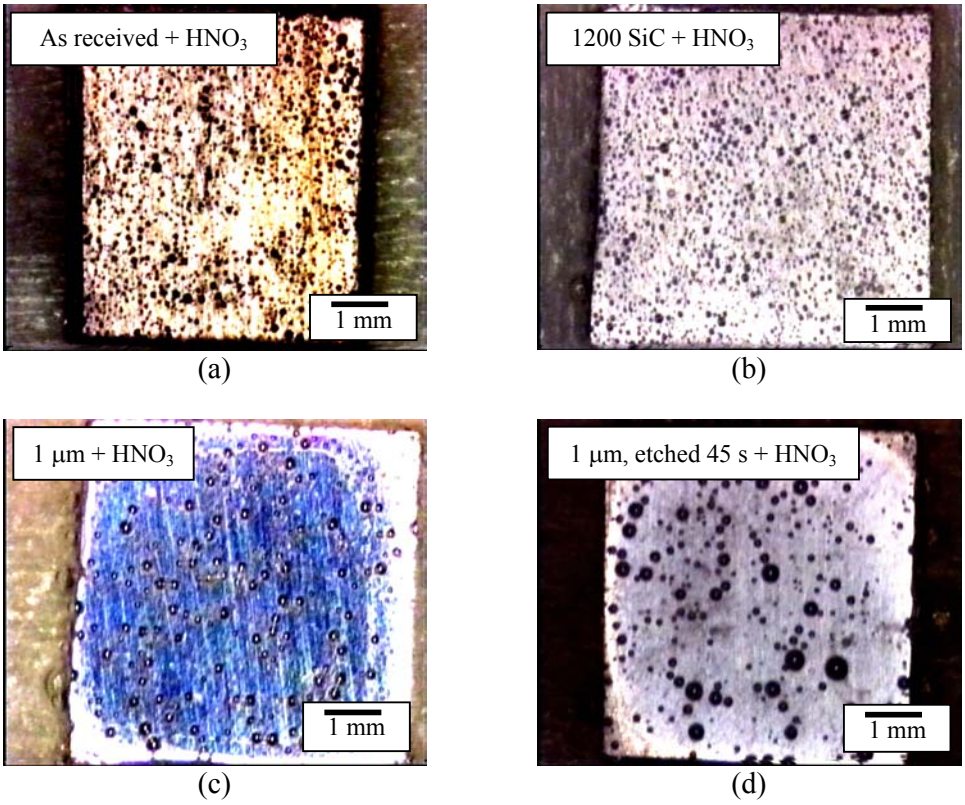

Figure 4.15 In-situ observation of corrosion of Al-1Mn-0.4Fe-0.3Si with different surface preparations in naturally aerated 1 M HCl: (a) as received, degreased in acetone and dipped in concentrated HNO_3, (b) ground with 1200 SiC paper, degreased in acetone and dipped in concentrated HNO_3, (c) polished with 1 μm diamond paste, degreased in acetone and dipped in concentrated HNO_3 and (d) polished with 1 μm diamond paste, degreased in acetone, alkaline etched for 45 s and desmutted in concentrated HNO_3.

4.3.2 Potentiodynamic cathodic and anodic polarisations

The cathodic and anodic reactivity for the Al-1Mn-0.4Fe-0.3Si alloy with different surface preparations was studied using potentiodynamic polarisation measurements in 0.85 M NaCl, pH 3, acidified with CH_3COOH.

Figures 4.16 and 4.17 show cathodic polarisation curves for different prepared surfaces in the naturally-aerated solution. The cathodic current density at a potential of -0.95 V(SCE) for different surface preparations was plotted from the cathodic polarisation curves (Figure 4.16 and 4.17), as shown in Figure 4.18. The data in Figure 4.18 were collected from repeated measurements which showed good reproducibility. From Figure 4.18, the GDOES sputtered surface exhibits the lowest cathodic reactivity while the 1 μm polished and alkaline etched and desmutted surface has the highest cathodic reactivity. For a given finish, dipping in HNO_3 increases the cathodic reactivity as shown in Figure 4.16 and 4.18. The 1 μm polished sample and the 1200 grit sample that were not dipped in HNO_3 are not significantly different in cathodic reactivity. Moreover, the 1200 grit and 1 μm polished samples that were dipped in HNO_3 do not show a significant difference in cathodic reactivity. Etching and desmutting in HNO_3 causes a further increase in the cathodic reactivity for the 1 μm polished surface and a slight increase in the cathodic reactivity for the 1200 SiC ground surface, as shown in Figure 4.17 and 4.18.

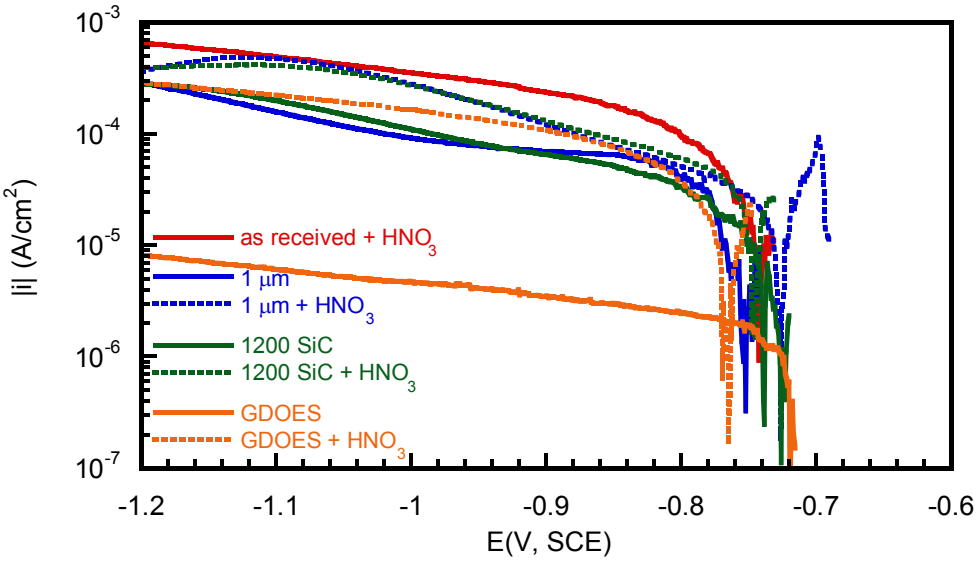

Figure 4.16 Cathodic polarisation curves of Al-1Mn-0.4Fe-0.3Si with different surface preparations in naturally aerated 0.85 M NaCl, pH 3 (CH_3COOH).

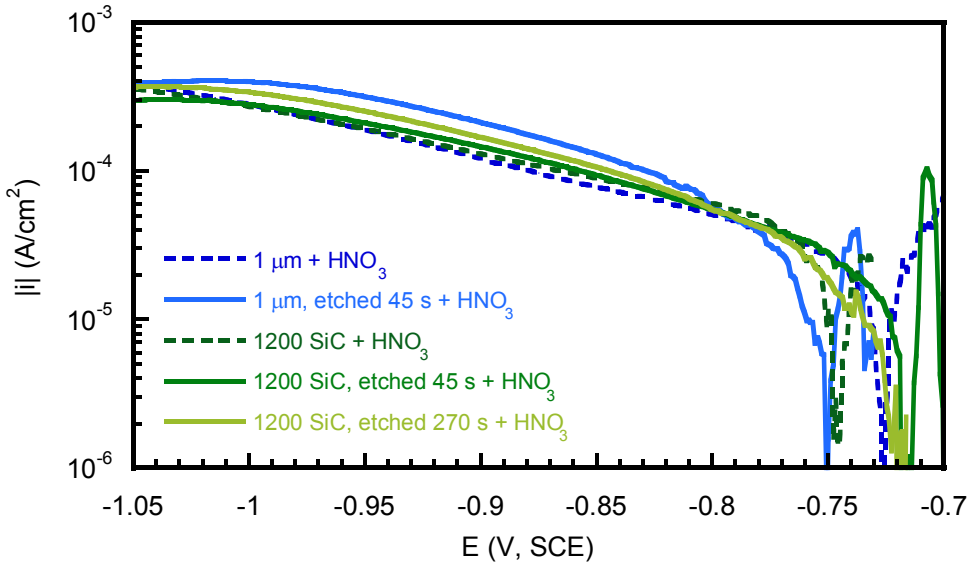

Figure 4.17 Cathodic polarisation curves of Al-1Mn-0.4Fe-0.3Si with and without alkaline etching in naturally aerated 0.85 M NaCl, pH 3 (CH_3COOH).

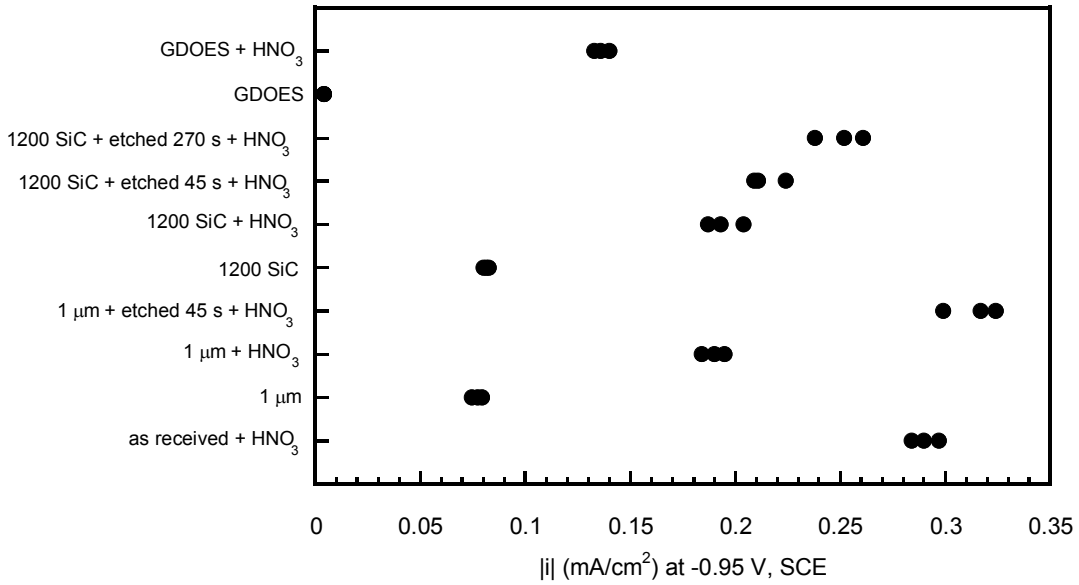

Figure 4.18 Cathodic current density (mA/cm^2) at a potential of -0.95 V, SCE for Al-1Mn-0.4Fe-0.3Si with different surface preparations in naturally aerated 0.85 M NaCl, pH 3 (CH_3COOH).

Figures 4.19 and 4.20 show anodic polarisation curves for different prepared surfaces in the de-aerated solution. The anodic potential at 100 $\mu A/cm^2$ for different surface preparations is shown in Figure 4.21. A lower anodic potential indicates a higher anodic reactivity. From Figures 4.19–4.21, the as received surface has the highest anodic reactivity and the 1 μm polished and etched and desmutted surface has the lowest anodic reactivity. For all of the surfaces, dipping in HNO_3 slightly decreases the anodic reactivity, and etching followed by desmutting leads to a further decrease in anodic reactivity.

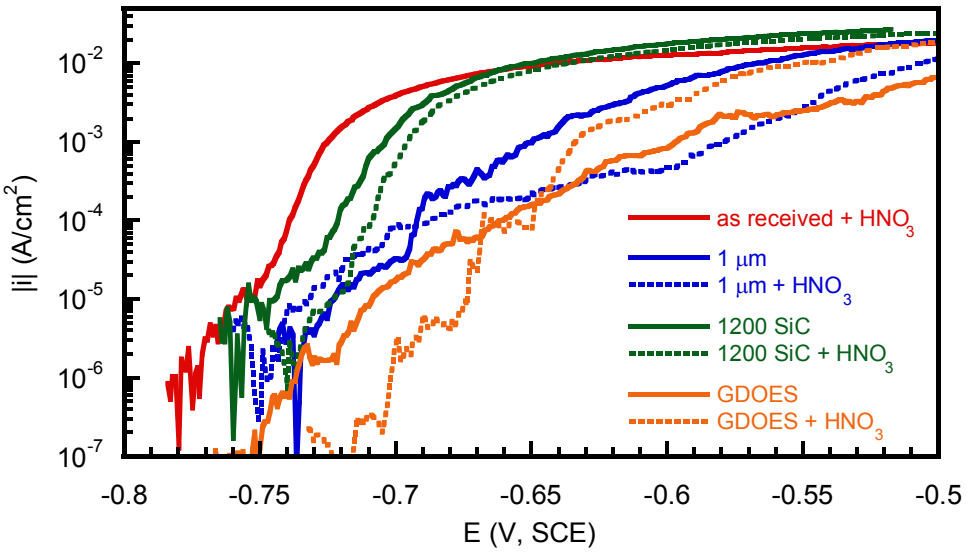

Figure 4.19 Anodic polarisation curves of Al-1Mn-0.4Fe-0.3Si with different surface preparations in de-aerated 0.85 M NaCl, pH 3 (CH_3COOH).

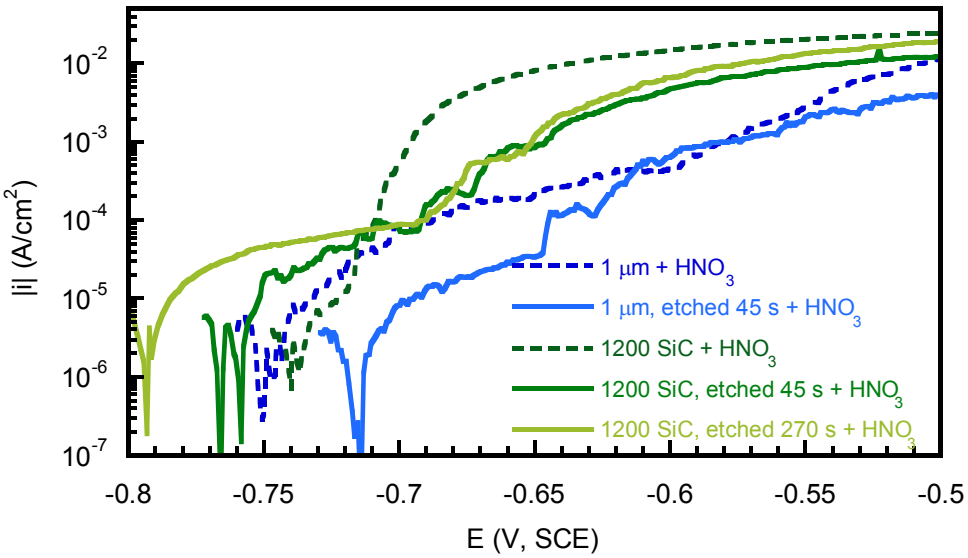

Figure 4.20 Anodic polarisation curves of Al-1Mn-0.4Fe-0.3Si with and without alkaline etching in de-aerated 0.85 M NaCl, pH 3 (CH_3COOH).

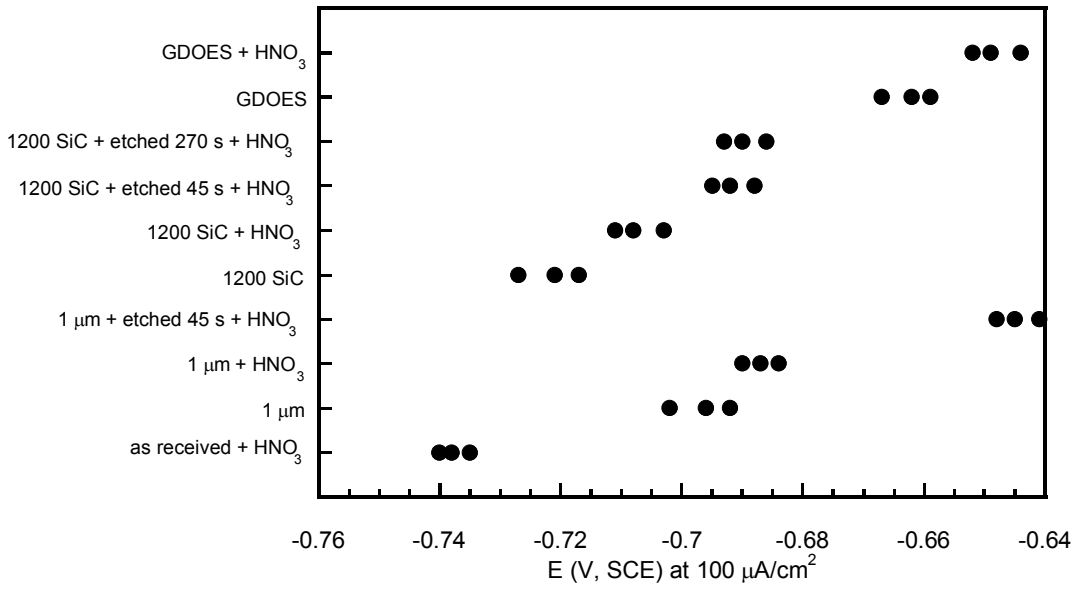

Figure 4.21 Anodic potential (V, SCE) at a current density of 100 μA/cm^2 for Al-1Mn-0.4Fe-0.3Si with different surface preparations in de-aerated 0.85 M NaCl, pH 3 (CH_3COOH).

Figure 4.22 shows the relationship between surface roughness and anodic reactivity. It shows that the increased surface roughness from mechanical polishing (1 μm polishing and 1200 SiC grinding) results in increasing anodic reactivity. However, it is also shown that increasing the surface roughness by etching or GDOES sputtering results in decreasing anodic reactivity. This implies that both surface roughness and chemistry of the surface affect the electrochemical behaviour. For the same chemical treatment, the anodic reactivity is slightly higher for a rougher surface. However, the chemical treatments have a bigger effect than the surface roughness on the anodic reactivity.

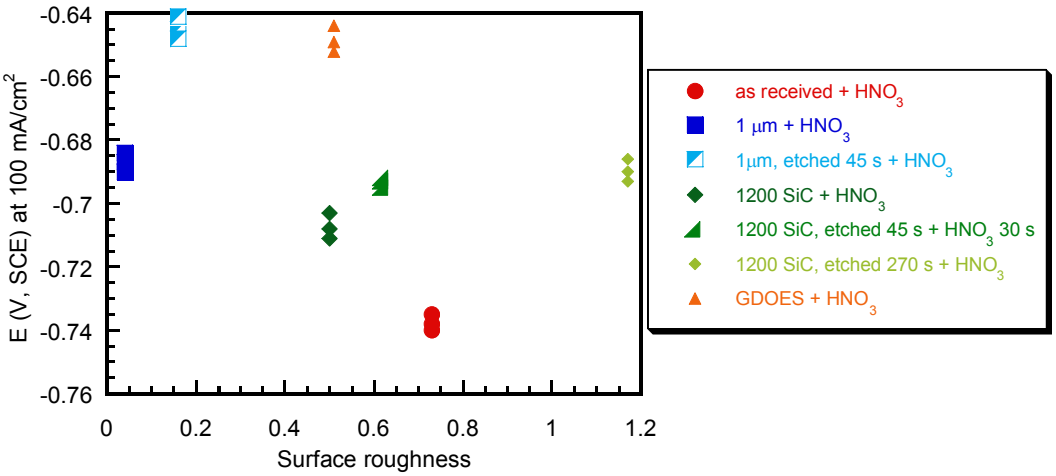

Figure 4.22 Effect of surface roughness on anodic potential (V, SCE) at a current density of 100 μA/cm^2 in de-aerated 0.85 M NaCl, pH 3 (CH_3COOH).

4.3.4 Corrosion surface morphology

Figure 4.23 shows the typical surface morphology of corroded surfaces after potentiodynamic anodic polarisation to –0.5 V(SCE) in de-aerated 0.85 M NaCl, pH 3, acidified with CH_3COOH. Generally, the images show localised corrosion sites and intermetallic particles on the surface. The as received sample has a high number of fine localised corrosion sites as shown in Figure 4.23(j). The GDOES, 1μm polished with and without dipping in HNO_3, and 1 μm polished, etched and desmutted samples have fewer, larger localised corrosion sites as shown in Figure 4.23(a)–(c) and (g)–(h). The 1200 grit SiC ground samples with and without dipping in HNO_3 and the etched and desmutted samples lie in between as shown in Figure 4.23(d)–(f) and (i).

In this study, the localised corrosion is pitting corrosion, which occurs where intermetallic particles are found, as shown in Figure 4.24(a)–(j). The distribution of pits is random on the surface of as received, 1 μm polished and 1200 grit SiC ground samples with and without dipping in HNO_3. On the other hand, for the GDOES with and without dipping in HNO_3, and etched and desmutted samples, there are few larger pits on some areas on the surface.

The 1200 grit SiC ground samples with and without dipping in HNO_3 samples appear to have a higher density of pits than the 1 μm polished samples. In the case of etched and desmutted samples, many particles can be observed on surface as shown in Figure 4.8(a), 4.10(a) and 4.11(a), but then few of these are active as initiation sites, as they do not show an increased density of pits. The 1 μm polished samples with and without dipping in HNO_3, as shown in Figure 4.23(a) and (b), are found to have more pit initiation sites than etched and desmutted surfaces, as shown in Figure 4.23(c). Similarly, the 1200 grit SiC ground surfaces with and without dipping in HNO_3 samples, as shown in Figure 4.23(d) and (e) appear to have more pit initiation sites than etched and desmutted surfaces, as shown in Figure 4.23(f) and (i). The micrographs of corroded etched and desmutted surface show larger pits. This is probably because the current flow on the unetched surface was limited by iR drop. All anodic polarisation curves were stopped at a fixed potential of –0.5 V(SCE).

All of the pits show similar crystallographic attack. They show undissolved crystallographic planes and inside them are found undissolved intermetallic particles (Figure 4.24 and 4.26).

After cathodic polarisation to –1.2 V(SCE) in naturally aerated 0.85 M NaCl, pH 3, acidified with CH_3COOH, the images do not show any corrosion sites (Figure 4.25(a)–(j).

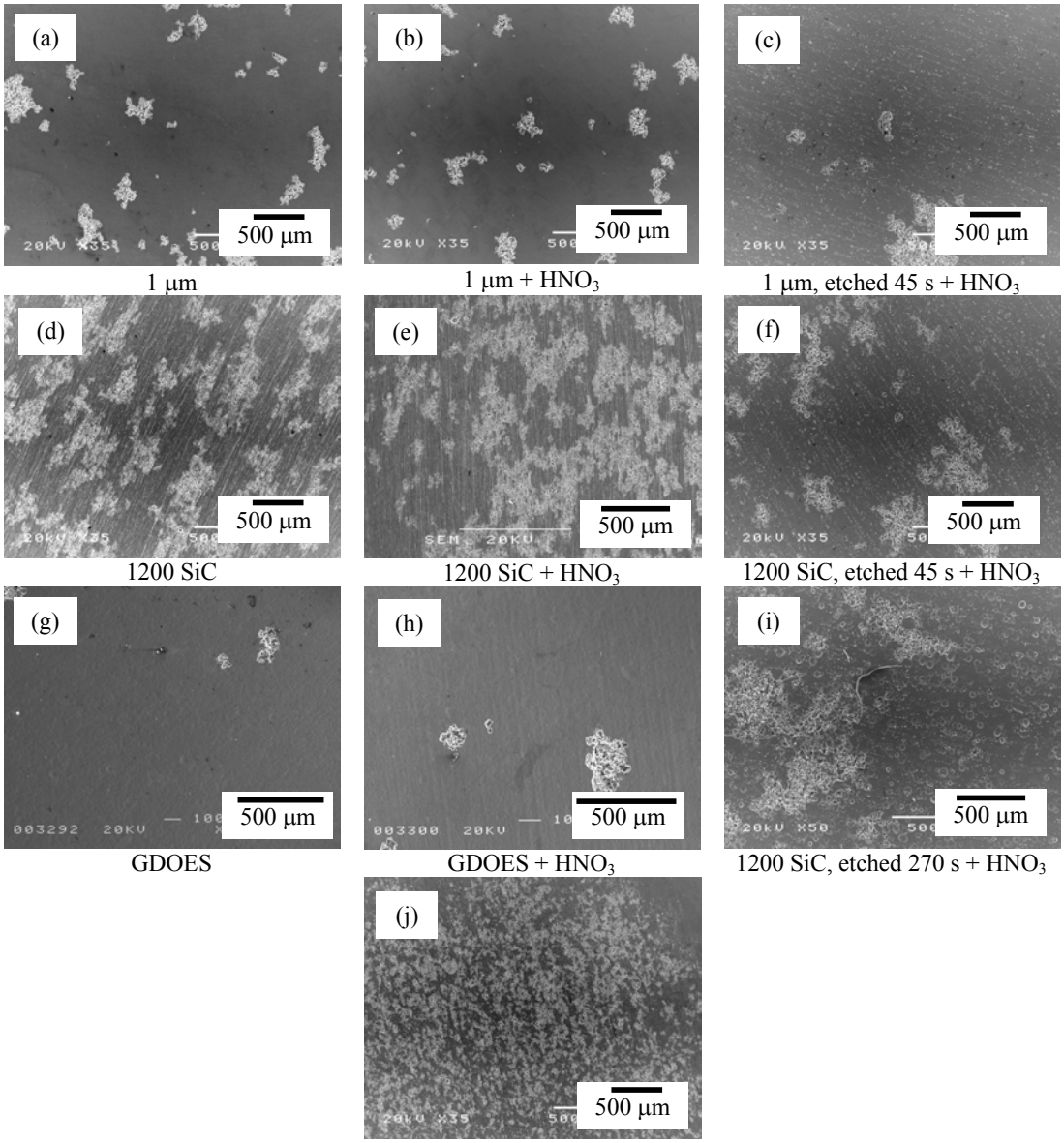

Figure 4.23 Surface morphology at low magnification of the corroded surface after anodic polarisation in de-aerated 0.85 M NaCl pH 3 (CH_3COOH) to –0.5 V(SCE) for (a) 1 µm diamond paste polished sample degreased in acetone, (b) 1 µm diamond paste polished sample, degreased in acetone and dipped in concentrated HNO_3, (c) 1 µm diamond paste polished sample, degreased in acetone, alkaline etched for 45 s and desmutted in concentrated HNO_3 for 30 s, (d) 1200 SiC ground sample and degreased in acetone, (e) 1200 SiC ground sample, degreased in acetone and dipped in concentrated HNO_3, (f) 1200 SiC ground sample, degreased in acetone, alkaline etched for 45 s and desmutted in concentrated HNO_3, (g) GDOES sputtered sample and degreased in acetone, (h) GDOES sputtered sample, degreased in acetone and dipped in concentrated HNO_3, (i) 1200 SiC ground sample, degreased in acetone, alkaline etched for 270 s, and desmutted in concentrated HNO_3 for 30 s and (j) as received sample, degreased in acetone and dipped in concentrated HNO_3.

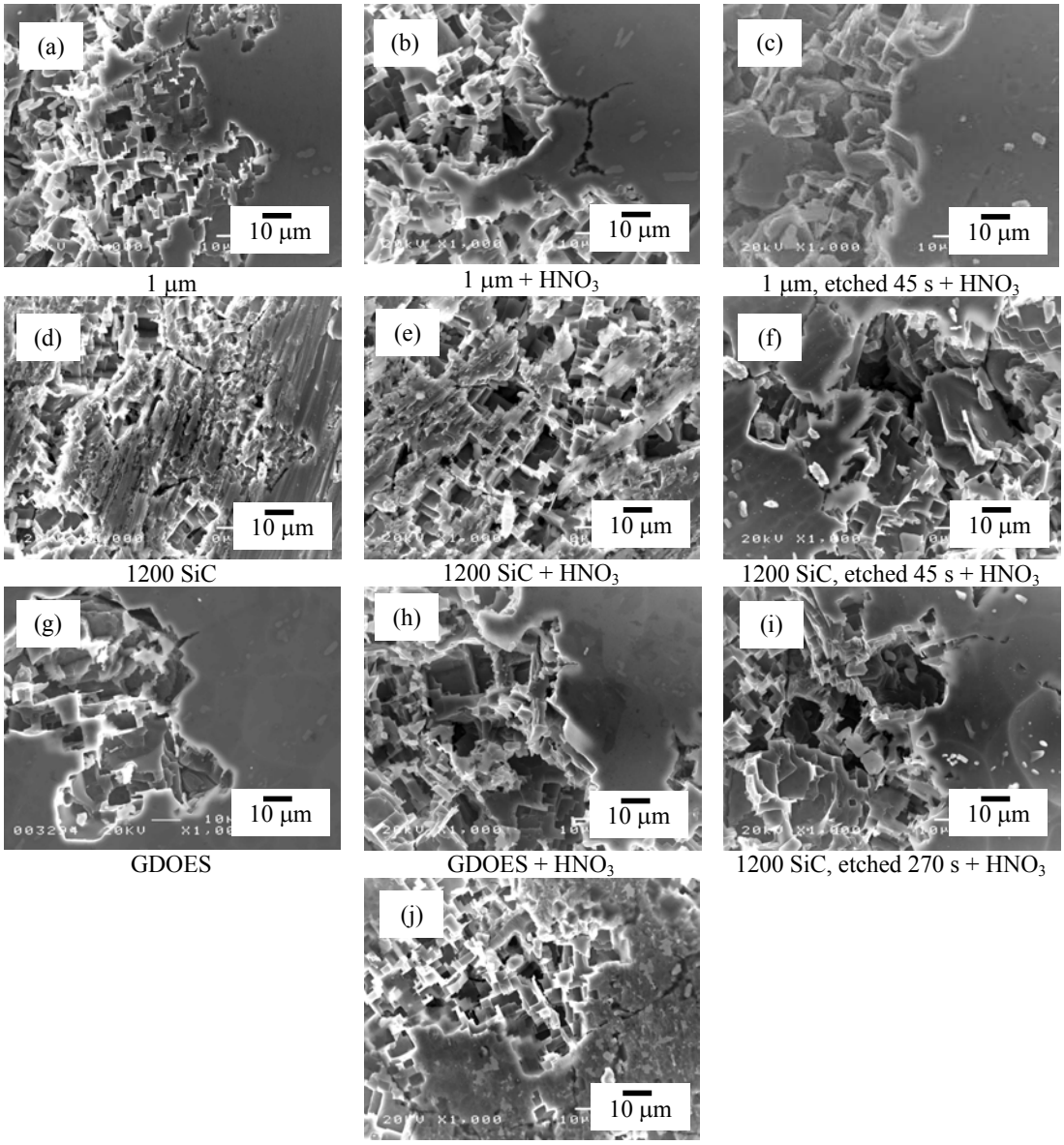

Figure 4.24 Surface morphology at high magnification of the corroded surface after anodic polarisation in de-aerated 0.85 M NaCl pH 3 (CH_3COOH) to –0.5 V(SCE) for (a) 1 μm diamond paste polished sample degreased in acetone, (b) 1 μm diamond paste polished sample, degreased in acetone and dipped in concentrated HNO_3, (c) 1 μm diamond paste polished sample, degreased in acetone, alkaline etched for 45 s and desmutted in concentrated HNO_3 for 30 s, (d) 1200 SiC ground sample and degreased in acetone, (e) 1200 SiC ground sample, degreased in acetone and dipped in concentrated HNO_3, (f) 1200 SiC ground sample, degreased in acetone, alkaline etched for 45 s and desmutted in concentrated HNO_3, (g) GDOES sputtered sample and degreased in acetone, (h) GDOES sputtered sample, degreased in acetone and dipped in concentrated HNO_3, (i) 1200 SiC ground sample, degreased in acetone, alkaline etched for 270 s, and desmutted in concentrated HNO_3 for 30 s and (j) as received sample, degreased in acetone and dipped in concentrated HNO_3.

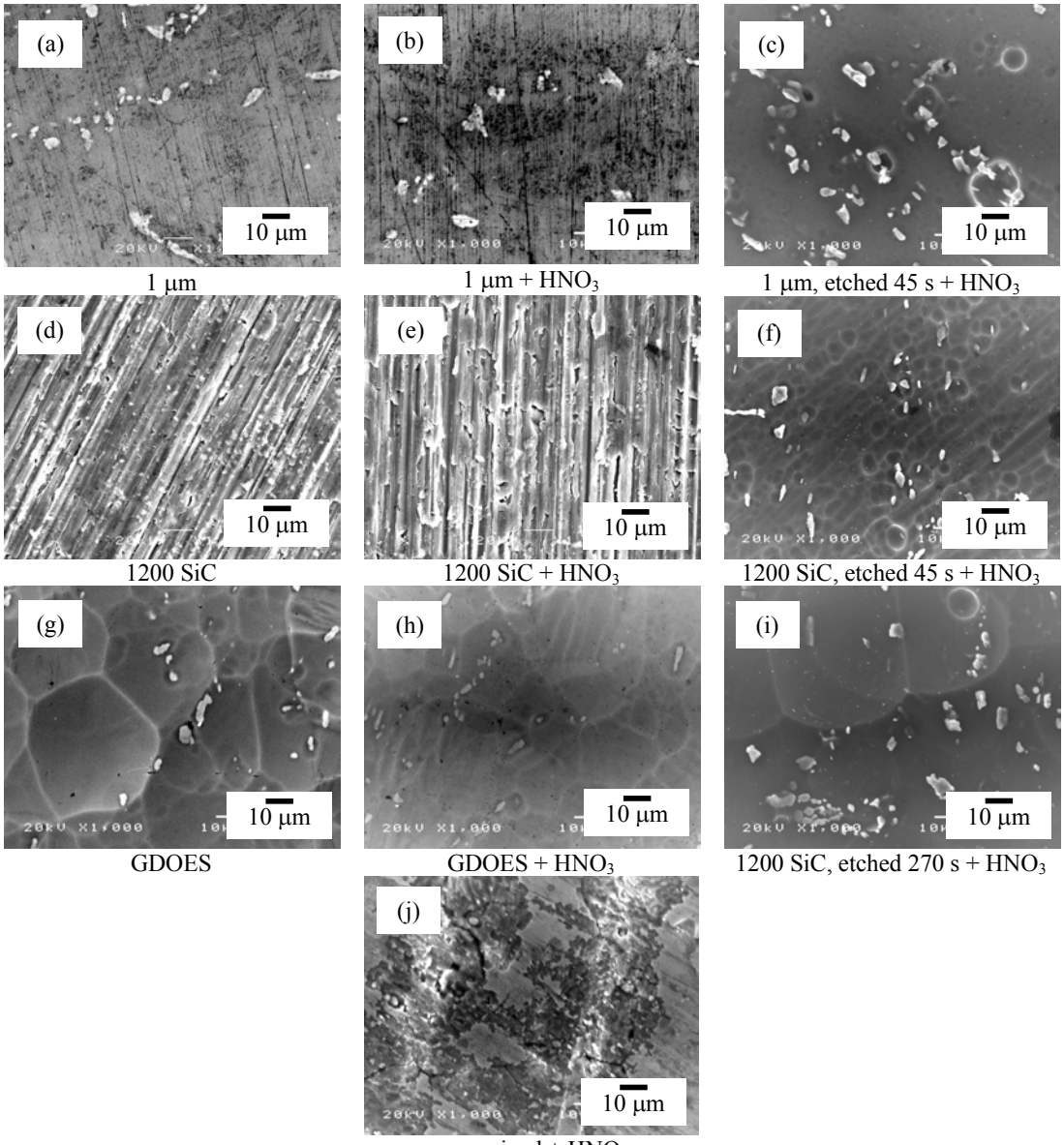

Figure 4.25 Surface morphology of the surface after cathodic polarisation in naturally aerated 0.85 M NaCl pH 3 (CH_3COOH) to −1.2 V(SCE) for (a) 1 μm diamond paste polished sample degreased in acetone, (b) 1 μm diamond paste polished sample, degreased in acetone and dipped in concentrated HNO_3, (c) 1 μm diamond paste polished sample, degreased in acetone, alkaline etched for 45 s and desmutted in concentrated HNO_3 for 30 s, (d) 1200 SiC ground sample and degreased in acetone, (e) 1200 SiC ground sample, degreased in acetone and dipped in concentrated HNO_3, (f) 1200 SiC ground sample, degreased in acetone, alkaline etched for 45 s and desmutted in concentrated HNO_3, (g) GDOES sputtered sample and degreased in acetone, (h) GDOES sputtered sample, degreased in acetone and dipped in concentrated HNO_3, (i) 1200 SiC ground sample, degreased in acetone, alkaline etched for 270 s, and desmutted in concentrated HNO_3 for 30 s and (j) as received sample, degreased in acetone and dipped in concentrated HNO_3.

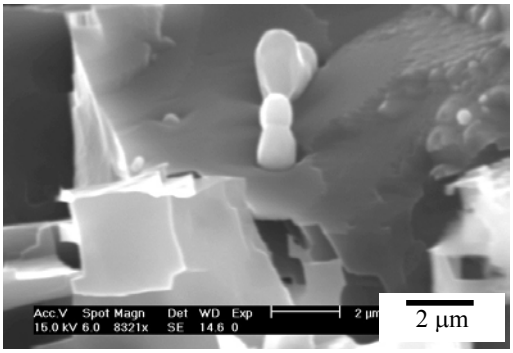

Figure 4.26 SEM image of interior of pit with intermetallic particles of corroded surface after anodic polarisation in de-aerated 0.85 M NaCl pH 3 (CH_3COOH) to −0.5 V(SCE) for 1 µm diamond paste polished sample, degreasing in acetone and dipping in concentrated HNO_3.

4.4 Discussion

The corrosion behaviour of a metallic surface greatly depends on the metallurgical microstructure and surface morphology [189]. Microstructure plays a role through the electrochemical behaviour of constituent intermetallic particles, while the morphology of the surface, particularly roughness, provides sites of enhanced reactivity as well as occluded sites for corrosion [13, 153, 190, 191]. The rough surface is much easier to pit compared with the smooth surface with similar metallurgical microstructure because of the ability to create the local pit chemistry necessary for pit propagation [190]. Dissolution of aluminium into an occluded cavity on the surface produces Al^{3+} cations which then hydrolyse, generating a more aggressive low pH evironment.

Surface preparation of aluminium alloys used prior to a corrosion test has a significant effect on pitting corrosion [18]. In the present investigation, two grinding

methods were compared. The 1 μm polished surface has a lower anodic reactivity than the 1200 ground surface (Figure 4.19 and 4.21). This is probably as a result of the greater roughness for the 1200 ground surface. Therefore, it is much easier for an aggressive solution chemistry to develop occluded sites on a rough surface. This factor contributes to the anodic reactivity via pitting. However, the slightly increased cathodic reactivity for 1200 ground surface might be attributed to the breaking up of the intermetallic particles (Figure 4.9(a.2)) improving access of dissolved oxygen and increasing the cathodic reaction.

Alkaline etching is frequently employed for cleaning the surface of aluminium alloys prior to corrosion testing and various treatment processes [9, 19, 20, 39, 182]. Appropriate alkaline etching can remove the deformed layer on the surface of hot rolled or cold rolled sheets of aluminium alloys, resulting in increasing corrosion resistance [18, 20, 127]. Furthermore, the use of alkaline etching, together with mechanical or electrochemical polishing, can control filiform corrosion (FFC) to a similar extent to chromate conversion coating [192]. However, alkaline etching in some cases has an adverse effect on corrosion susceptibility because alkaline etching dissolves a thin layer of the matrix which covers the cathodic intermetallic particles [39, 182].

Koroleva et al. [39, 184] found that during alkaline etching followed by desmutting in HNO_3 of high purity aluminium, the air-formed film was removed and then replaced with a thin, dense and homogeneous oxide film on the surface. The desmutting only removes corrosion products [185]. After alkaline etching of an Al-Mn alloy, the surface of a fine scallop textures was generated on the surface, exposing more

intermetallic particles as dissolution of the matrix is higher than that of the α-Al(MnFe)Si intermetallic particles [18, 39, 127, 182, 184].

In this study, the effect of alkaline etching followed by desmutting was studied for bulk rolled sheet. Alkaline etching and desmutting in concentrated HNO_3 of the 1 μm polished and 1200 ground surfaces resulted in decreasing anodic reactivity. This may be because etching changes the chemical properties of the surface, which decreases the ease of pit initiation. SEM images (Figure 4.23(b)–(c), (e)–(f) and (i)) indicate that the pitting sites on the corroded surface after etching and desmutting are less numerous than the unetched surfaces.

However, alkaline etching and desmutting in concentrated HNO_3 has an adverse effect on the cathodic reactivity of the 1 μm polished surface by exposing more intermetallic particles on the surface, as indicated by the current density of cathodic polarisation (Figure 4.17 and 4.18). Furthermore, alkaline etching and desmutting in concentrated HNO_3 has a similar effect on the cathodic reactivity of the 1200 ground surface.

The etched and desmutted surface roughness is more than that of the unetched surface roughness. The SEM images (Figure 4.7(a)–4.11 (a)) show that there are more intermetallic particles exposed on the etched and desmutted surface than the unetched surface. This implies that the intermetallic particles dissolve in sodium hydroxide more slowly than the matrix. These SEM images also show the development of holes on the

etched and desmutted surface. This might be as a result of loss of some intermetallic particles from the surface during etching.

Nitric acid treatment, usually called desmutting, is found to have some influence on the electrochemical behaviour of aluminium surface [23]. Desmutting with nitric acid is used to remove a layer left by alkaline etching. [175] Zhou et al. [23] investigated alkaline etched surfaces with and without desmutting on AA5005 H14 aluminium alloy sheet. A micrograph of an microtomed cross section of the alloy after alkaline etching in 20 wt% NaOH solution at 60°C showed that the active deformed layer (Figure 2.12(a) in Section 2.2.4.2) was removed completely and replaced with a layer of etched products, of thickness 20-30 nm (Figure 2.12(c) in Section 2.2.4.2). This etched-product layer was replaced by a relatively uniform air-formed film, less than 10 nm thickness, after desmutted in concentrated HNO_3 solution (Figure 2.12(d) in Section 2.2.4.2). The investigation on 1 μm polished, 1200 grit ground, and GDOES sputtered surfaces treated with HNO_3 on anodic polarisation showed decreasing anodic reactivity. This may be due to nitric acid treatment dissolving the hydrated oxide film layer and forming a uniform oxide film on the surface that allows less anodic reactivity.

Nitric acid treatment leads to higher cathodic reactivity on the 1 μm polished, 1200 grit ground, and GDOES sputtered surfaces. The Auger electron spectroscopy measurements (Figure 4.13) show that the film on the nitric acid-cleaned surface has a thinner oxide film. This may also lead to a decrease in film thickness on intermetallic particles, facilitating oxygen reduction.

There is a higher density of pit initiation sites on the as-received surface compared with GDOES sputtered surfaces with and without HNO_3 treatment (Figure 4.23). This may be associated with the presence of an active deformed layer on the surface. Ambat et al. [11] investigated the very thin deformed layer in the same material, cold rolled sheet of Al-1Mn-0.4Fe-0.3Si model alloy. It was found that the both anodic and cathodic reactivity of the deformed layer, approximately 1 μm, were significantly higher than that of the bulk. This deformed layer results form shear deformation during rolling and subsequent annealing lead to enhanced precipitation of fine intermetallic particles in the surface layers. [10, 51] These layers have high electrochemical reactivity. [9, 11, 13, 14, 45, 149, 150] GDOES sputtered surfaces represent the bulk materials in this investigation.

All pits show intermetallic particles embedded in their interior. It is likely that these intermetallic particles act as pit initiation sites. Many research groups [16, 19, 79-81, 127] have also found that iron-rich intermetallic particles are nucleation sites of pits.

4.5 Summary

The intermetallic particles that are found on the solution heat-treated and subsequent annealed model alloy Al-1Mn-0.4Fe-0.3Si cold rolled sheet are composed of Al, Fe, Mn, and Si, and are expected to be α-$Al_{12}(Fe,Mn)_3Si$.

Different surface preparations of this alloy show different electrochemical behaviour as follows:

- Pitting is always associated with intermetallic particles.
- Nitric acid treatment decreases the anodic reactivity but increases the cathodic reactivity.
- Alkaline etching and desmutting in concentrated HNO_3 decreases the anodic reactivity but increases the cathodic reactivity.
- Increasing the surface roughness from mechanical polishing (1 μm polishing and 1200 SiC grinding) results in increasing anodic reactivity. However, the roughness has little effect on cathodic reactivity. This will result in more pitting.
- The GDOES sputtered surface which has a depth of ~3.6 μm from the surface has lower anodic and cathodic reactivity than the as-received surface.

Chapter 5 Electrochemical Behaviour of Active Surface Layers in Commercial Rolled AA3005 Sheet

The electrochemical reactivity of the surface layers of commercial rolled AA3005 sheet was investigated by profiling through the surface with GDOES. The microstructure and electrochemical reactivity was examined at different depths in order to compare the behaviour of the surface layers with that of the bulk alloy.

5.1 Topography of the GDOES etched surface

The crater formed after etching the surface of AA3005 sheet with GDOES for 150 s was examined with white light interferometry. The image of the GDOES crater, depth profile, and a high magnification image of the etched area are shown in Figure 5.1. The crater has a diameter of ~4 mm, and a depth of ~2 μm, determined from the X and Y profiles as shown in Figure 5.1(b). The sputtering process leaves a shoulder of ~4 μm in height and 0.8 mm width around the edge of the sputtered area. The surface is slightly rough after the etching, with a RMS roughness value of about 1.5 μm after 150 s etching.

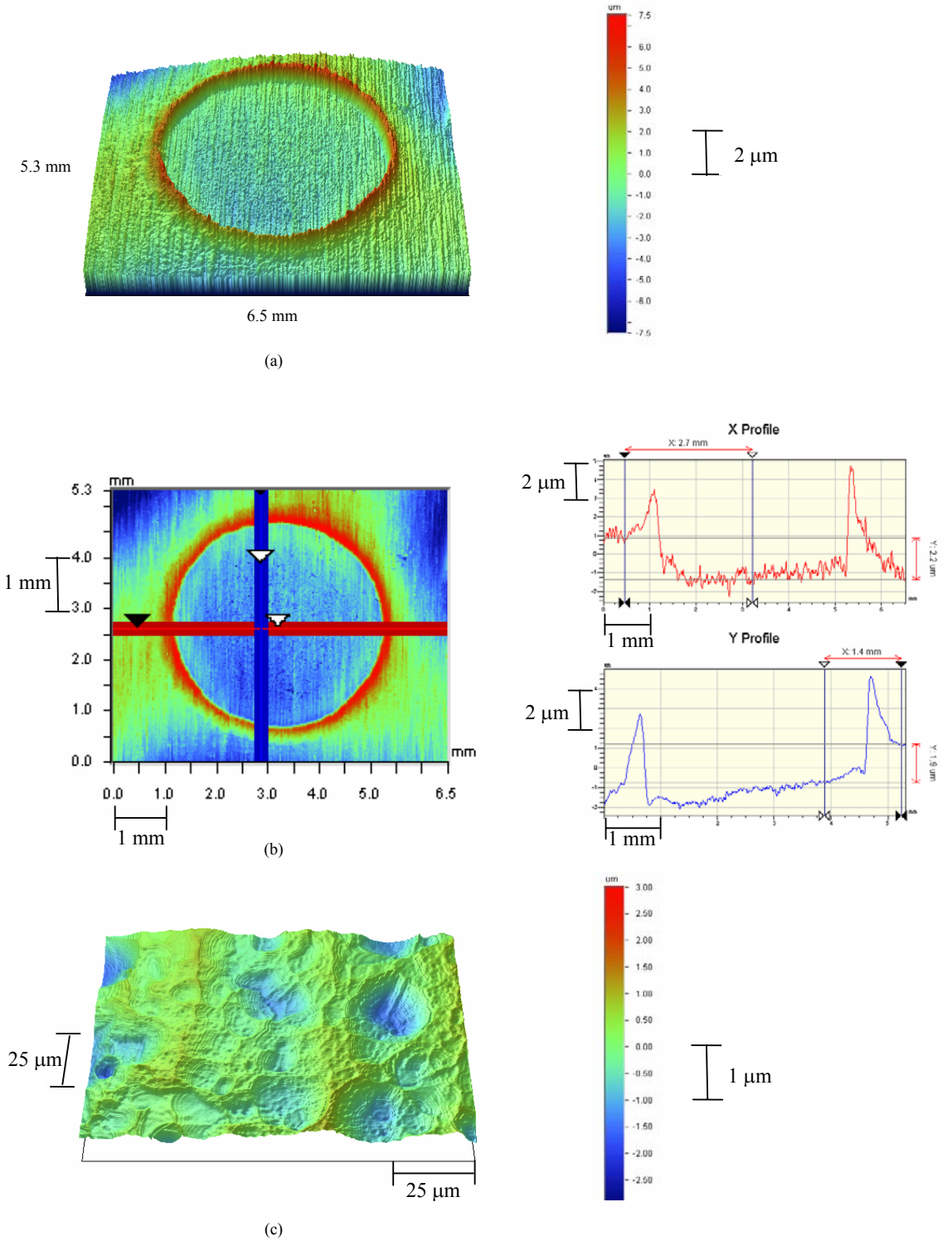

Figure 5.1 GDOES crater on AA3005 after 150 s etching (2 µm depth) (a) view of crater with shoulder, (b) depth profiles and (c) magnified view of the bottom of the crater showing surface topography.

5.2 Microstructure morphology

The microstructure of the bulk alloy after GDOES etching is shown in Figure 5.2(a), obtained using backscattered electron (BE) imaging. There are a number of large intermetallic particles in the range 1-10 μm. EDX analysis shows that there are two types: one contains Fe, Mn and Si in addition to Al, and the other contains Fe and Mn in addition to Al, as shown in Figure 5.2(b) and (c).

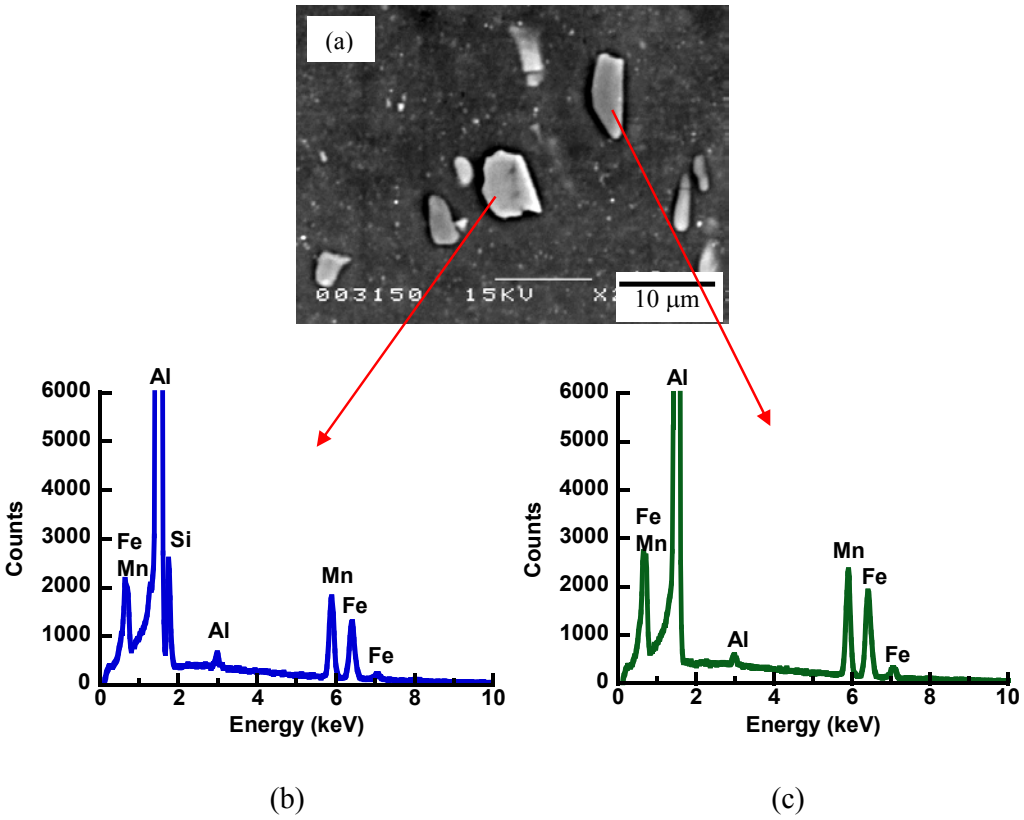

(b) (c)

Figure 5.2 SEM BE image of 1 μm polished surface (equivalent to bulk) of AA3005 (a) and EDX spectrum of the α-Al(MnFe)Si phase, (b) and the AlMnFe phase, (c).

Figure 5.3 shows the concentration of Mn vs. Fe in both phases. These phases are frequently identified as α-$Al_{12}(MnFe)_3Si$ and $Al_6(MnFe)$ [4, 36]. Composition analysis of 200 particles larger than ~1 μm using EDX found approximately 90% of the intermetallic particles were $Al_6(MnFe)$ and the rest were α-$Al_{12}(MnFe)_3Si$. The iron to manganese ratio in $Al_6(MnFe)$ was 0.6 ± 0.2 and in α-$Al_{12}(MnFe)_3Si$ was 0.5 ± 0.2. Previous work done by Afseth et al. [14] on the same material showed that approximately 60% of the intermetallic particles were $Al_6(MnFe)$ and the remainder were α-$Al_{12}(MnFe)_3Si$. They also analysed intermetallic particles larger than ~1 μm, and found an iron to manganese ratio of 0.8-0.9 for both phases.

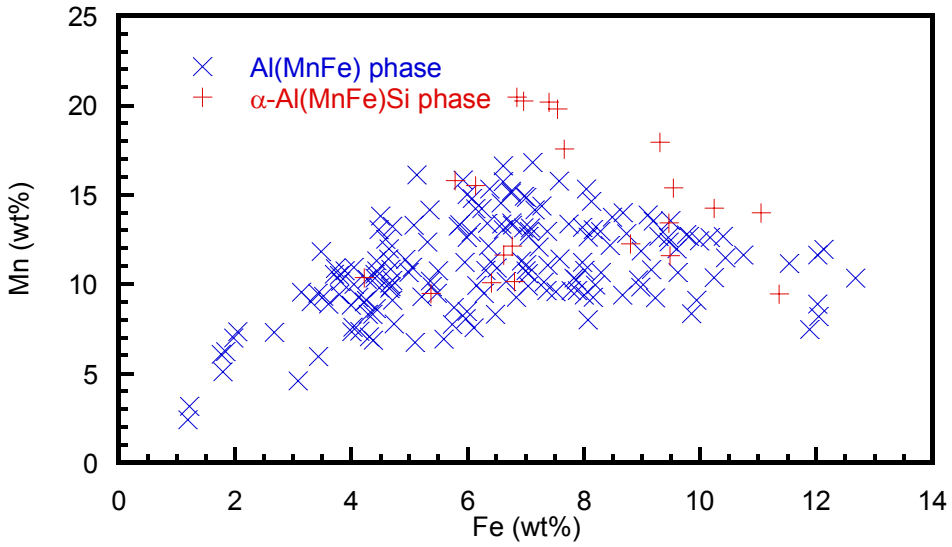

Figure 5.3 %Mn vs. %Fe in intermetallic particles of AA3005.

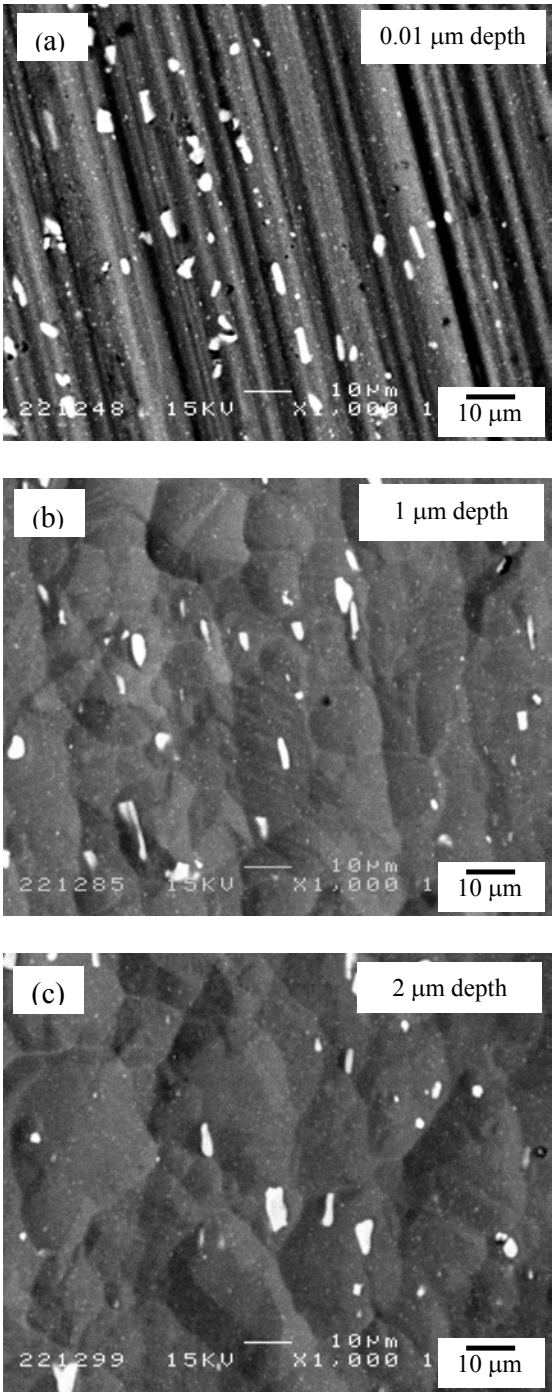

Figure 5.4 SEM BE image showing the particle distribution at different depths from the surface (a) 0.01 μm, (b) 1 μm and (c) 2 μm depth (equivalent to bulk which relates to TEM micrograph (Figure 2.11) showing a different microstructure between an active deformed layer and the bulk material) after GDOES etching.

SEM backscattered electron (BE) images of the surface at different depths after GDOES etching are shown in Figure 5.4. Figure 5.5 gives the particle count and total area fraction of the intermetallic particles. The number of particles (especially fine particle size less than 1 μm) is significantly higher at the surface compared with the bulk as shown in Figures 5.4 and 5.6. The minimum particle size detected by the image analysis was 0.5 μm. Figure 5.5 shows that there is an increase in the area fraction of particles as well as the number density at the surface. The particle size distribution analysis (Figure 5.6) shows that the number of small particles (0.5-1 μm) is significantly higher at the surface than the bulk. On the other hand, the number of large particles is significant lower at the surface than the bulk as shown in Figure 5.7.

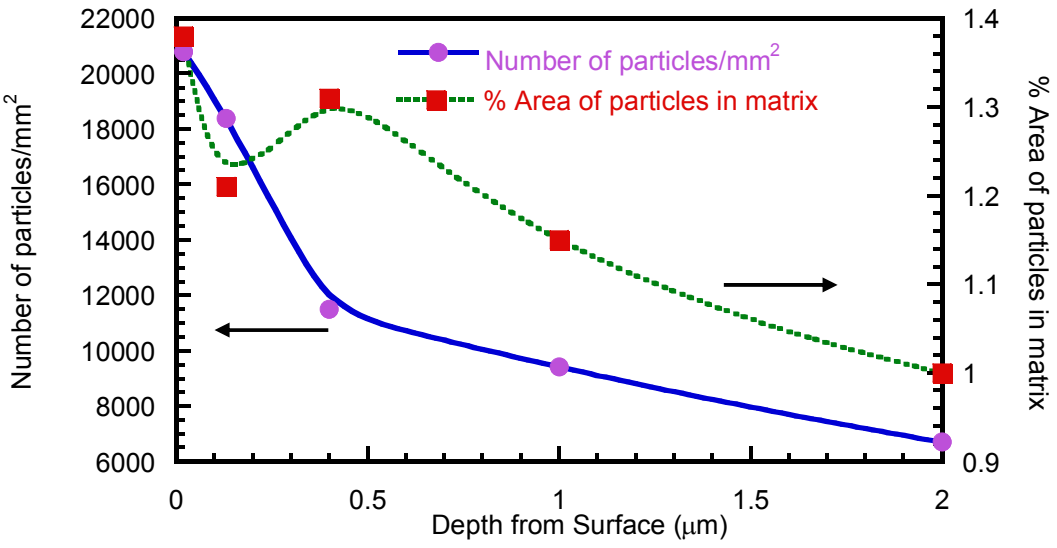

Figure 5.5 Total particle count (particles > 0.5 μm in size) and area fraction as a function of depth calculated from SEM BE images using image analysis.

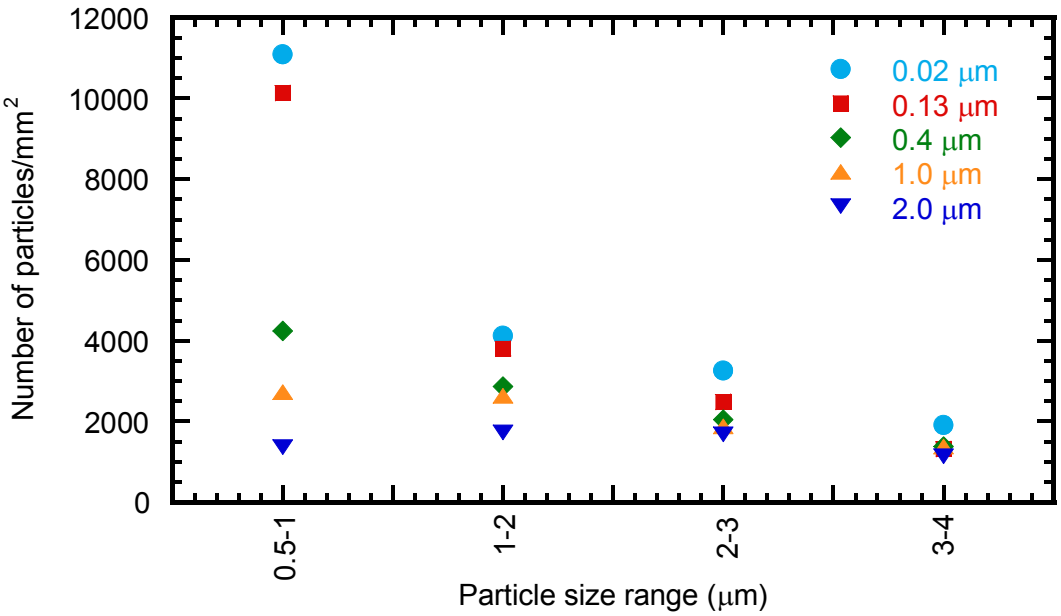

Figure 5.6 Particle size distribution (0.5-4 μm) of AA3005 at different depths.

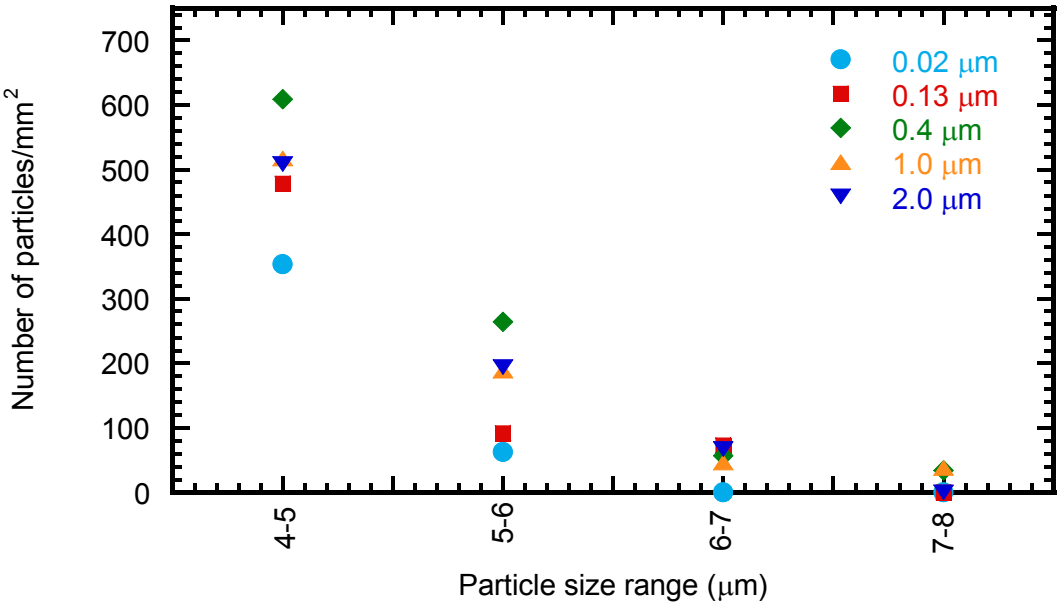

Figure 5.7 Particle size distribution (4-8 μm) of AA3005 at different depths.

5.3 Electrochemical measurements

5.3.1 In-situ observation of corrosion

The reactivity of the surface as a function of depth was determined by etching to different depths with GDOES, and monitoring the corrosion behaviour in naturally aerated 1 M HCl using a video camera attached to an optical microscope. The shoulder of the GDOES crater and the surrounding region were masked with lacquer. Figure 5.8 shows still images taken from the video during an 8 minute immersion test. For all depths, small hydrogen bubbles can be seen evolving across the entire surface. At the surface (0.02 μm), the bubbles are very small and more numerous, consistent with the fine distribution of particles observed in Figure 5.4-5.7. Fewer, larger bubbles are observed at greater depths.

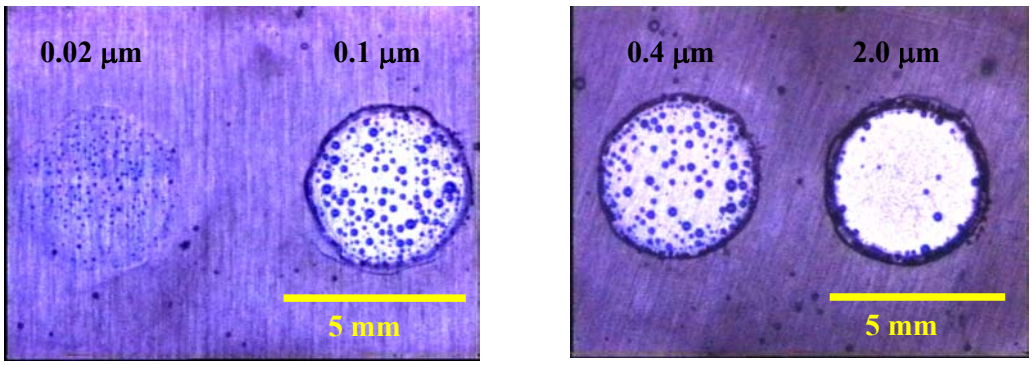

Figure 5.8 In situ observation of corrosion in naturally aerated 1 M HCl in GDOES craters sputtered to different depths.

5.3.2 Potentiodynamic cathodic and anodic polarisations

The anodic and cathodic reactivities of the material at different depths were studied using potentiodynamic polarisation experiments on specimens that were etched to different depths with GDOES sputtering.

Figure 5.9 shows the anodic polarisation curves for the material in de-aerated 0.85 M NaCl, pH 11.5, at the depths of 0.13, 0.4 and 2.0 μm. The passive current density is slightly higher for the surface (0.13 μm) and the breakdown potential slightly lower. During the reverse scan, the repassivation current dips below passive level, owing to hydrogen evolution within acidic pit cavities.

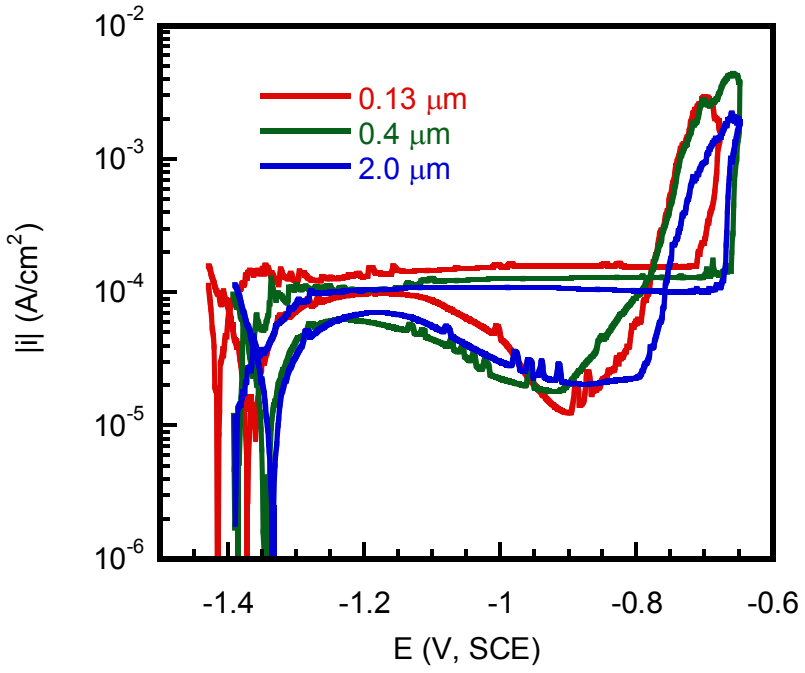

Figure 5.9 Anodic polarisation curves for AA3005 at different depths in de-aerated 0.85 M NaCl, pH 11.5.

Figure 5.10 shows anodic polarisation curves for the materials in de-aerated 0.85 M NaCl, pH 3, sputtered to different depths with GDOES. The anodic potential at 50 μA/cm^2 of the material at different depths is shown in Figure 5.11. The data in Figure 5.11 which were collected from repeated measurements show reproducibility. It is clear that the surface, 0.02 μm, is highly active compared with the bulk (2 μm depth).

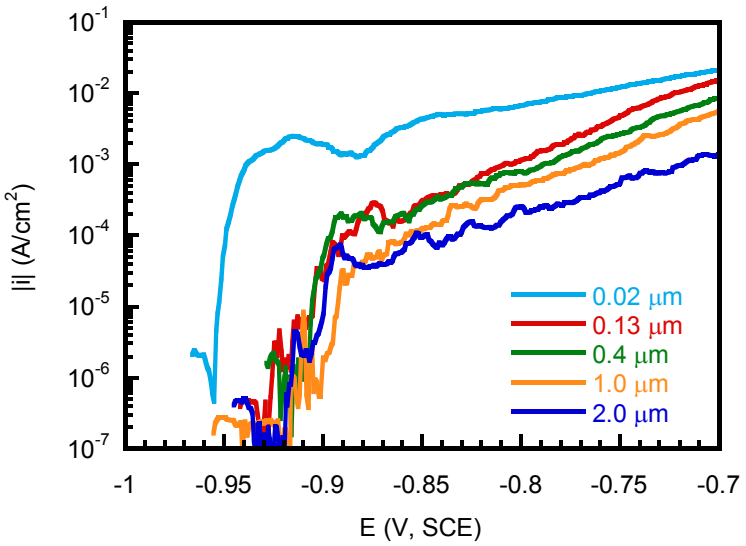

Figure 5.10 Anodic polarisation curves for AA3005 at different depths in de-aerated 0.85 M NaCl, pH 3.

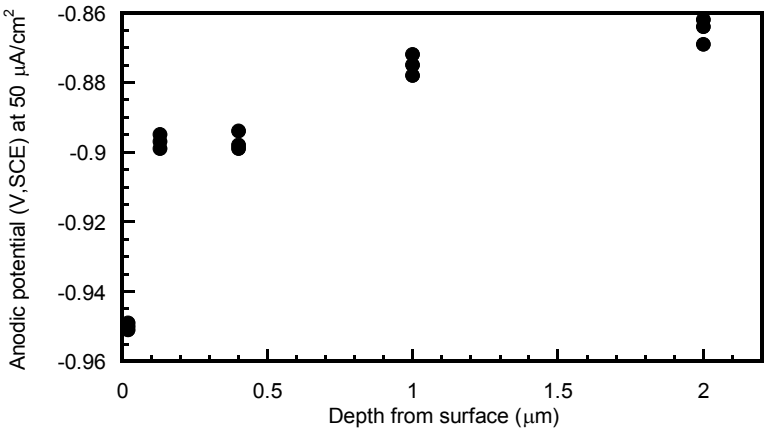

Figure 5.11 Anodic potential (V, SCE) at a current density of 50 μA/cm^2 for AA3005 at different depths in de-aerated 0.85 M NaCl, pH 3.

Figure 5.12 gives the cathodic polarisation curves at different depths in naturally aerated 0.85 M NaCl, pH 3. The cathodic current density at a potential of -1.15 V(SCE) for the material at different depths was plotted from the cathodic polarisation curves (Figure 5.12) as shown in Figure 5.13. The cathodic current density for the surface (0.02, 0.13, 0.4, and 1.0 μm depth) is almost an order of magnitude greater than that for the bulk (2 μm depth). These observations are in agreement with the immersion test results, where the hydrogen evolution reaction due to the cathodic reduction reaction at the surface was high.

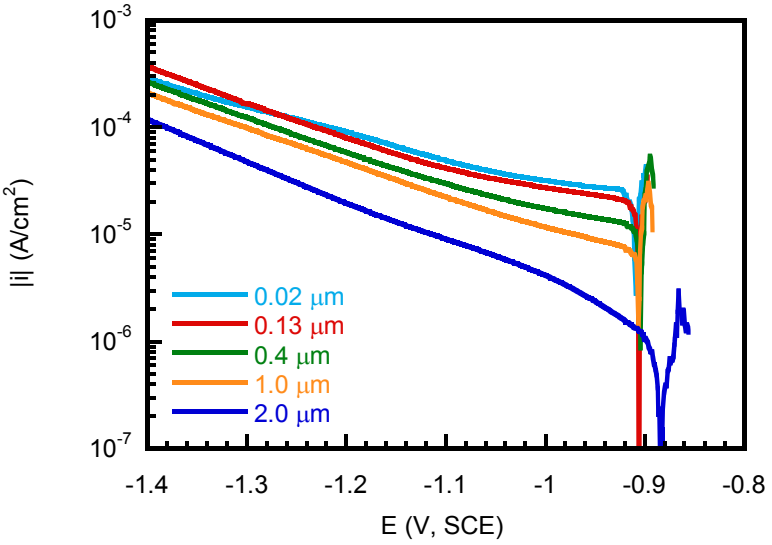

Figure 5.12 Cathodic polarisation curves for AA3005 at different depths in naturally aerated 0.85 M NaCl, pH 3.

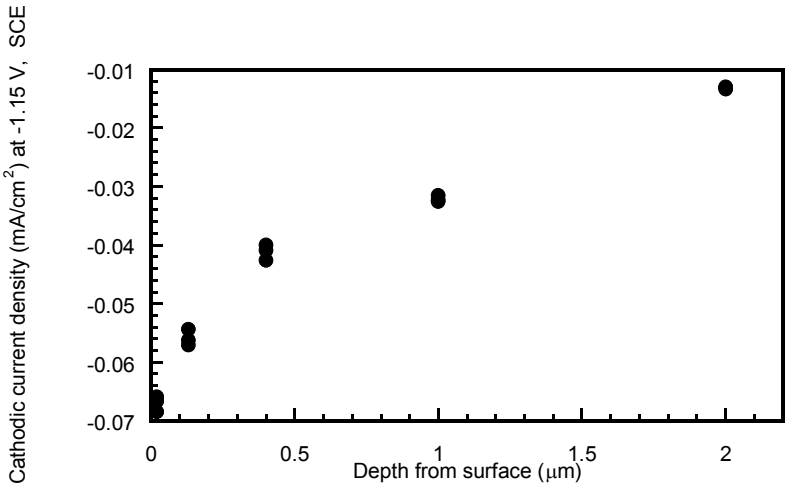

Figure 5.13 Cathodic current density (mA/cm^2) at potential -1.15 V(SCE) for AA3005 at different depths in naturally aerated 0.85 M NaCl, pH 3.

5.3.3 Potentiostatic polarisation

The specimens etched to different depths were potentiostatically polarised at -1 V(SCE) in de-aerated 0.85 M NaCl, pH 11.5. At this potential, the material should be passive according to Figure 5.9. Figure 5.14 gives the plot of current vs. time for three different depths. In agreement with the results in Figure 5.9, the surface showed a higher current density than the bulk.

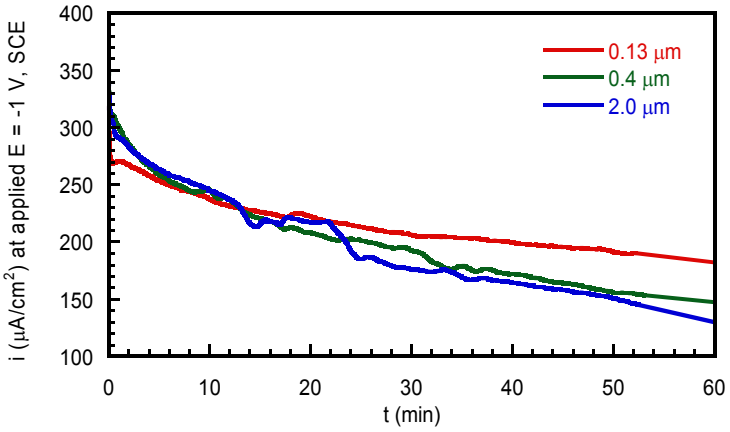

Figure 5.14 Potentiostatic polarisation curves at -1 V, SCE in de-aerated 0.85 M NaCl, pH 11.5 for AA3005 sheet sputtered to different depths.

5.3.4 Corrosion surface morphology

Figure 5.15 shows the typical surface morphology of the corroded surface after potentiodynamic anodic polarisation to -0.5 V(SCE) in de-aerated 0.85 M NaCl, pH 3. Both the surface and bulk suffer pitting as a result of the anodic polarisation. However, size of the pits is smaller at the surface while the bulk shows for fewer larger pits. The internal part of pit show crystallographic dissolution typical of an acidic pit. Faceted crystallographic planes can be seen inside the pit (Figure 5.16), as well as the intermetallic particles that act as pit initiation sites. After cathodic polarisation, the images do not show any corrosion sites.

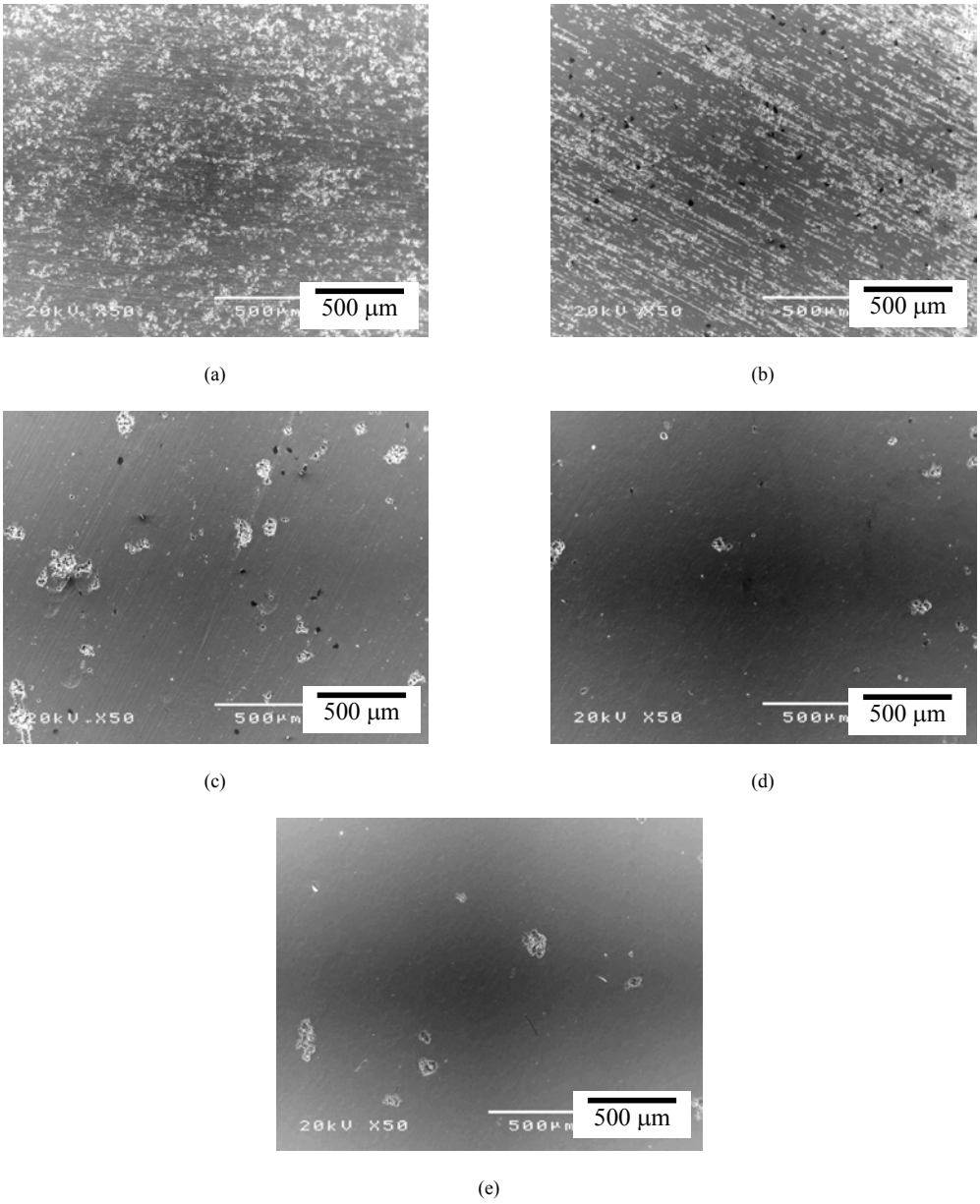

Figure 5.15 Surface morphology of the alloy after anodic polarisation in de-aerated 0.85 M NaCl pH 3 to -0.5 V(SCE) at depths of (a) 0.02 µm, (b) 0.13 µm, (c) 0.4 µm, (d) 1 µm, and (e) 2 µm.

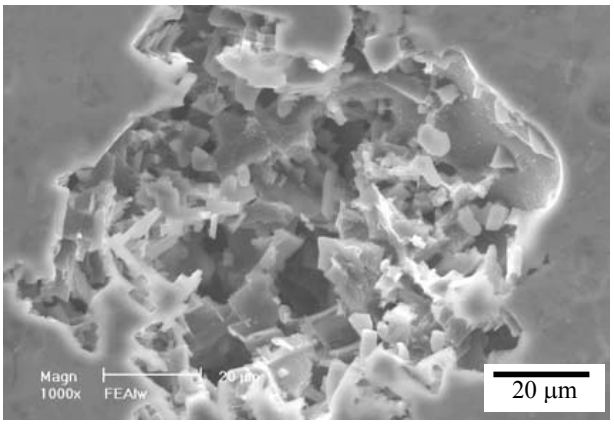

(a)

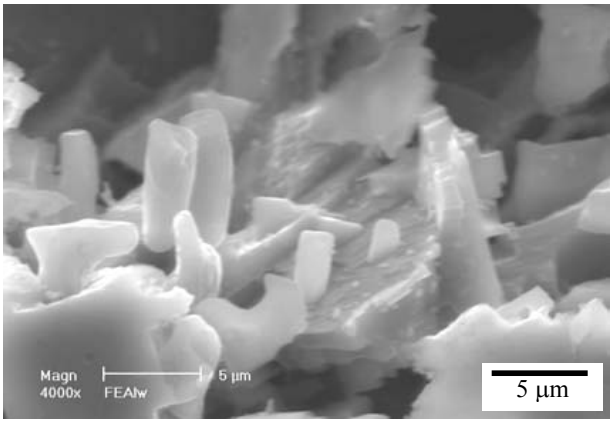

(b)

Figure 5.16 Surface morphology of the alloy after anodic polarisation in de-aerated 0.85 M NaCl, pH 3 to -0.5 V(SCE) at 2 µm depth with interior structure of pit shows undissolved crystallographic facets with intermetallic particles: (a) at low magnification and (b) at high magnification.

5.4 Discussion

Wrought aluminium alloys are produced from cast ingots, the structures of which are greatly changed by the various working operations (e.g. hot working and cold working during fabrication) and thermal treatments [2]. Hot rolling and cold rolling affect the microstructure and texture of the alloys [8, 10, 12, 40]. Fishkis and Lin [10] found that the heavily deformed, micrograined layer at the surface of rolled aluminium alloy sheet can be attributed to a higher shear deformation of the surface region in the rolling process. The enhanced shear deformation at the surface produces fine intermetallic particles as a result of fragmentation of larger intermetallic particles exposed at the surface, and an additional number of fine dispersoids nucleated during further annealing. Micrographs of the surface at different depths after GDOES etching of an annealed commercial cold rolled AA3005 sheet are shown in Figure 5.4 (a)-(c). As shown in Figure 5.4 (c), large particles are found in the bulk while a greater number of fine dispersoids is found at the surface of an AA3005 cold rolled sheet and subsequent annealing, as shown in Figure 5.4 (a). The particle count and total area of intermetallic particles in the matrix are given in Figure 5.5. The surface layer contains fewer larger particles and more fine intermetallic particles (Figures 5.4, 5.6 and 5.7). The observation that there is much change in the distribution of large particles suggests that fragmentation of particles may be significant. The increase in the total area of intermetallic particles, in particular small particles, indicates that nucleation and growth of intermetallic particles have taken place at the surface during annealing in addition to fragmentation. It is possible that intermetallic particles of sizes finer than the resolution limit of the SEM could be present in the alloy.

It is known that deformation can affect precipitation behaviour [46-50]. Senkov et al. [49] found that enhanced surface deformation of an Al-Fe alloy has an effect on precipitation kinetics. Luiggi [46-48] studied the effect of plastic deformation on the precipitation kinetics of AA 3004 containing α-$Al_{12}(MnFe)_3Si$ and $Al_6(MnFe)$ intermetallic particles. It was found that Mn diffusion is the dominant process in the precipitation kinetics. Deformation reduces the temperatures at which precipitation starts, and may increase the rate of precipitation at a given temperature by orders of magnitude [47].

The intermetallic particles in the deformed layer have much influence on corrosion susceptibility [11, 13, 14, 18, 22, 45, 147, 153]. As mentioned earlier, the formation of a highly deformed layer at the surface of rolled aluminium alloy sheet results from shear deformation during rolling [8, 10, 12, 40]. Subsequent annealing leads to enhanced precipitation of fine intermetallic particles in the surface layers. These fine intermetallic particles, in the case of AA3005 alloy, are found to be α-$Al_{12}(MnFe)_3Si$ phase [13, 14, 193] which are cathodically active relative to the aluminium matrix [133]. Therefore, these deformed layers have high cathodic reactivity [9, 11, 13, 14, 45, 149-151], as illustrated in Figure 5.12 and 5.13.

In situ observation of corrosion shows that many cathodic sites generating hydrogen bubbles can be observed for the surface up to 1 μm depth (Figure 5.8), while for the bulk only a few sites are active. The fine intermetallic particles at the surface

create numerous sites for hydrogen evolution while each site is quite small compared with the bulk.

The surface has higher anodic reactivity than the bulk, as shown in Figures 5.9, 5.10 and 5.11. It has been suggested that the increased precipitation at the surface causes a decrease in solute content of matrix, thus enhancing the anodic reactivity. Ambat and Davenport [194] found that the presence of Mn in solid solution provides better corrosion resistance and less pitting. Thus, the depletion of Mn at the surface is likely to have increased the anodic reactivity. Afseth and co-workers [14, 18, 147] investigated the corrosion behaviour of AA3005 hot rolled and cold rolled sheet. Preferential precipitation of a fine dispersion of intermetallic particles of the α-$Al_{12}(MnFe)_3Si$ phase occurs in the surface layer during high temperature heat treatment. It was deduced that this phenomenon causes depletion of the more noble alloying elements, e.g., Mn, in supersaturated solid solution in this region, thereby increasing the anodic reactivity of the aluminium matrix. Intermetallic particles also act as preferential pit initiation sites [104, 118, 124, 125]. Thus, the higher density of intermetallic particles found at the surface leads to a larger number of pits, as shown in Figure 5.15.

Many investigators have reported the role played by the active surface layer found on rolled sheet in enhancing filiform corrosion susceptibility. [9, 13, 14, 23, 45, 149-151, 157, 170] The filiform corrosion behaviour of rolled aluminium alloys is controlled predominantly by the presence of a heavily deformed layer at the alloy surface comprising fine alloy grains with oxide-decorated boundaries with fine distribution of

intermetallic particles [9, 149-151]. Compared with the underlying bulk material, the microstructural features of the surface layers render them electrochemically reactive and susceptible to corrosion, resulting in relatively rapid and extensive propagation of filiform corrosion.

The present work has highlighted the combined effects of enhanced precipitation and solute depletion in increasing both anodic and cathodic reactivity of surface.

5.5 Summary

The enhanced deformation at the surface of a rolled commercial AA3005 alloy sheet resulted in an increased number of fine intermetallic particles after heat treatment. These resulted from both fragmentation of existing particles and nucleation and growth of new precipitates. The surface layers of the alloy up to about 1 μm depth showed higher cathodic reactivity due to an increased number of Al(MnFe) and α-Al(MnFe)Si precipitates. Pit initiation is enhanced at the surface owing to the increased density of intermetallic particles, and it is likely that solute depletion from the matrix, particularly of Mn, will contribute to the enhanced anodic reactivity.

Chapter 6 Effect of Deformation on the Electrochemical Behaviour of Al-1Mn-0.4Fe-0.3Si

Deformation is likely to have two effects on the corrosion of aluminium alloys. One is to cause the precipitation of intermetallic particles that act as local cathodes and pit initiation sites. The other is the depletion of adjacent matrix in solute as a consequence of precipitation, making it more susceptible to dissolution. This work aims to investigate material deformed using uniaxial compression and equal channel angular extrusion (ECAE) of an Al-1Mn-0.4Fe-0.3Si model alloy and to study the effect of deformation on electrochemical behaviour of this alloy.

6.1 Uniaxial Compression

A series of samples were prepared by uniaxial compression at different levels of deformation and then annealed at 400°C for 2 h and furnace cooled.

6.1.1 Microstructure morphology

The SEM back-scattered images of samples that have received different levels of deformation and subsequent annealing are shown in Figures 6.1(a)–(e) at low magnification and Figures 6.2(a)–(e) at high magnification. Figures 6.1(a)–(e) show that higher deformation leads to fragmentation of the larger constituent particles. Figures

6.2(a)–(e) show that fine dispersoid particles appear to be larger and numerous after a high level of deformation (50% and 80% deformation) and subsequent annealing. Furthermore, these images show a depletion zone between constituent particles and dispersoid particles.

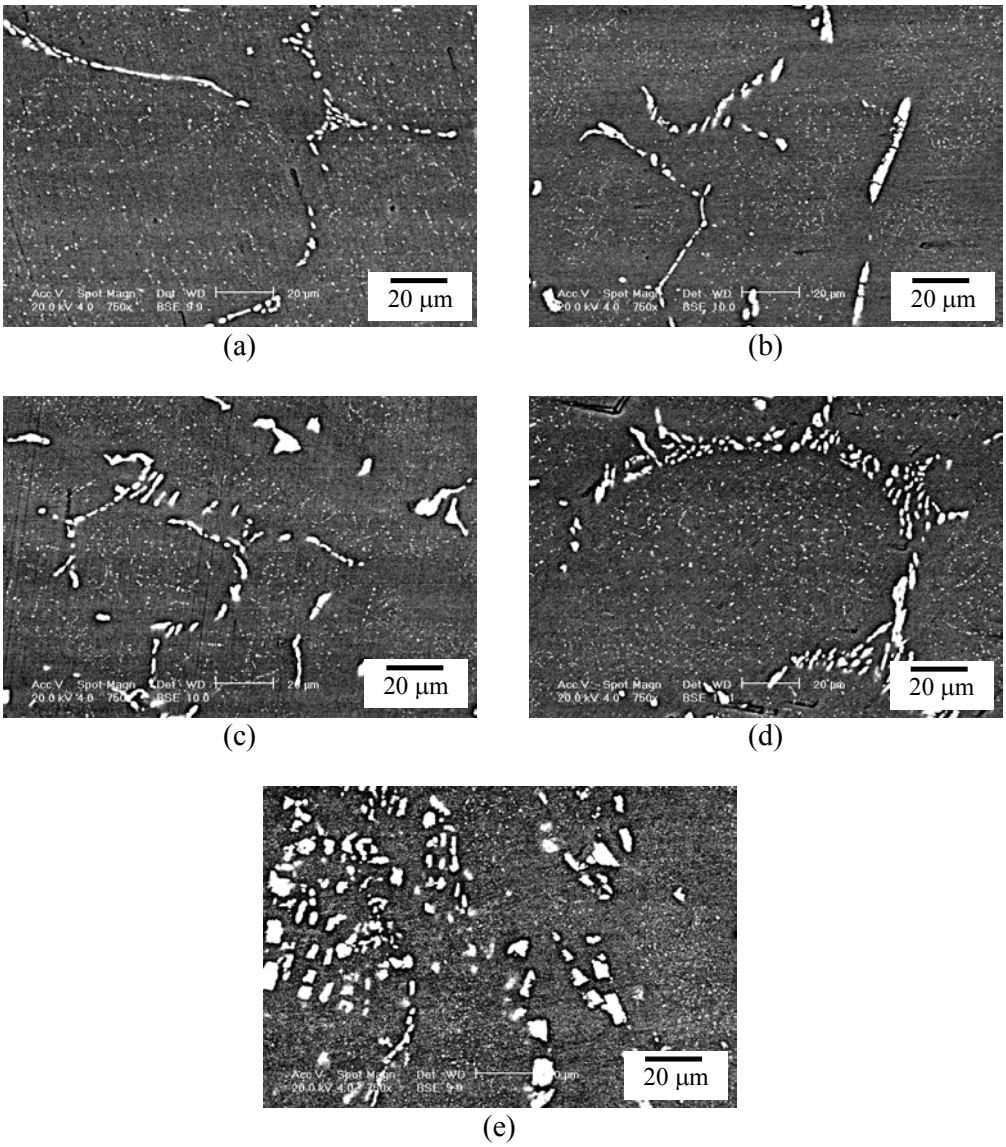

Figure 6.1 SEM back-scattered images at low magnification of Al-1Mn-0.4Fe-0.3Si subjected to different levels of deformation and subsequent annealing: (a) no deformation (as cast), (b) 10% deformation, (c) 25% deformation, (d) 50% deformation and (e) 80% deformation.

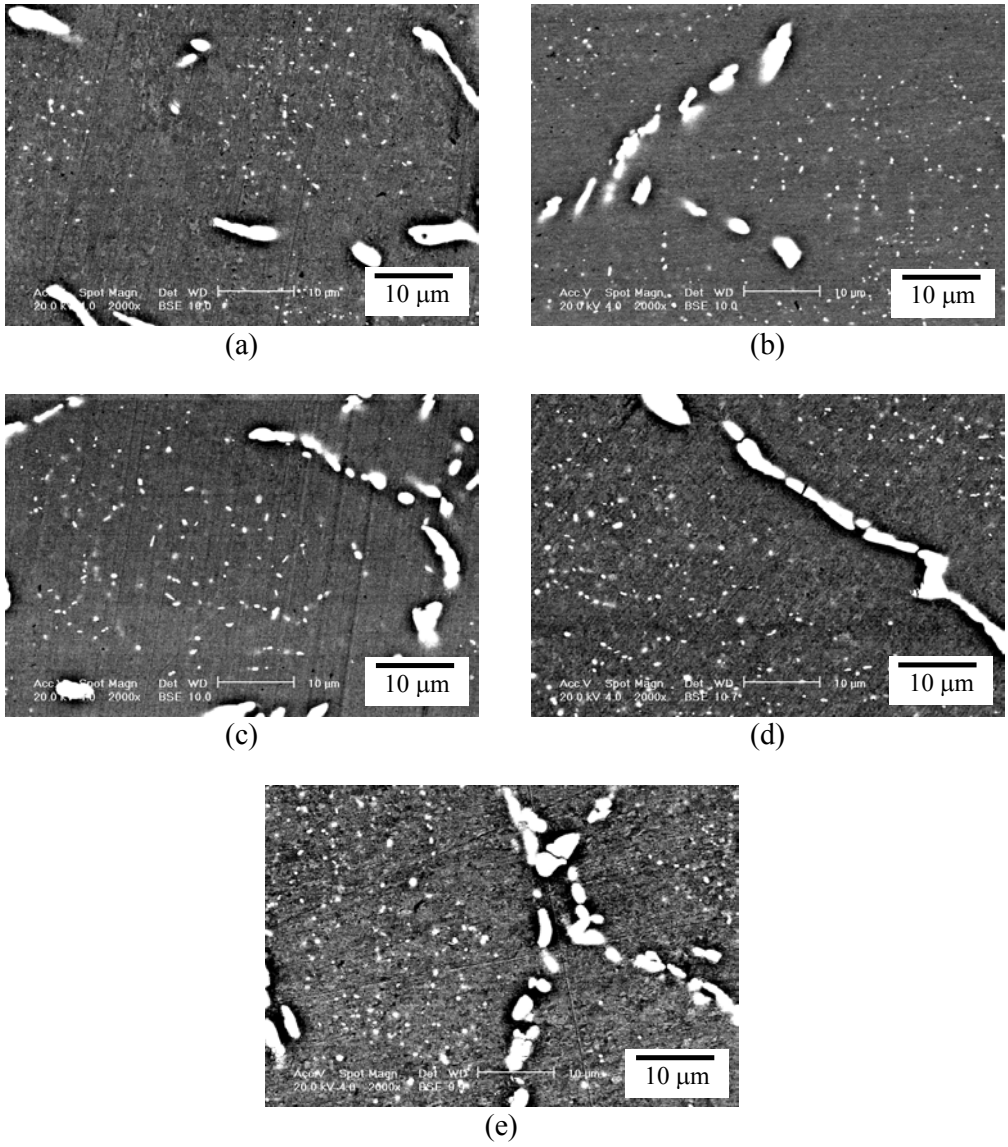

Figure 6.2 SEM back-scattered images at high magnification of Al-1Mn-0.4Fe-0.3Si subjected to different levels of deformation and subsequent annealing: (a) no deformation (as cast), (b) 10% deformation, (c) 25% deformation, (d) 50% deformation and (e) 80% deformation.

The intermetallic particles larger than 1 μm were analysed using EDX. A typical result is shown in Figures 6.3(a) and (b). These intermetallic particles are found to be enriched in Fe, Mn, and Si. Figures 6.4–6.6 show the concentration of Mn vs. Fe, Mn vs. Si and Fe vs. Si, respectively, in intermetallic particles. There appears to be a single

population of particles with approximately constant elemental ratios, apart from a few particles with anomalously high Fe contents. The average %Mn, %Fe and %Si are 13% ± 3%, 10% ± 3%, and 7% ± 1%, respectively. The iron to manganese ratio is 0.8 ± 0.3. This composition is close to α-$Al_{12}(Fe,Mn)_3Si$ phase, which was also found in a rolled AA 3005 analogue model alloy (Al-1Mn-0.5Mg-0.4Fe-0.3Si), studied by Afseth and co-workers [45]. They found that this alloy contains only α-$Al_{12}(MnFe)_3Si$ phase with an iron to manganese ratio of 0.7.

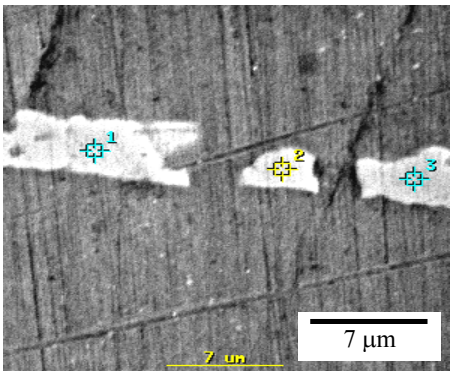

(a)

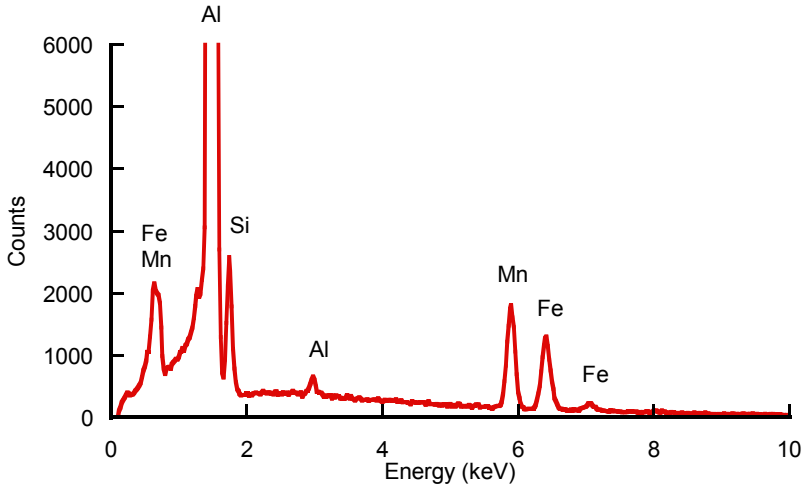

(b)

Figure 6.3 Analysis of an intermetallic particle on undeformed Al-1Mn-0.4Fe-0.3Si after solution heat-treatment and annealing: (a) SEM image and (b) EDX spectrum of the particle at position 1.

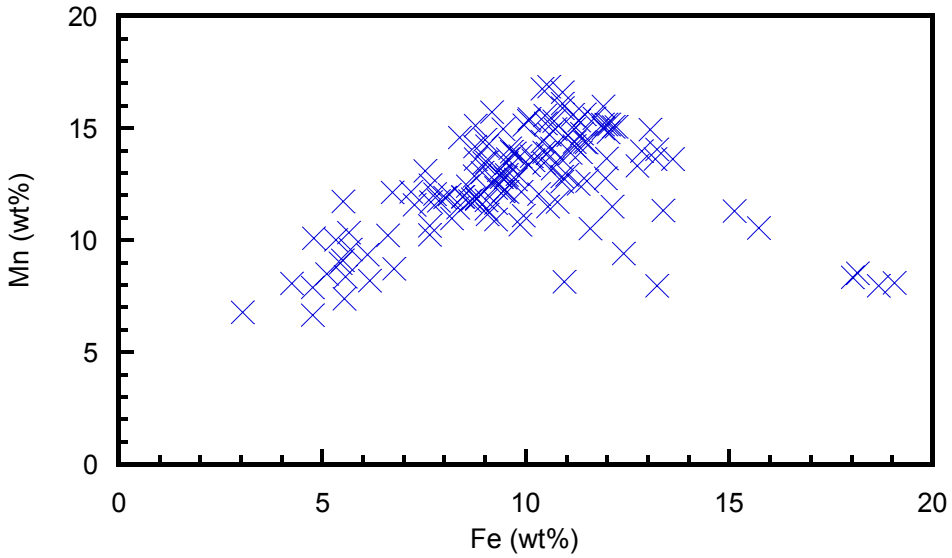

Figure 6.4 % Mn vs. % Fe in intermetallic particles of as cast Al-1Mn-0.4Fe-0.3Si after solid solution heat-treatment and annealing, determined from EDX.

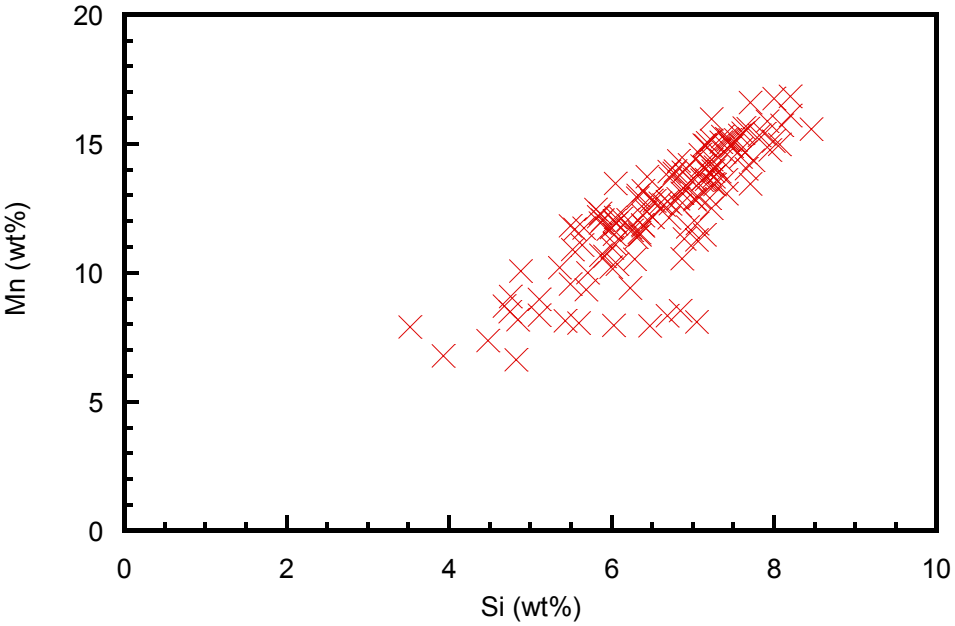

Figure 6.5 % Mn vs. % Si in intermetallic particles of as cast Al-1Mn-0.4Fe-0.3Si after solid solution heat-treatment and annealing, determined from EDX.

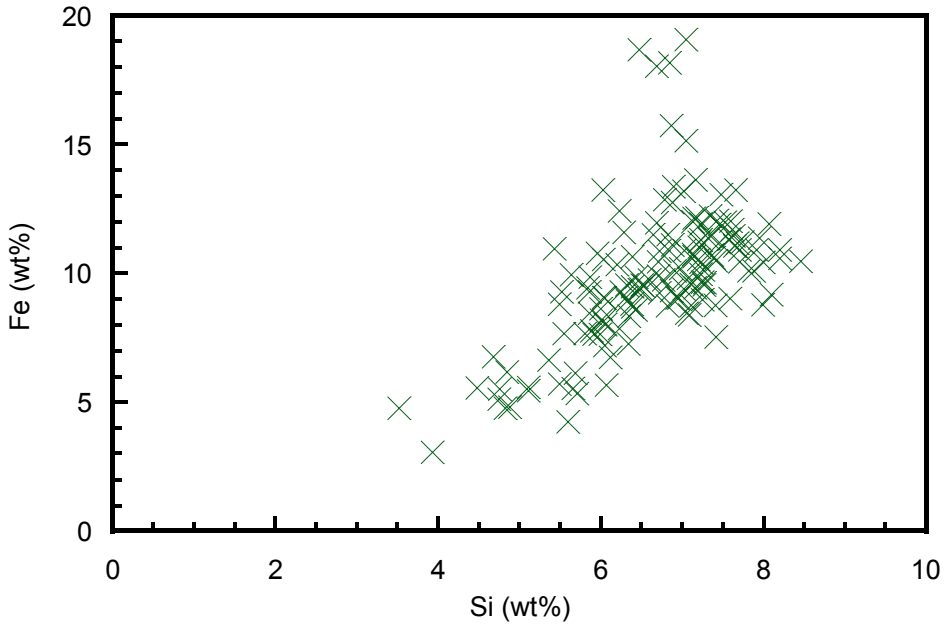

Figure 6.6 % Fe vs. % Si in intermetallic particles of as cast Al-1Mn-0.4Fe-0.3Si after solid solution heat-treatment and annealing, determined from EDX.

The optical micrographs of undeformed (as cast) and deformed samples after subsequent annealing are shown in Figures 6.7(a) and (b). The grain sizes of the undeformed and deformed samples show a significant difference as a result of deformation. Figure 6.7(a) shows the undeformed and annealed sample with an average grain size of between 1 and 2 mm. The grain size appears to have been reduced after 80% deformation and annealing as shown in Figure 6.7(b). The average grain size has been reduced to approximately 200–400 μm. The grains appear to be equiaxed.

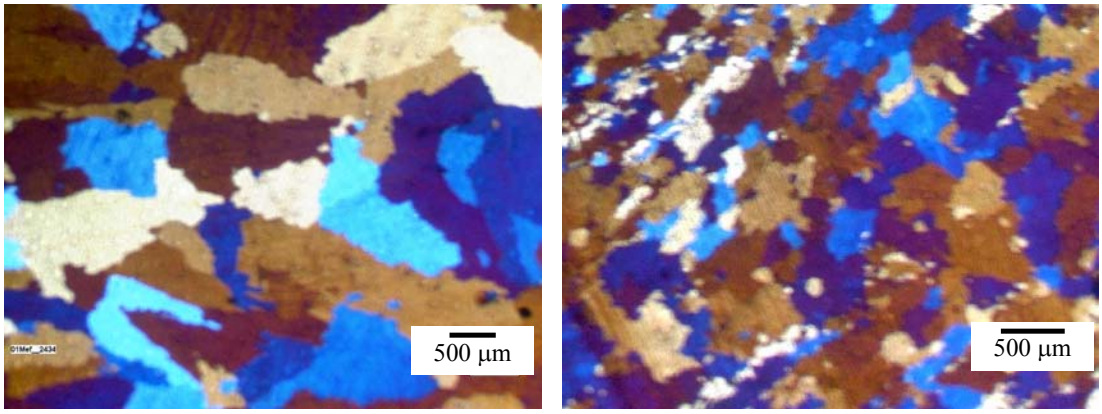

(a) (b)

Figure 6.7 Optical micrographs of (a) undeformed (as cast) and annealed sample and (b) 80% deformed and annealed sample of Al-1Mn-0.4Fe-0.3Si.

The SEM back-scattered micrographs shown in Figure 6.1 were used for particle size distribution analysis. The distribution curve is shown in Figure 6.8(a) and (b). The total number of intermetallic particles per unit area (mm^2) and the total area of particles for the different deformed and annealed samples are also given in Figure 6.9. In general, these figures support the observation that increased deformation and subsequent annealing leads to an increase in both the number and area of intermetallic particles. When the sample is deformed, the intermetallic particles break down to smaller particles. Subsequent annealing of deformed samples leads to precipitation of small particles (< 2 μm).

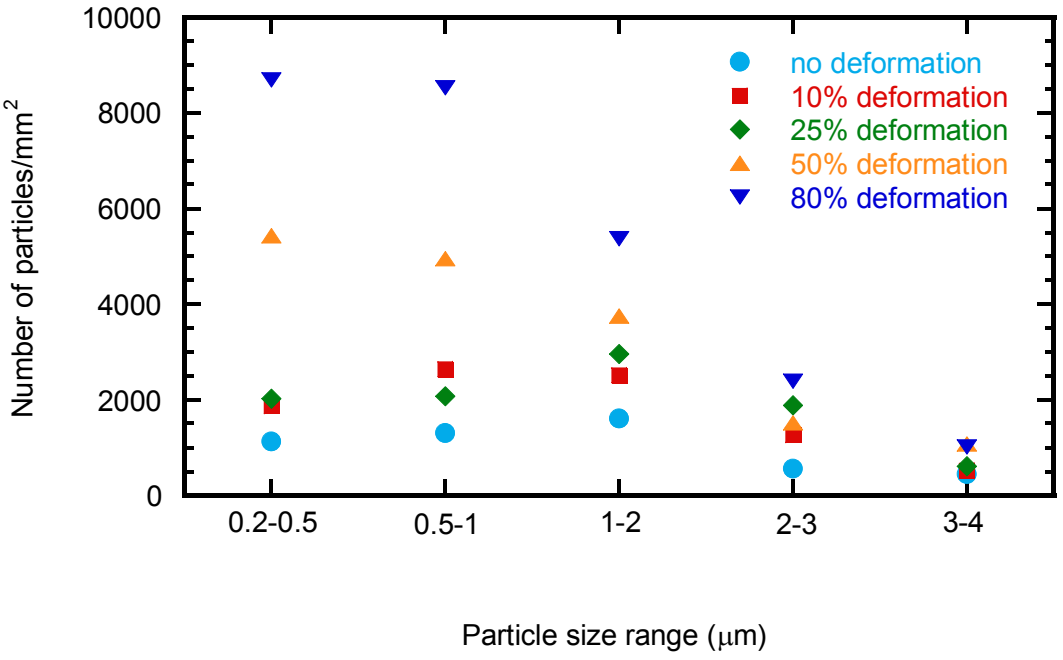

(a)

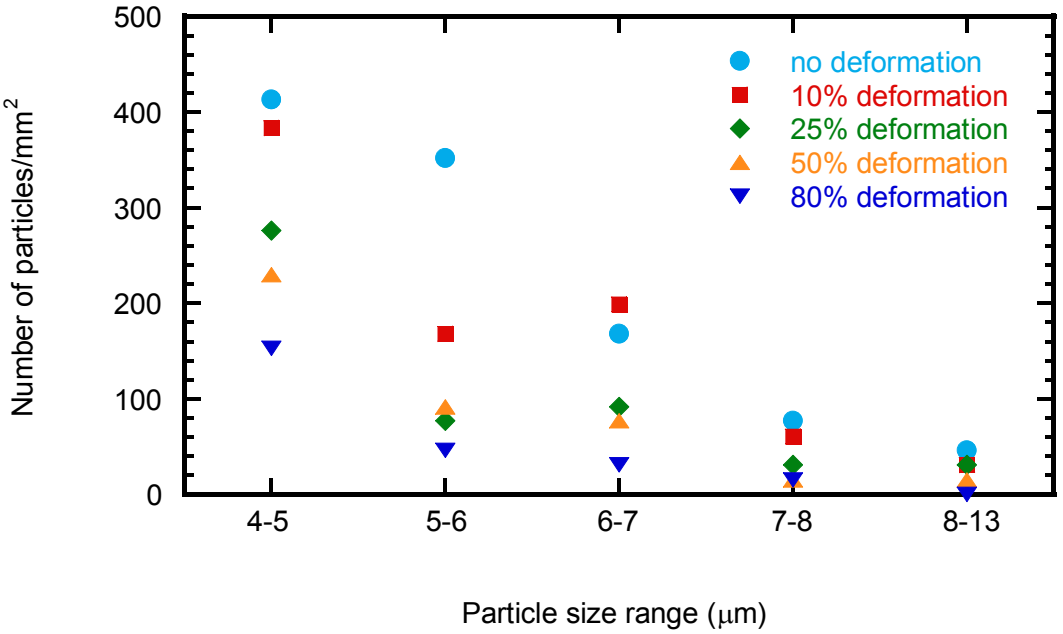

(b)

Figure 6.8 Particle size distribution after deformation to different levels and subsequent annealing for Al-1Mn-0.4Fe-0.3Si: (a) particle size range 0.2-4 μm and (b) particle size range 4-13 μm.

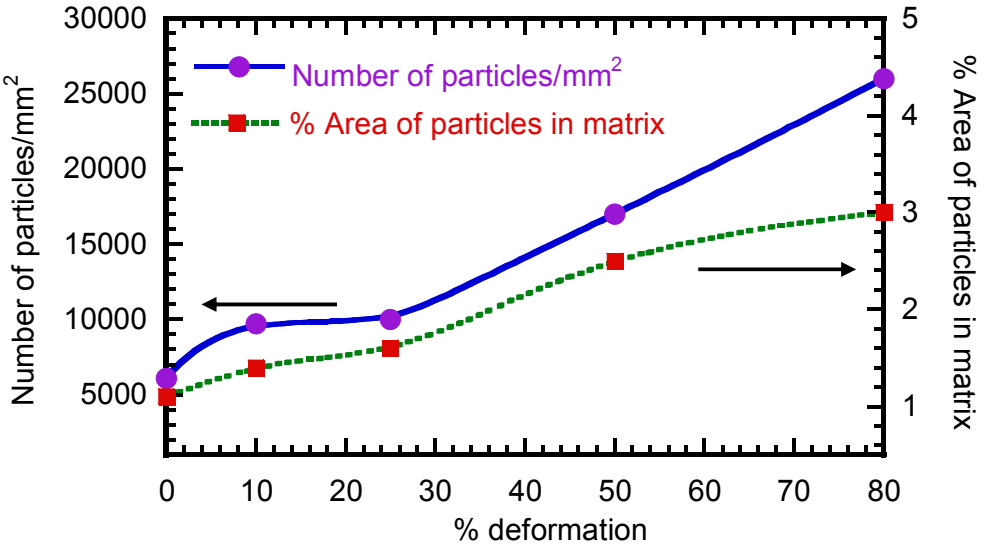

Figure 6.9 Total area fraction (% area) and number of particles (> 0.2 μm) per mm^2 for after deformation to different levels and annealing.

6.1.2 Electrochemical study of the effect of uniaxial compression

6.1.2.1 Potentiodynamic cathodic and anodic polarisations

The cathodic and anodic polarisation curves for the alloy with different degrees of deformation and subsequent annealing were measured in 0.85 M NaCl, pH 3 (acidified with CH_3COOH). Figures 6.10 and 6.12 show the cathodic and anodic polarisation curves, respectively. Generally, the deformed and annealed samples have higher cathodic and anodic reactivity than the undeformed and annealed sample.

The cathodic current density at a potential of –0.95 V(SCE) for different levels of deformation was plotted from the cathodic polarisation curves shown in Figure 6.11. The

data were collected from repeated measurements which showed good reproducibility. From Figure 6.10 and 6.11, it was found that the cathodic reactivity increases with the degree of deformation. However, the cathodic reactivity for the samples with 10% and 25% deformation was almost the same. The higher deformation (50% and 80% deformation) causes a further increase in the cathodic reactivity.

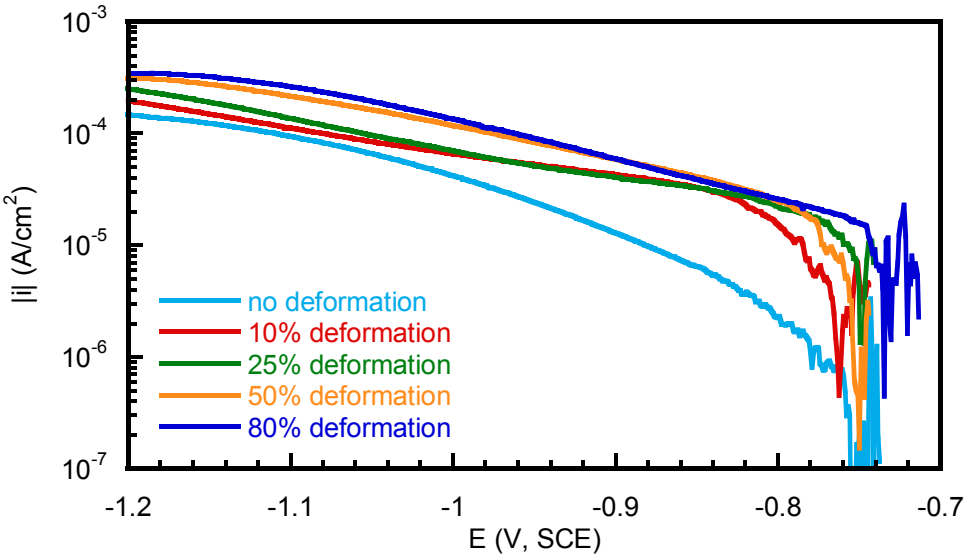

Figure 6.10 Cathodic polarisation curves of Al-1Mn-0.4Fe-0.3Si with different levels of deformation and subsequent annealing in naturally aerated 0.85 M NaCl, pH 3 (CH_3COOH).

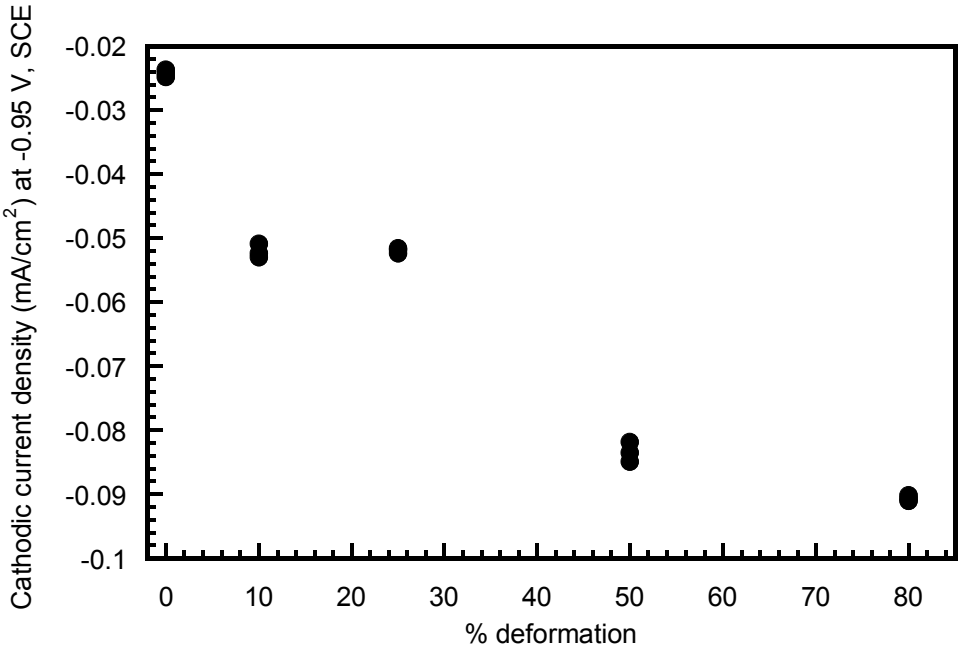

Figure 6.11 Cathodic current density (mA/cm^2) at –0.95 V(SCE) of Al-1Mn-0.4Fe-0.3Si with different levels of deformation and subsequent annealing in naturally aerated 0.85 M NaCl, pH 3 (CH_3COOH).

Figure 6.12 shows anodic polarisation curves for the material with different levels of deformation. The anodic potential at 100 μA/cm^2 was plotted from the anodic polarisation curves (Figure 6.12) as shown in Figure 6.13. The data were collected from repeated measurements and these data showed higher scatter on samples with high level of deformation (25%, 50% and 80% deformation). The undeformed and annealed sample has the lowest anodic reactivity compared to the deformed samples, as seen in Figures 6.12 and 6.13. The 80% deformation sample has lower anodic reactivity compared to the other deformed samples. The 10%, 25% and 50% deformation samples have almost the same anodic reactivity.

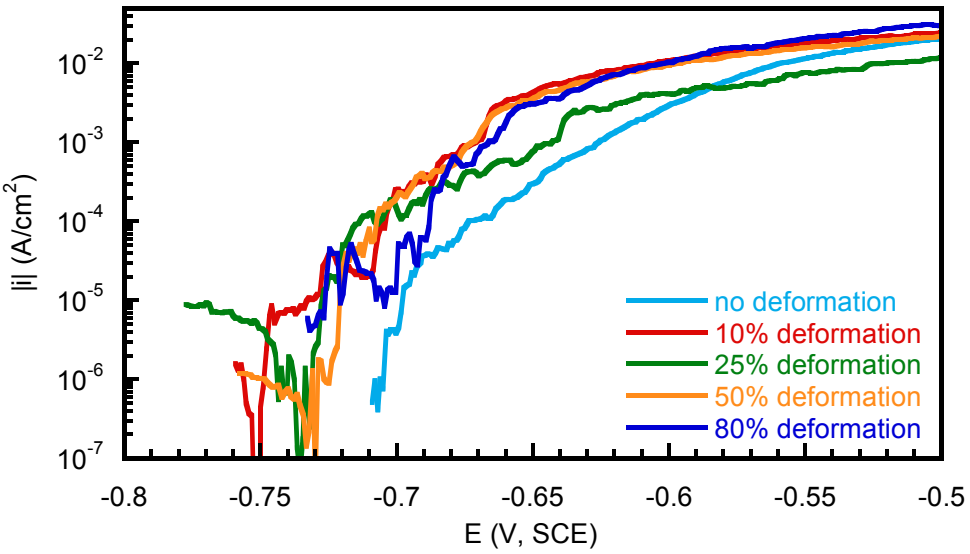

Figure 6.12 Anodic polarisation curves of Al-1Mn-0.4Fe-0.3Si with different levels of deformation and subsequent annealing in de-aerated 0.85 M NaCl, pH 3 (CH_3COOH).

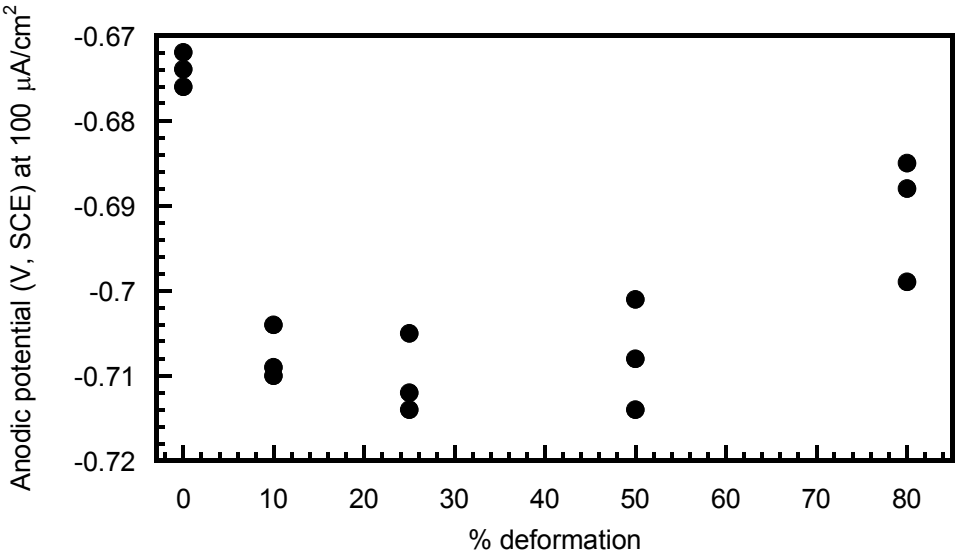

Figure 6.13 Anodic potential (V, SCE) at a current density of 100 µm/cm^2 for Al-1Mn-0.4Fe-0.3Si with different levels of deformation and subsequent annealing in de-aerated 0.85 M NaCl, pH 3 (CH_3COOH).

6.1.2.2 Corrosion surface morphology

Figure 6.14 shows the surface morphology of the corroded surface after anodic polarisation in de-aerated 0.85 M NaCl pH 3 to a potential –0.5 V(SCE). In general, these pictures show localised corrosion sites on the surface. The undeformed surface has fewer localised corrosion sites than the deformed surfaces. The 50% deformed sample has the highest number corrosion sites.

Figure 6.15 shows SEM images of a replica of the 50% deformed sample after anodic polarisation in de-aerated 0.85 M NaCl, pH 3. The internal structure of the pits shows undissolved crystallographic planes.

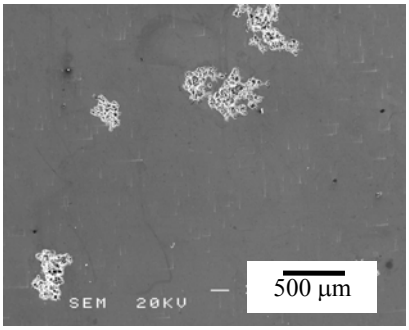

(a)

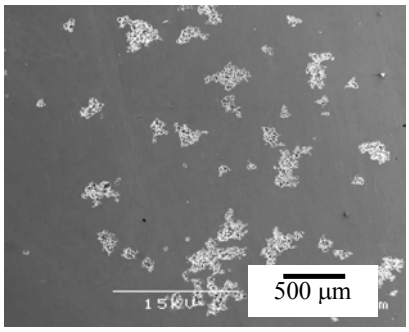

(b)

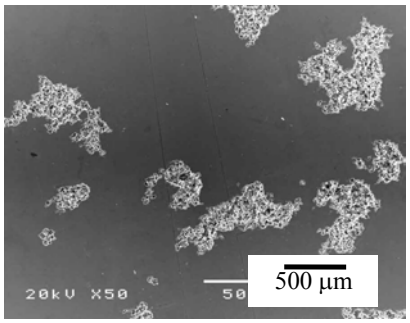

(c)

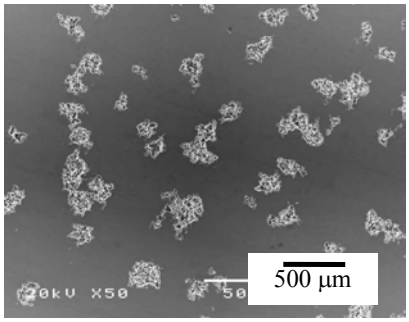

(d)

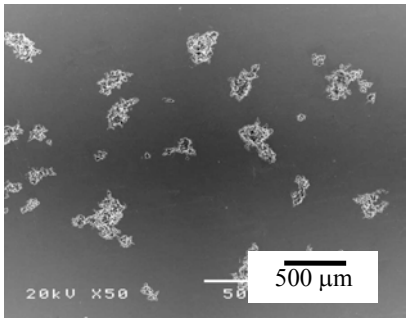

(e)

Figure 6.14 Morphology of the corroded surfaces after anodic polarisation in de-aerated 0.85 M NaCl, pH 3 (CH_3COOH), of Al-1Mn-0.4Fe-0.3Si with different levels of deformation and subsequent annealing: (a) no deformation, (b) 10% deformation, (c) 25% deformation, (d) 50% deformation, and (e) 80% deformation. Anodic polarisation was performed from the open circuit potential to -0.5 V(SCE) at a sweep rate of 1 mV/s.

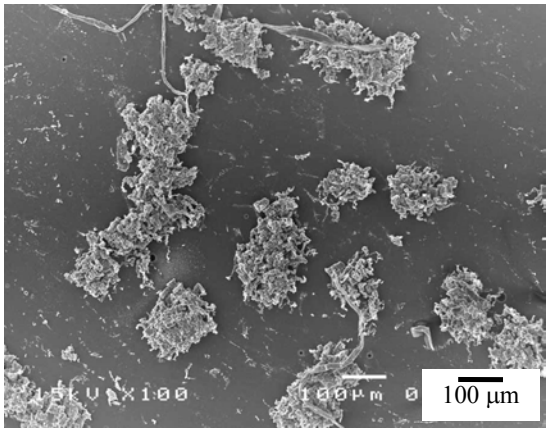

(a)

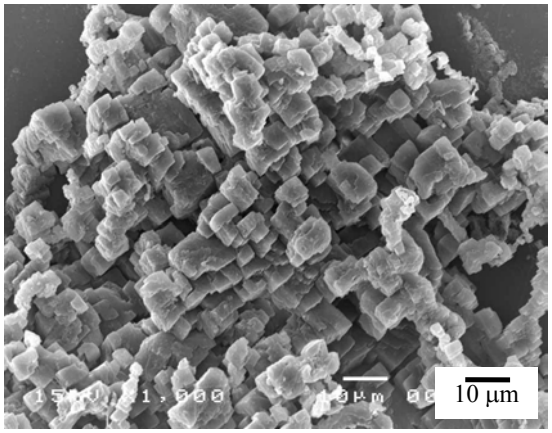

(b)

Figure 6.15 SEM picture of replica for surface of 50% deformation sample after anodic polarisation in de-aerated 0.85 M NaCl pH 3 (CH_3COOH): (a) at low magnification and (b) at high magnification.

6.2 Equal Channel Angular Extrusion

The model alloy Al-1Mn-0.4Fe-0.3Si was deformed by equal channel angular extrusion (ECAE), and then annealed at 400°C for 2 h and furnace cooled.

6.2.1 Microstructure morphology

Figures 6.16 and 6.17 show SEM back-scattered images of the undeformed (as cast) sample and ECAE deformed samples of the Al-1Mn-0.4Fe-0.3Si model alloy after annealing, at low and high magnification, respectively. Each sample shows a dark background of the aluminium matrix with a random distribution of lighter α-Al(MnFe)Si particles throughout the matrix.

Figures 6.16(a) and 6.17(a) show the microstructure of the heat-treated, undeformed as cast sample. In Figures 6.16(b)-(d) and 6.17 (b)-(d), it is evident that ECAE has had a significant effect on the alignment of the particles. They show a random distribution throughout the matrix. The particles have become more fragmented as a result of the shear stress introduced during ECAE processing. Figure 6.17 shows that ECAE processing followed by annealing leads to increased precipitation of fine dispersoid particles.

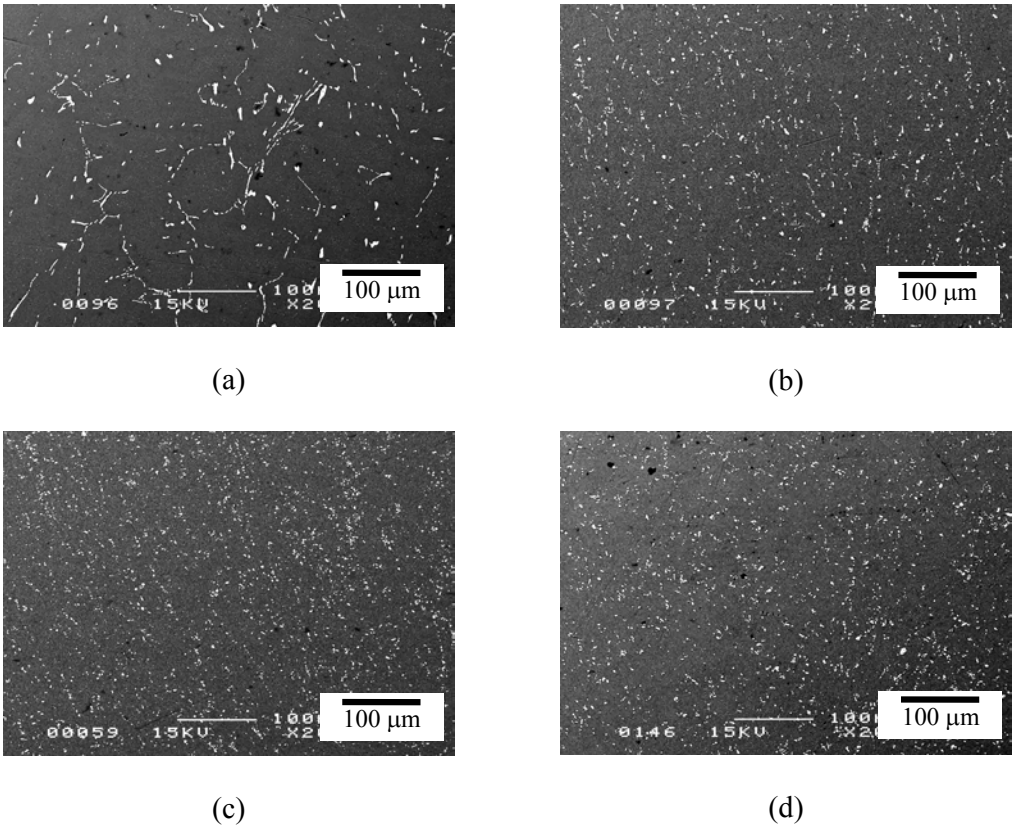

(a) (b)

(c) (d)

Figure 6.16 SEM back-scattered images at low magnification of Al-1Mn-0.4Fe-0.3Si subjected to different levels of ECAE deformation and subsequent annealing: (a) no deformation (as cast), (b) ECAE 3 passes, (c) ECAE 10 passes, and (d) ECAE 15 passes.

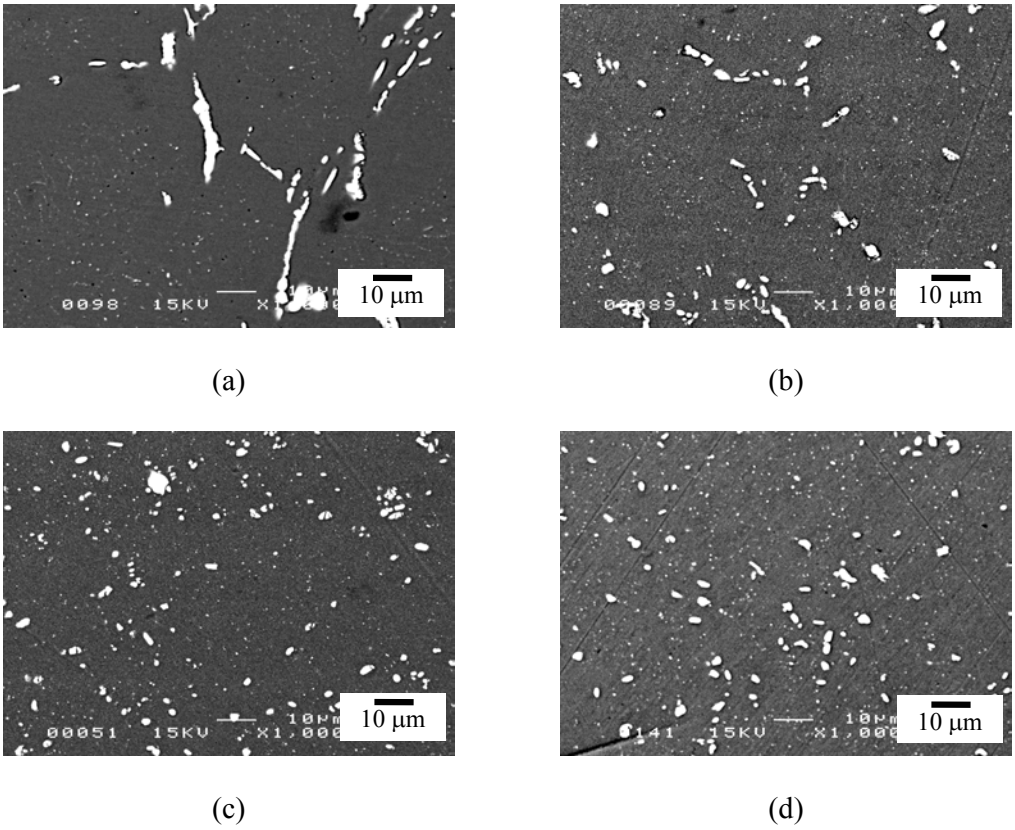

Figure 6.17 SEM back-scattered images at high magnification of Al-1Mn-0.4Fe-0.3Si subjected to different levels of ECAE deformation and subsequent annealing: (a) no deformation (as cast), (b) ECAE 3 passes, (c) ECAE 10 passes, and (d) ECAE 15 passes.

Electron back-scattered diffraction (EBSD) micrographs of the undeformed sample and ECAE-deformed samples are shown in Figures 6.19–6.22. The crystal orientation is identified using the colour key in Figure 6.18. Figure 6.19 shows the undeformed and subsequently annealed sample with a grain size between 1–2 mm. From Figures 6.20–6.22, it is clear that the grain sizes are greatly reduced as a result of ECAE processing and subsequent annealing. Figure 6.20 shows that the 3 ECAE pass sample have elongated grains with an average grain size of ~100–200 μm. Grain sizes at the centre and the edge of the sample are similar in size. After the specimen was extruded for 10 passes and subsequently annealed, the grain sizes were reduced to ~50–100 μm as shown in Figure 6.21. Grain sizes at the edge are smaller than at the centre. The grain size was greatly reduced after 15 passes and subsequent annealing with an average grain size of ~3–5 μm at the centre and ~4–6 μm at the edge (Figure 6.22). The grain size distribution at the centre seems to be more homogeneous than at the edge. Thus, all corrosion testing was investigated at the centre of the specimens.

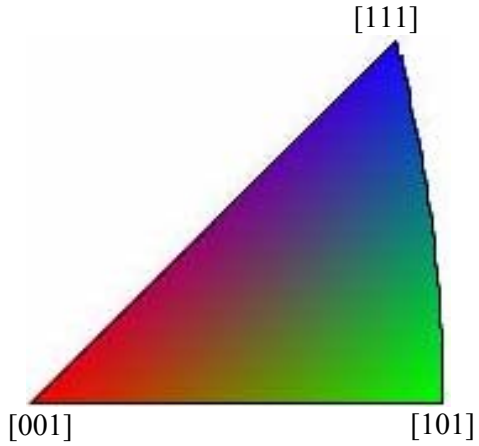

Figure 6.18 Color key for crystal orientation map.

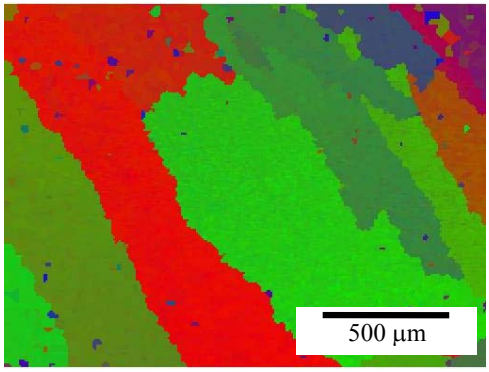

Figure 6.19 EBSD map for the undeformed (as cast) and subsequently annealed sample of Al-1Mn-0.4Fe-0.3Si.

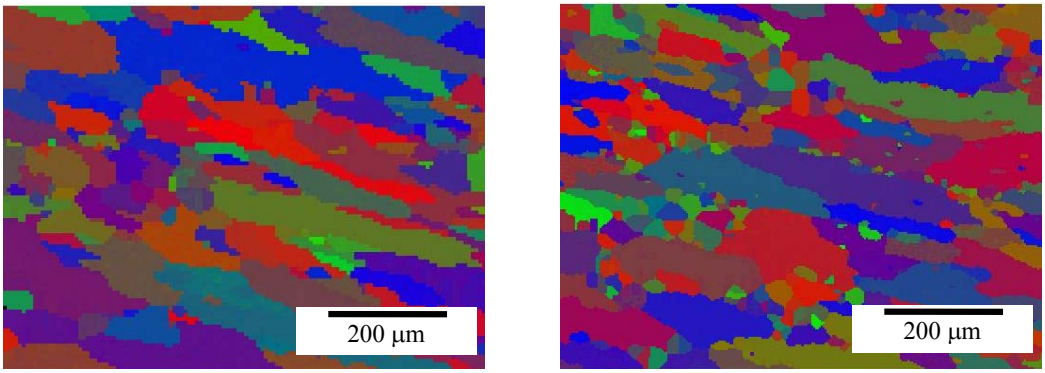

(a) (b)

Figure 6.20 EBSD map for the deformed Al-1Mn-0.4Fe-0.3Si after 3 ECAE passes and subsequent annealing: (a) at the centre and (b) at the edge.

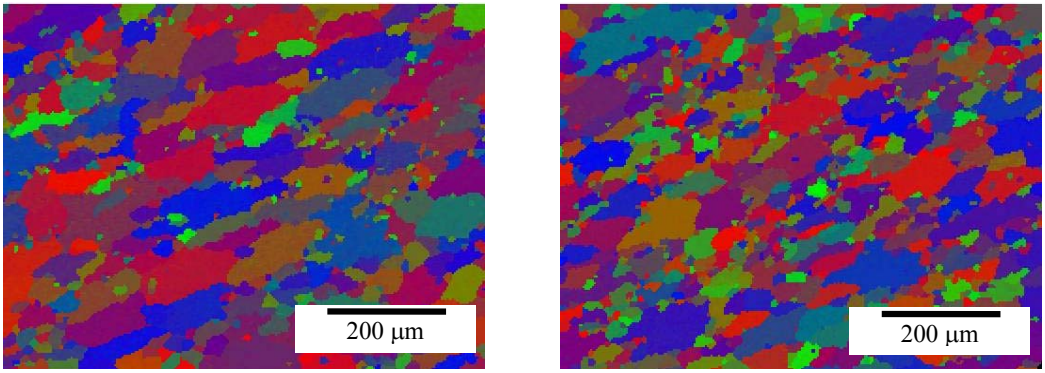

(a) (b)

Figure 6.21 EBSD map for the deformed Al-1Mn-0.4Fe-0.3Si after 10 ECAE passes and subsequent annealing: (a) at the centre and (b) at the edge.

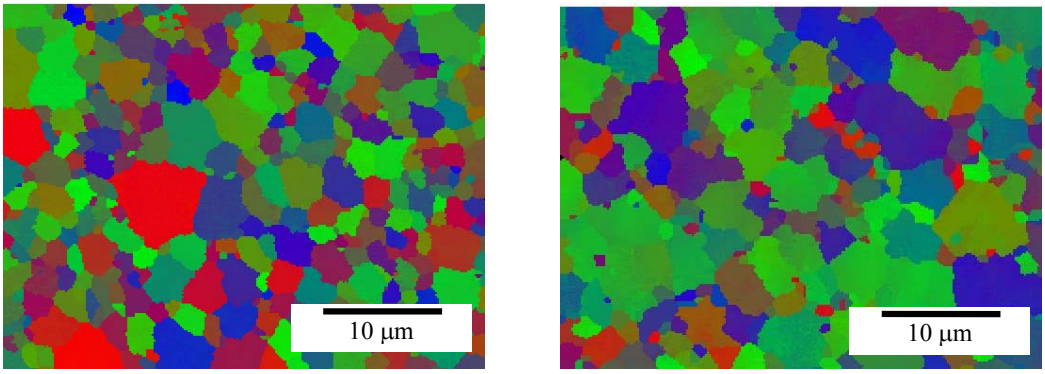

(a) (b)

Figure 6.22 EBSD map for the deformed Al-1Mn-0.4Fe-0.3Si after 15 passes ECAE and subsequent annealing: (a) at the centre and (b) at the edge.

The SEM back-scattered images shown in Figure 6.17 were used for particle counting and determination of the area fraction of particles in the matrix. The number of intermetallic particles per mm^2 and the total area of particles of the undeformed and ECAE deformed samples before and after annealing are given in Figures 6.23 and 6.24, respectively. Figure 6.23 shows that before annealing, the number of intermetallic particles gradually increases with the number of passes of ECAE. The total area fraction of particles (Figure 6.24) is slightly increased after ECAE processing. However, the area fraction remains unchanged on increasing the number of ECAE passes. After annealing, the number of particles per mm^2 is significantly increased and the total area of particles is slightly increased.

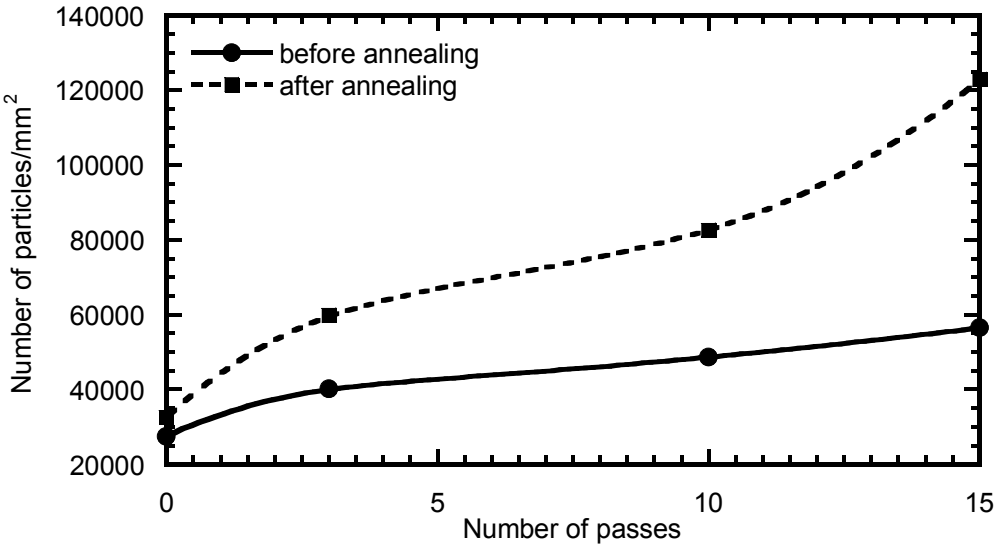

Figure 6.23 Number of particles/mm^2 in the matrix of undeformed and ECAE-deformed Al-1Mn-0.4Fe-0.3Si before and after annealing.

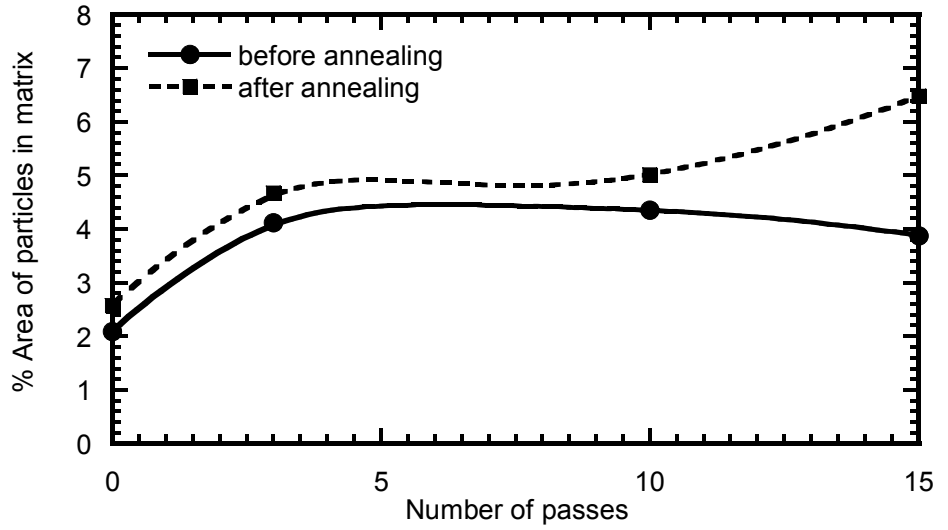

Figure 6.24 %Area of particles in undeformed and ECAE-deformed Al-1Mn-0.4Fe-0.3Si before and after annealing.

Figure 6.25 shows the particle size distribution for undeformed and ECAE-deformed samples before and after annealing. The number of larger particles found in deformed samples is less than that found in the undeformed sample. A higher fraction of fine particles (0.1-0.5 μm) was found on the deformed and subsequently annealed samples.

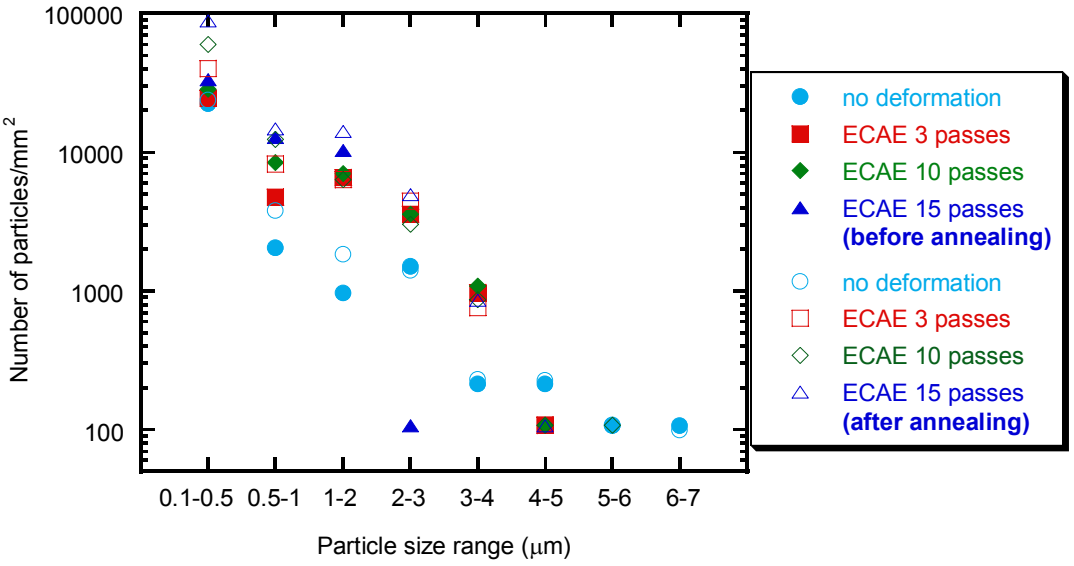

Figure 6.25 Particle size distribution of Al-1Mn-0.4Fe-0.3Si with different number of ECAE passes before and after annealing.

6.2.2 Hardness measurements

The Vickers hardness was measured using a 50 g load and readings were taken in 9 different areas, corresponding to the positions shown in Figure 6.26, on the undeformed and ECAE deformed samples before annealing. Figure 6.27 shows that the hardness is at a minimum before deformation and at a maximum after 15 ECAE passes.

The microstructure at each position for the sample treated with 3 ECAE passes is shown in Figure 6.28. It is found that the microstructure is inhomogeneous across the specimen. In some positions there are more intermetallic particles than at others. In order to avoid this variability, all the corrosion measurements were carried out at the centre of the specimens.

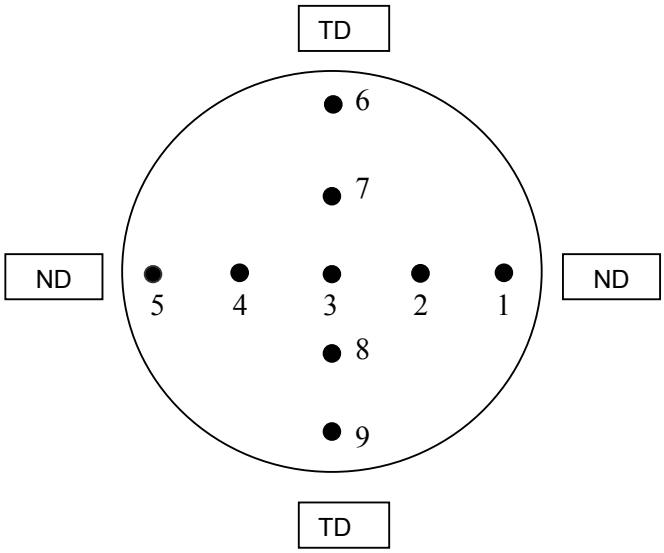

Figure 6.26 Schematic diagram showing areas where hardness measurements were taken (TD is transverse direction and ND is the vertical direction relative to the billet's axis in the die's symmetry plane as defined in Figure 3.2).

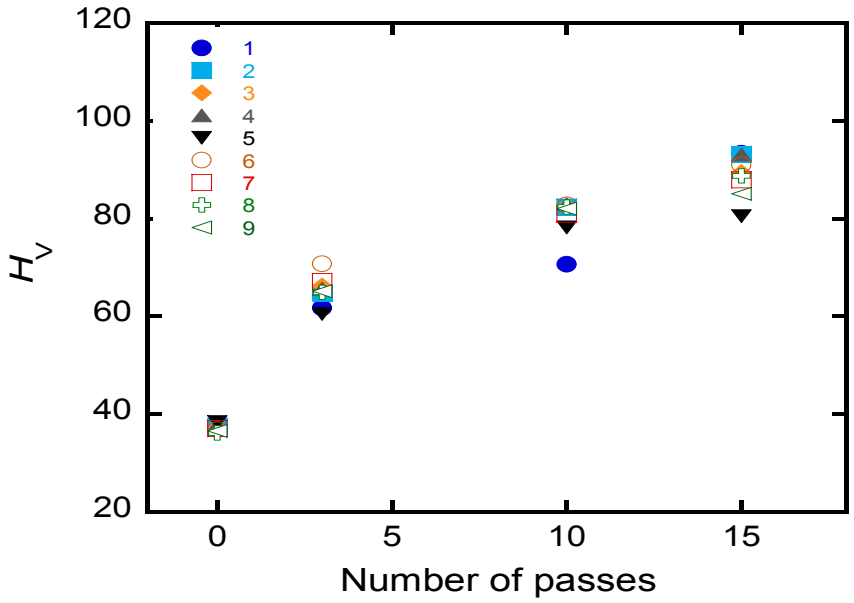

Figure 6.27 Hardness measurements (50 g load) for Al-1Mn-0.4Fe-0.3Si before annealing in the undeformed state (0 pass) and after different numbers of ECAE passes. The indicated positions are shown in Figure 6.26.

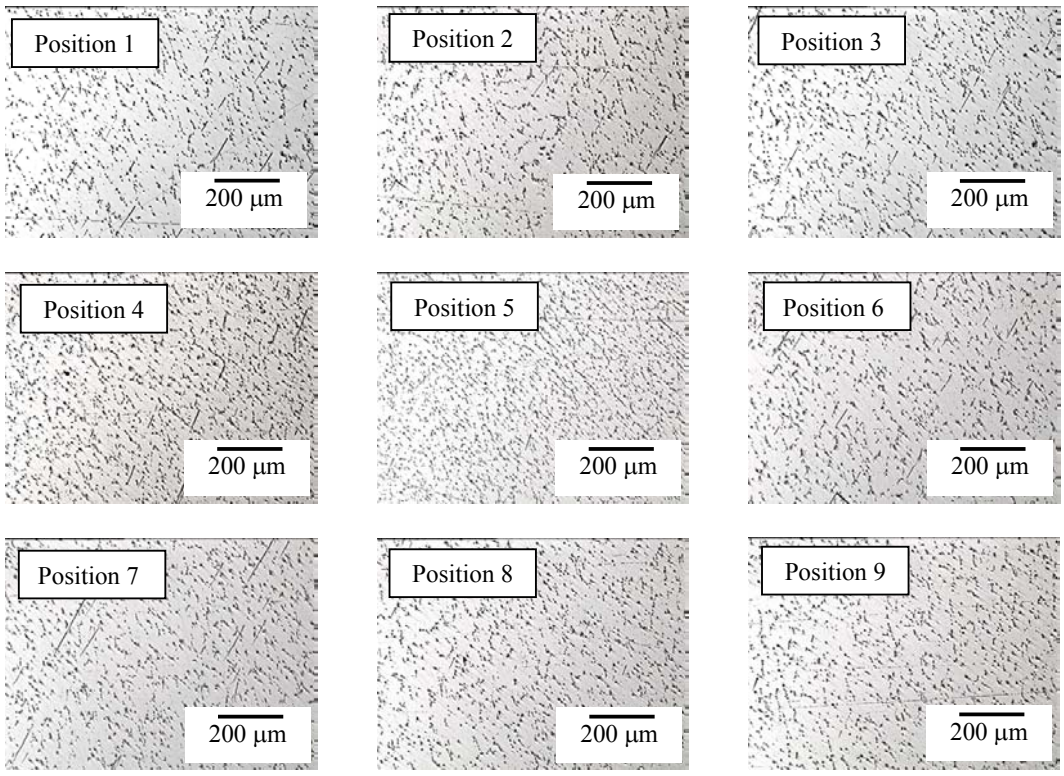

Figure 6.28 Optical micrograph of Al-1Mn-0.4Fe-0.3Si after 3 ECAE passes before annealing on positions indicated in Figure 6.26

6.2.3 Thermoelectric power (TEP) measurements

Thermoelectric power (TEP) measurements were used to determine the solute levels in the different samples. The TEP values measured for undeformed (as cast) and ECAE-deformed samples with and without subsequent annealing are shown in Figure 6.29. The main contribution to the observed changes in the TEP of the present alloy comes from the changes in the level of manganese in solid solution [46, 47, 195]. The approximate %Mn in solid solution is shown in Figure 6.30; this was calculated using values for specific resistivity and specific thermoelectric power as reported by Borrelly et al. [186]. Figure 6.30 shows that after ECAE processing, the amount of Mn in solid solution is unchanged. After annealing, the amount of Mn in solid solution is rapidly reduced by ECAE processing; there is a further small reduction with increasing numbers of ECAE passes.

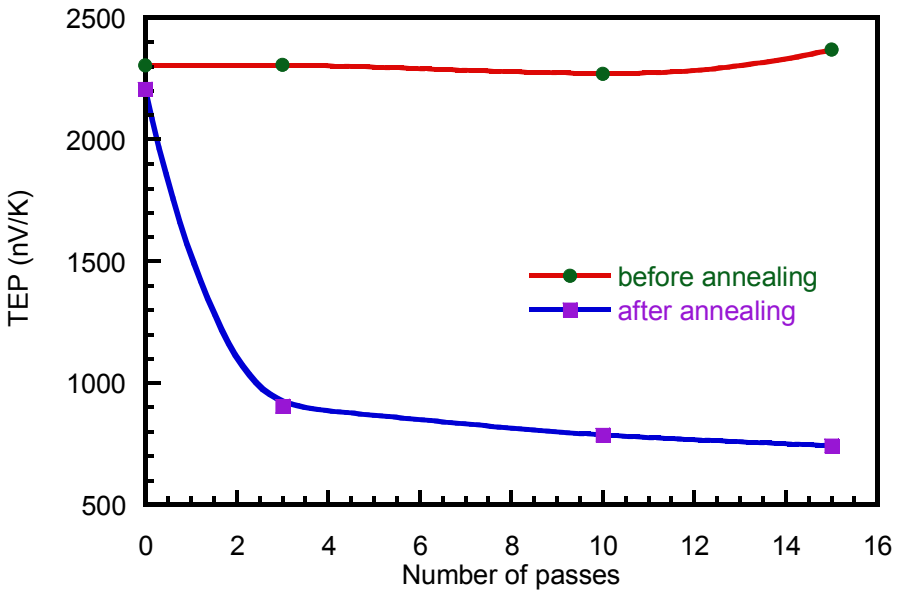

Figure 6.29 Relative TEP of the undeformed and ECAE-deformed Al-1Mn-0.4Fe-0.3Si alloy.

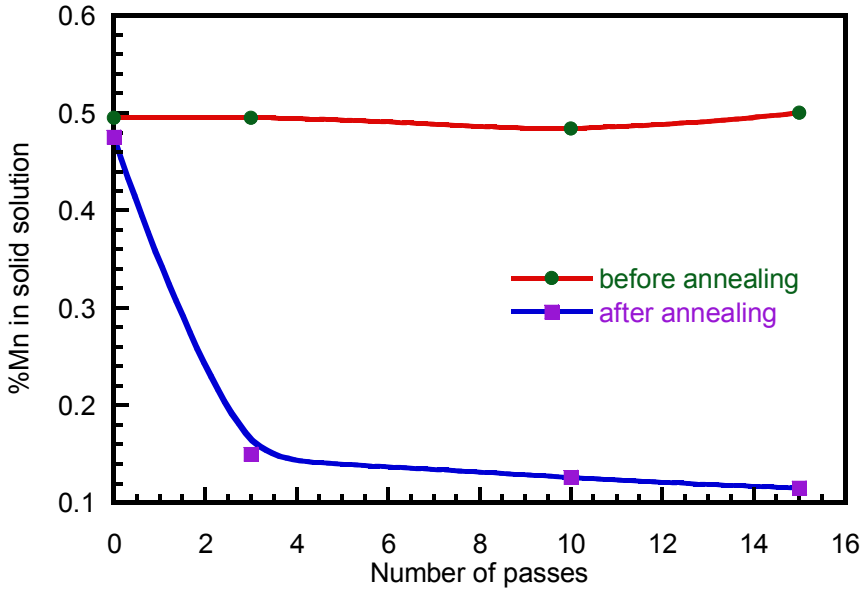

Figure 6.30 %Mn in solid solution of the undeformed and ECAE-deformed Al-1Mn-0.4Fe-0.3Si alloy.

6.2.4 Electrochemical study of the effect of ECAE processing

6.2.4.1 Potentiodynamic cathodic and anodic polarisations

The cathodic and anodic reactivity of the material with the different levels of ECAE-deformation and subsequent annealing were studied using potentiodynamic polarisation.

Figure 6.31 shows the cathodic polarisation for the alloy with the different levels of ECAE-deformation and subsequent annealing in naturally aerated 0.1 M NaCl. Figure 6.32 shows the cathodic current density (mA/cm^2) at a potential of –0.95 V(SCE) plotted from data in Figure 6.31. Figures 6.31 and 6.32 show that the undeformed and

annealed sample exhibits the lowest cathodic reactivity compared to the ECAE-deformed samples. Among samples with different numbers of ECAE passes and subsequent annealing, increasing the number of ECAE passes causes a further increase in the cathodic reactivity.

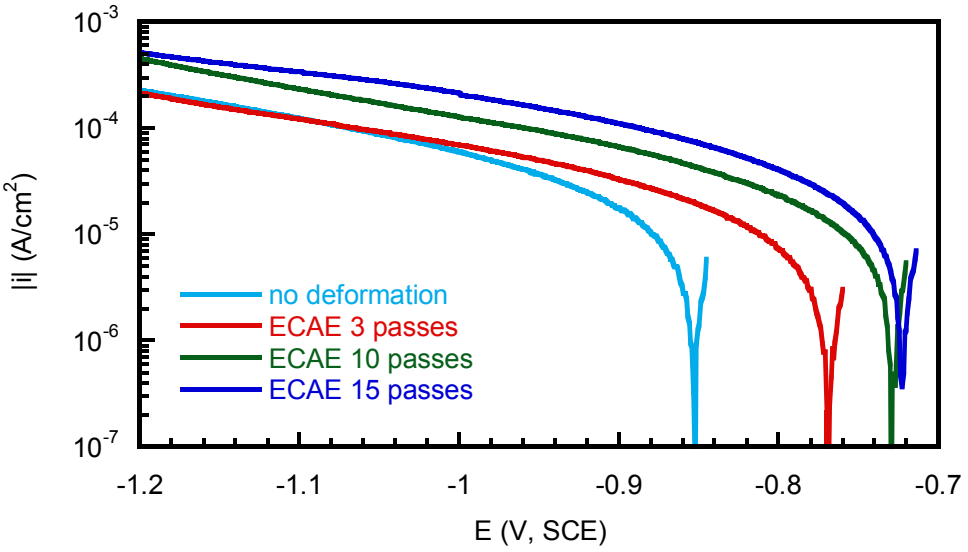

Figure 6.31 Cathodic polarisation of Al-1Mn-0.4Fe-0.3Si with different numbers of ECAE passes and subsequent annealing in naturally aerated 0.1 M NaCl.

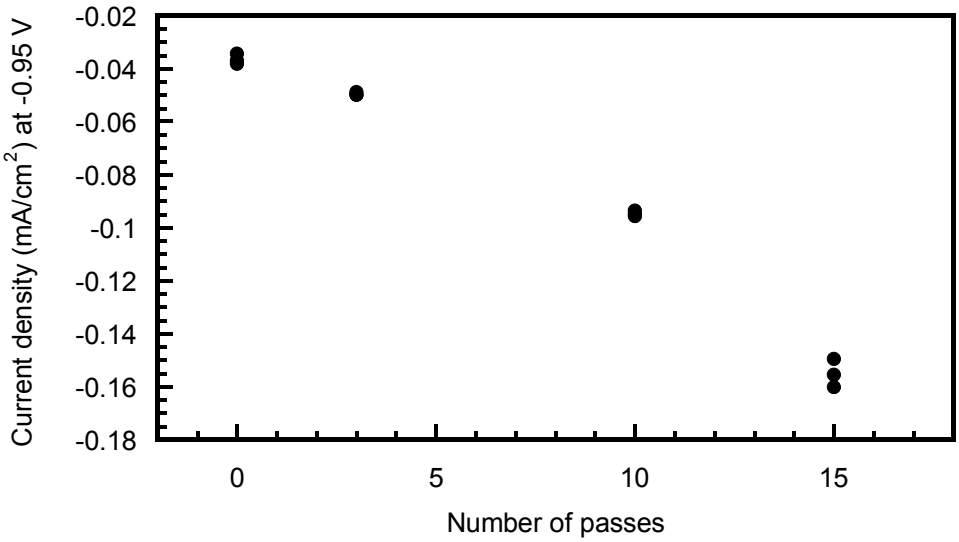

Figure 6.32 Cathodic current density (mA/cm^2) at -0.95 V(SCE) of Al-1Mn-0.4Fe-0.3Si with different numbers of ECAE passes and subsequent annealing in naturally aerated 0.1 M NaCl.

Figure 6.33 shows anodic polarisation curves for the alloy with the different levels of ECAE-deformation and subsequent annealing in de-aerated 0.1 M NaCl. Figure 6.34 shows the anodic potential (V, SCE) at a current density of 100 μA/cm^2 plotted from data in Figure 6.33. The anodic reactivity of the undeformed sample appears to show the highest reactivity, with a passive region as shown in Figure 6.33. After deformation, increasing the number of ECAE passes results in increase in anodic reactivity without a passive region.

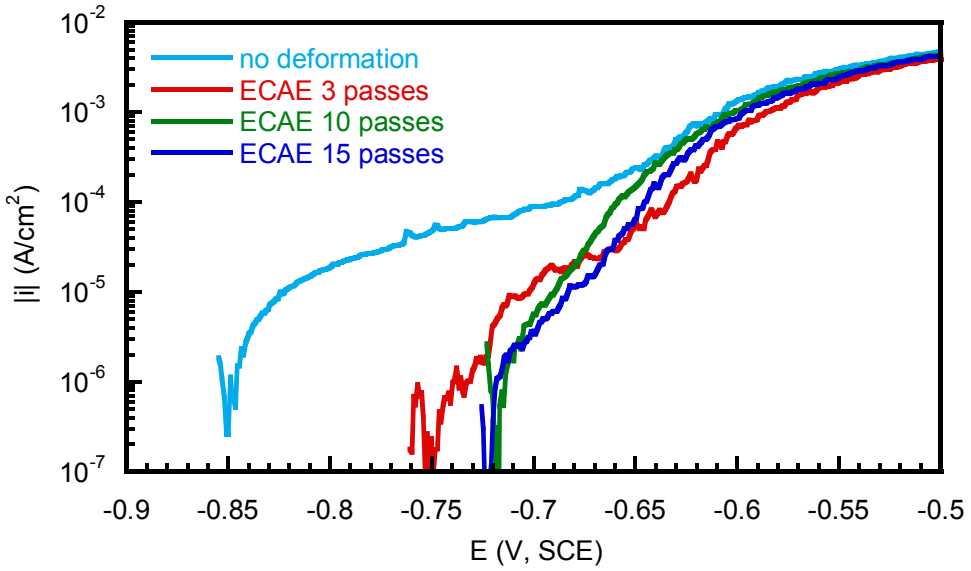

Figure 6.33 Anodic polarisation of Al-1Mn-0.4Fe-0.3Si with different numbers of ECAE passes and subsequent annealing in de-aerated 0.1 M NaCl.

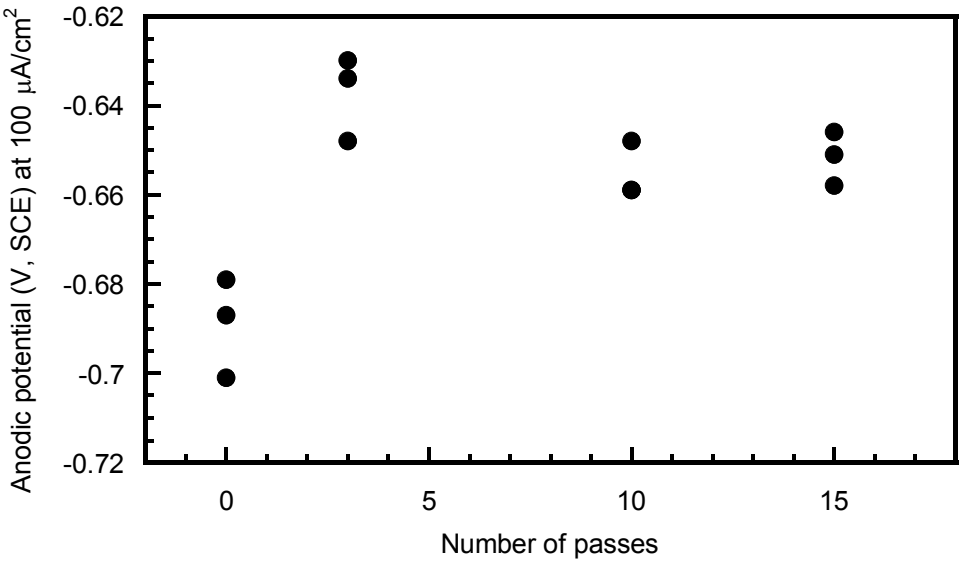

Figure 6.34 Anodic potential (V, SCE) at a current density of 100 µm/cm^2 of Al-1Mn-0.4Fe-0.3Si with different numbers of ECAE passes and subsequent annealing in de-aerated 0.1 M NaCl.

In situ anodic polarisation measurements were conducted in naturally aerated 0.1 M NaCl, pH 11.5, to investigate the anodic reactivity of the undeformed (as cast) and the extremely deformed (ECAE 15 passes) samples after annealing, with visual observation of the surface during the measurement. Figure 6.35 shows that the passive current density was slightly higher for the 15 ECAE passes, annealed sample and the breakdown potential was slightly lower. Thus, 15 ECAE passes and subsequently annealed sample was more anodically active than the undeformed and annealed sample.

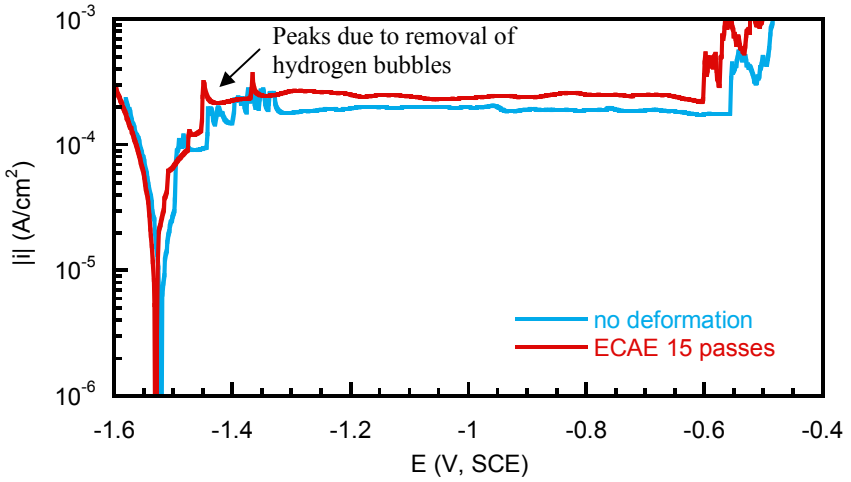

Figure 6.35 Anodic polarisation of the undeformed and deformed (ECAE 15 passes) annealed samples of Al-1Mn-0.4Fe-0.3Si in naturally aerated 0.1 M NaCl, pH 11.5.

Figures 6.36 and 6.37 show the anodic polarisation curve of the undeformed and deformed (15 ECAE passes) samples, respectively, with still images taken from the video recording during polarisation measurement. At the beginning of each measurement, hydrogen bubbles evolved across the surfaces of both samples. Then, the rate of evolution decreased as the potential become more anodic. However, there were some bubbles adhering to the surfaces. The solution was stirred to remove these bubbles, causing the peaks indicated. In the passive region, no changes were observed on the surfaces. At the breakdown potential, hydrogen bubbles were evolved rapidly at pit sites.

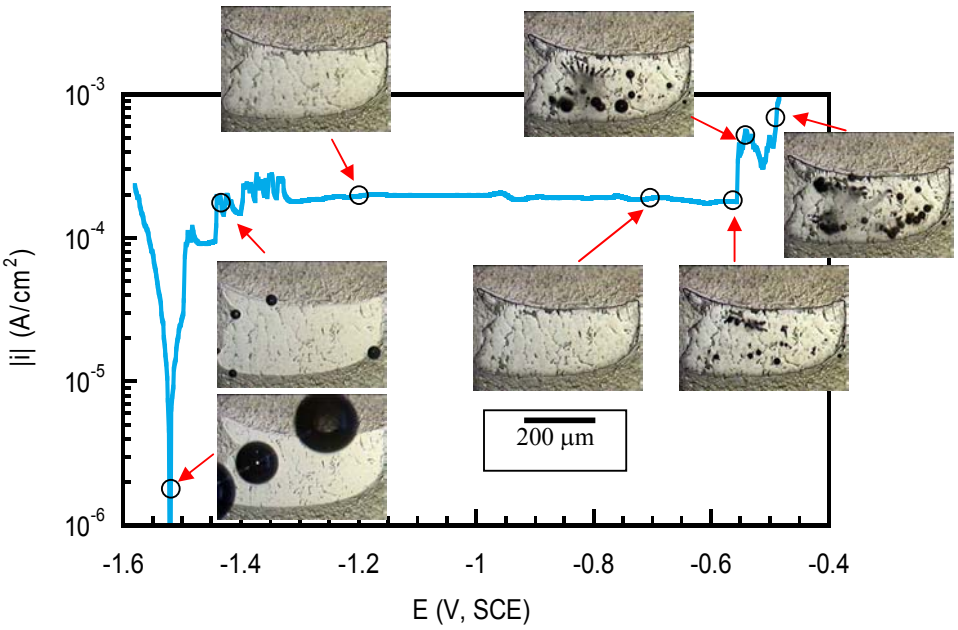

Figure 6.36 Anodic polarisation of the undeformed and annealed Al-1Mn-0.4Fe-0.3Si sample in naturally aerated 0.1 M NaCl, pH 11.5, with in situ video images taken during the polarisation measurement.

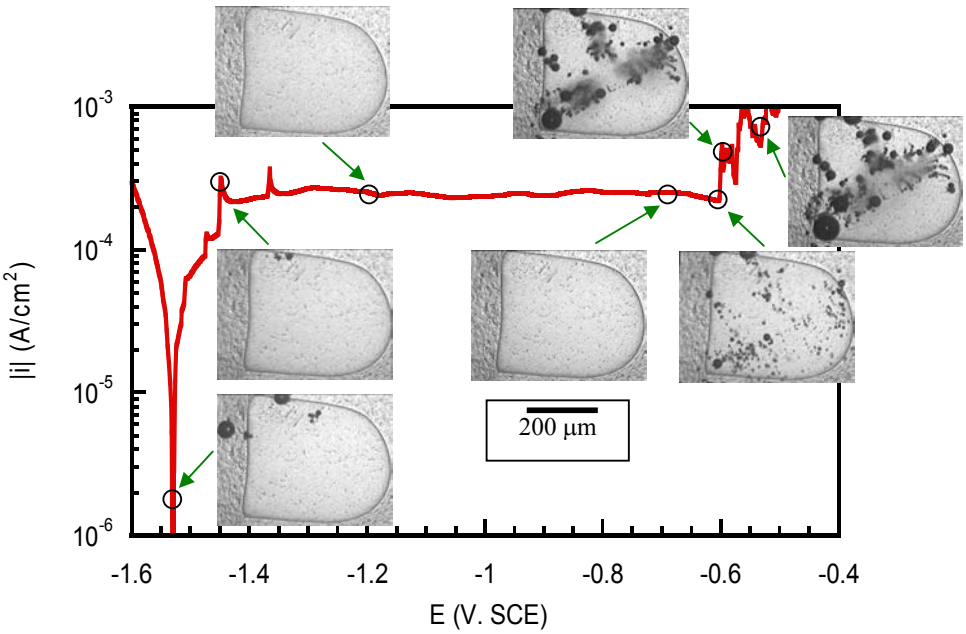

Figure 6.37 Anodic polarisation of the 15 ECAE passes and subsequently annealed Al-1Mn-0.4Fe-0.3Si sample in naturally aerated 0.1 M NaCl, pH 11.5, with in situ video images taken during the polarisation measurement.

6.2.4.3 Corrosion surface morphology

Figures 6.38(a)–(d) show the surface morphology of the corroded surfaces of the undeformed and deformed samples after anodic polarisation in de-aerated 0.1 M NaCl, stopped at a potential of –0.5 V(SCE). The images show that the localised corrosion sites are associated with intermetallic particles. The undeformed or as cast surface shows a large area of localised corrosion sites. The size of the pits is smaller on the deformed surfaces. Among the deformed surfaces, the 15 ECAE passes surface showed the smallest area of localised corrosion sites.

Figures 6.39(a)–(d) show the surface morphology of undeformed and deformed samples after cathodic polarisation in naturally aerated 0.1 M NaCl stopped at a potential -1.2 V(SCE). The images do not show any corrosion sites.

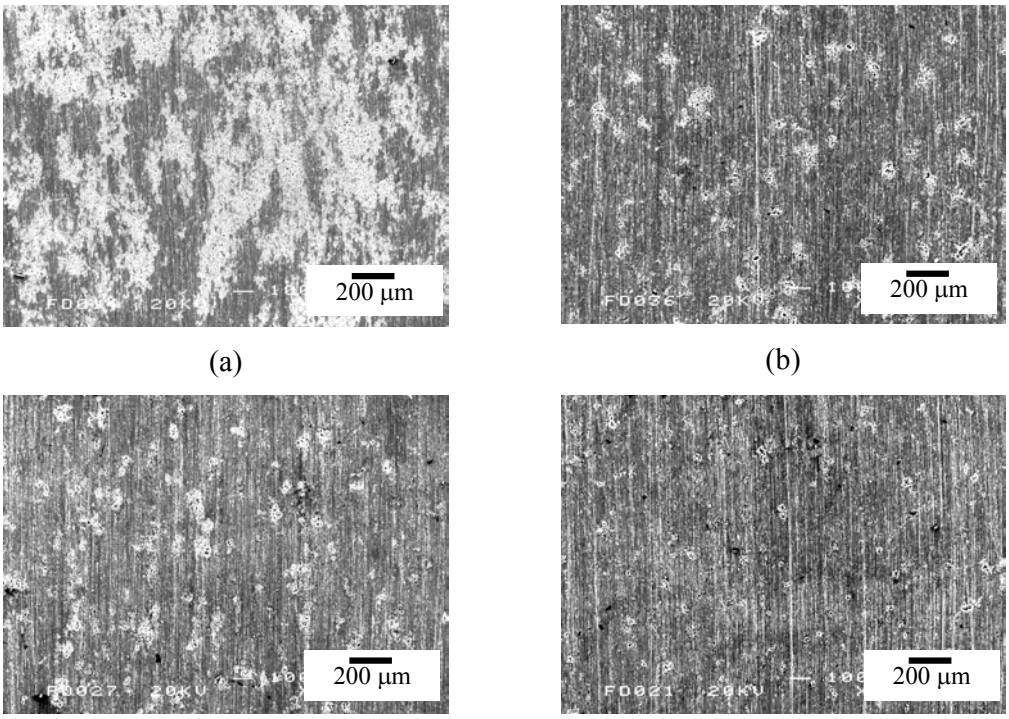

Figure 6.38 Morphology of the corroded surfaces of Al-1Mn-0.4Fe-0.3Si after anodic polarisation in de-aerated 0.1 M NaCl, with different levels of ECAE-deformation and subsequent annealing: (a) no deformation, (b) ECAE 3 passes, (c) ECAE 10 passes, and (d) ECAE 15 passes. Anodic polarisation was performed from the open circuit potential to -0.5 V(SCE) at a sweep rate of 1 mV/s.

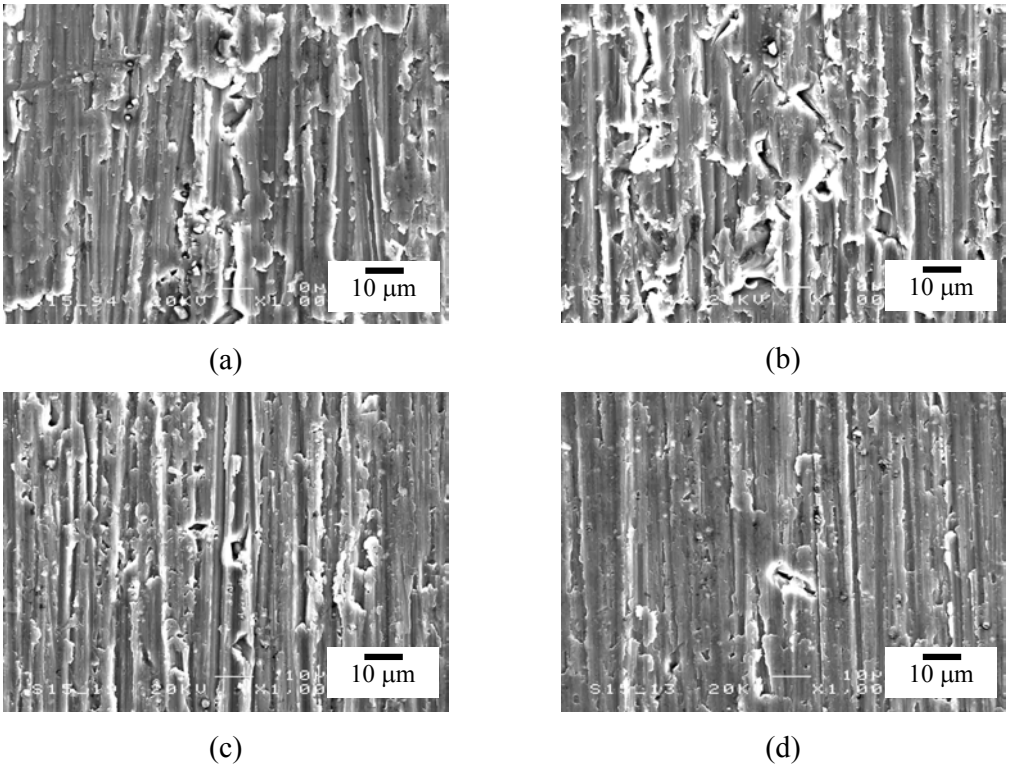

Figure 6.39 Morphology of the corroded surfaces of Al-1Mn-0.4Fe-0.3Si after cathodic polarisation in naturally aerated 0.1 M NaCl, with different levels of ECAE-deformation and subsequent annealing: (a) no deformation, (b) ECAE 3 passes, (c) ECAE 10 passes, and (d) ECAE 15 passes. Cathodic polarisation was performed from the open circuit potential to -1.2 V(SCE) at a sweep rate of 1 mV/s.

6.3 Discussion

Investigation of the effect of deformation and annealing on the electrochemical behaviour of an Al-1Mn-0.4Fe-0.3Si model alloy was carried out using uniaxial compression and equal channel angular extrusion (ECAE).

ECAE is a special deformation technique in which a billet is subjected to very high plastic strain without any change in the billet's shape [52, 55]. The multiple passes through the die results in an accumulated strain and subsequent annealing forming a submicron grain structure [59, 61-67]. Figure 6.19 shows the undeformed and subsequently annealed sample with a grain size between 1 and 2 mm. From Figures 6.20–6.22, it is clear that the grain sizes are greatly reduced due to ECAE processing and subsequent annealing. In increasing the number of ECAE passes, the grain size was significantly reduced. For example, after the specimen was extruded for 3 passes and subsequently annealed, the grain sizes were reduced to ~100–200 μm (Figure 6.20). After 10 ECAE passes and annealing, the grain sizes were reduced to ~50–100 μm as shown in Figure 6.21. In the case of 15 ECAE passes and annealing, the grain sizes were reduced to ~3–5 μm (Figure 6.22).

The microstructure from uniaxial compression is different to that from ECAE processing. Optical and EBSD micrographs (Figure 6.7 and 6.19–6.22) show that the undeformed and annealed sample has a large average grain size between 1 and 2 mm. For both uniaxial compression and ECAE processing, deformation followed by annealing

led to a decrease in grain size compared to as cast. Deformation by ECAE gave a much smaller grain size than deformation by uniaxial compression. For example, 80 % deformation by uniaxial compression and subsequent annealing gave an average grain size of ~200-400 μm, while 15 ECAE passes with the same annealing treatment gave an average grain size of ~3-5 μm.

The Vickers microhardness results for the unannealed samples shown in Figure 6.27. It shows that the hardness of the undeformed sample is significantly lower than that of the deformed samples. This is probably due to work hardening [196].

In this study, it is found that both deformation by uniaxial compression and ECAE followed by annealing leads to an increase in the number and area fraction of intermetallic particles (Figures 6.9, 6.23 and 6.24). This happens for two reasons. Firstly, intermetallic particles are fragmented, giving several smaller particles when the alloy is deformed. Secondly, a number of intermetallic particles nucleate and grow as a result of annealing. Enhanced deformation of aluminium alloys has an effect on precipitation kinetics. Luiggi [46-48] studied the effect of plastic deformation on the precipitation kinetic of AA 3003, which contains $Al_6(MnFe)$ and α-$Al_{12}(MnFe)_3Si$ intermetallic particles, using the thermoelectric power (TEP) technique. It was found that Mn diffusion is the dominant process in the precipitation kinetics. At an identical annealing temperature, a higher level of deformation significantly increases the rate of precipitation.

Both deformation by uniaxial compression and ECAE have effect on the electrochemical behaviour of Al-1Mn-0.4Fe-0.3Si alloy. It is found that both uniaxial compression deformed and ECAE deformed samples have a higher cathodic reactivity than the undeformed sample (Figures 6.10, 6.11, 6.31 and 6.32). Furthermore, the higher levels of deformation increased the cathodic reactivity resulting from the breakdown of intermetallic particles into smaller particles when deformed and precipitated more intermetallic particles on the surface after heat-treatment.

The deformation by uniaxial compression and ECAE also affects the anodic reactivity. It is found that the undeformed and annealed sample has lower anodic reactivity than the deformed and annealed samples (Figure 6.12, 6.13, and 6.33-6.35). The higher levels of deformation resulted in increased anodic reactivity. The surface morphology of the corroded surface after anodic polarisation show localised corrosion (pitting) sites on the surface. The number of pitting sites on the undeformed sample is less than that on the deformed samples (Figure 6.14 and 6.38). These are related to the number of intermetallic particles on the surface. It has been suggested that the increased precipitation on the deformed samples causes a decrease in solute content (Mn) of the matrix, thus enhancing the anodic reactivity. Approximate % Mn in solid solution (Figure 6.30) was calculated from the TEP values using specific resistivity and specific thermoelectric power values as reported by Borrelly et al. [186]. The higher number of ECAE passes result in the %Mn in solid solution decreasing. Intermetallic particles also act as preferential pit initiation sites. Thus, the higher density of intermetallic particles found on the samples increased with levels of deformation leads to a larger number of pits, as shown in Figure 6.14 and 6.38.

Both hot and cold rolling of aluminium alloys and many surface preparation procedures such as grinding, machining, dimpling, sand blasting, etc. generate the deformed layer at the surface [10, 21-24, 36, 50, 51]. This deformed layer has adverse effects on corrosion resistance such as filiform corrosion and pitting corrosion [9, 11, 13, 14, 23, 45, 50, 149-151].

Scamans et al. [50] investigated the correlation between the amount of surface deformation induced by various grinding practices and subsequent annealing on corrosion behaviour of hot rolled AA 3005. It was found that grinding of aluminium alloy surfaces produced ultra-fine grain sized, deformed surface layers with fine intermetallic particles resulting in promoted susceptibility to filiform corrsosion. Leggat and Taylor [153] studied the effect of micron-scale surface deformation on the corrosion behaviour of coil-coated AA 5182. They found that dimples were introduced into the coil-coated sheet by feed roller during can end manufacturing. As a result of micron-scale surface deformation, the damaged oxide film and second-phase precipitation were proposed as the mechanism of increased corrosion susceptibility. Forsyth [22] studied corrosion behaviour on machined surfaces of AA 7010 in seawater and found that the deformed material is more susceptible to corrosion than the undeformed substrate. Moreover, any bruising of the machined surface, such as that arising from chip build up and clogging, increased the corrosion susceptibility [21, 22].

6.4 Summary

The model alloy Al-1Mn-0.4Fe-0.3Si was deformed by uniaxial compression and equal channel angular extrusion (ECAE), and then annealed at 400°C for 2 h and furnace cooled. It was found that deformation by uniaxial compression and ECAE leads to an increase in the number of intermetallic particles and the total area of intermetallic particles correlates with the increase in cathodic reaction and increase in the number of pitting sites. Furthermore, the depletion of Mn in solid solution in the matrix contributes to the enhanced anodic reactivity.

This work has implications for filiform corrosion found on rolled aluminium alloys and corrosion of surfaces with other kinds of mechanical damage such as machining.

Chapter 7 Conclusions

This work has been based on the study of the effect of surface preparation and deformation on electrochemical behaviour of Al-Mn alloys. Al-1Mn-0.4Fe-0.3Si model alloy in the form of cold rolled sheet was used to investigate the effect of surface preparation and the as-cast billet form was used to investigate the effect of deformation. It was found that there is one main type of intermetallic particle: α–$Al_{12}(MnFe)_3Si$. The AA3005 alloy in the form of cold rolled sheet was used to investigate the role of the active deformed layer on electrochemical behaviour. It was found that there are two main types of intermetallic particles: $Al_6(MnFe)$ and α–$Al_{12}(MnFe)_3Si$. Both types of intermetallic particles were found to be more cathodically reactive than the matrix. The sections below are the conclusions of this work.

7.1 Surface preparation effects

Different surface preparations affect the electrochemical behaviour of cold-rolled Al-1.0Mn-0.4Fe-0.3Si. The surface roughness, chemical properties, and number of intermetallic particles on the surface are significant factors affecting the corrosion behaviour. In this study, it has been observed that pitting is always associated with intermetallic particles.

Mechanical grinding and polishing have an effect on the roughness of the surface. It was found that increased surface roughness causes increased anodic reactivity (high pit density). However, the roughness has little effect on cathodic reactivity.

Chemical properties also affect corrosion behaviour. Nitric acid treatment decreases the anodic reactivity but increases the cathodic reactivity. Alkaline etching and desmutting in concentrated nitric acid improved the electrochemical behaviour by decreasing pit density and anodic reactivity. However, it increases cathodic reactivity. The results presented here do not indicate whether the overall corrosion rate under freely corroding condition will increase or decrease. Further experiments (for example, electrochemical impedance or weight loss measurements) are required to determine this.

The GDOES sputtered surface with a depth of ~3.6 μm from the surface had lower pit density and lower anodic and cathodic reactivity compared to the as-received surface.

7.2 Deformation effects

7.2.1 Electrochemical behaviour of active surface layers in commercial cold rolled AA 3005 sheet

The electrochemical reactivity of the surface layers of commercial cold rolled and annealed AA 3005 sheet was investigated by profiling through the surface with GDOES.

The microstructure and electrochemical reactivity was examined at different depths in order to compare the behaviour of the surface layers with that of the bulk alloy.

It was found that the enhanced deformation at the surface of a rolled commercial AA 3005 alloy sheet resulted in an increased number of fine intermetallic particles after annealing. These were as a result of both fragmentation of existing particles and nucleation and growth of new precipitates. The surface layers of the alloy up to about 1 μm depth showed higher cathodic reactivity due to an increased number of $Al_6(MnFe)$ and α-$Al_{12}(MnFe)_3Si$ precipitates. Pit initiation was enhanced at the surface owing to the increased density of intermetallic particles and it is likely that solute depletion from the matrix, particularly of Mn, contributed to the enhanced anodic reactivity.

7.2.2 Investigation of the role of deformation by uniaxial compression and ECAE processing on electrochemical behaviour of Al-1Mn-0.4Fe-0.3Si

The model alloy Al-1Mn-0.4Fe-0.3Si was deformed by uniaxial compression and equal channel angular extrusion (ECAE), then annealed at 400°C for 2 h and furnace cooled. For both uniaxial compression and ECAE processing, deformation followed by annealing led to a decrease in grain size. Deformation by ECAE gave a much smaller grain size than deformation by uniaxial compression.

It was found that deformation leads to an increase in the number of intermetallic particles and total area correlates with cathodic reaction and increased number of pitting

sites. Furthermore, the depletion of Mn in solid solution which deduced from TEP contributes to the enhanced anodic reactivity.

Chapter 8 Future Work

This work has shown that deformation has an effect on corrosion susceptibility. It could be applied to some practical examples, e.g. the deformed layer developed on aluminium surface during manufacturing by machining and grinding in automotive car bodies, architectural applications, and friction stir welds. For example, AA 5182 has been used in the automotive industry. Manufacture would involve mechanical strain during pressing, machining and grinding operations which might result in the development of the deformed layer and susceptibility to filiform corrosion. Another example might be friction stir welding, which involves the joining of metals without fusion or filler materials. It is used for joining structural components made of aluminium and its alloys. The welds are created by the combined action of frictional heating and mechanical deformation due to a rotating tool which could produce a deformed layer. Future work could be done by simulation of different types of deformed layer and then studying the effect of different types of deformed layer on electrochemical behaviour. Furthermore, the work presented here could be extended to study in more detail the relationship between the solid solution depletion and anodic reactivity. In addition, the effect of the distribution of intermetallic particles on the cathodic reactivity could be studied.

This work has explained why the deformed layer on cold rolled sheet of aluminium alloys affects corrosion susceptibility. This leads to the recommendation to remove this deformed layer to prevent corrosion. This can be achieved by deep chemical

etching, for example in highly alkaline solutions, as part of surface finishing procedures. It is therefore important to monitor the amount of metal removed during surface finishing to ensure that the deformed layer is completely removed.

REFERENCES

1 S. H. Avner, *Introduction to Physical Metallurgy*, p. 481-489, McGraw-Hill, Japan, (1974).

2 I. J. Polmear, *Light Alloys: Metallurgy of the Light Metals*, p. 24-27, 90-91, and 103-104, St Edmundsbury Press Ltd., Bristol, UK, (1995).

3 R. W. Cahn, P. Haasen, and E. J. Kramer, *Materials Science and Technology: A Comprehensive Treatment*, p. 242-244 and 267-273, **8**, VCH, Germany, (1996).

4 L. F. Mondolfo, *Manganese in Aluminium Alloys*, Manganese Centre, Neuilly sur Seine, France, (1977).

5 B. D. Craig, *Handbook of Corrosion Data*, p. 17, ASM International, Metals Park, USA, (1960).

6 W. D. Callister, *Materials Science and Engineering: An Introduction*, p. 372, John Wiley & Sons, Inc., USA, (1999).

7 A. K. Vasudevan and R. D. Doherty, *Aluminum Alloys-Contemporary Research and Applications*, p. 76-83, 137-167, Treatise on Materials Science and Technology, **31**, H. Herman Editor. Academic Press, Inc., USA., (1989).

8 R. G. Kamat and S. Saimoto, in *Proceedings of The 3rd International Conference on ALUMINIUM ALLOYS (ICAA3): Their physical and mechanical properties*, Trondheim, Norway, **3**, p. 291-296, (1992).

9 H. Leth-Olsen, J. H. Nordlien, and K. Nisancioglu, *Corrosion Science,* **40**, 2051-2063 (1998).

10 M. Fishkis and J. C. Lin, *Wear,* **206**, 156-170 (1997).

11 R. Ambat, A. J. Davenport, A. Afseth, and G. Scamans, *Journal of the Electrochemical Society,* **151**, B53-B58 (2004).

12 G. Plassart, M. Aucouturier, and R. Penelle, *Scripta materialia,* **41**, 1103-1108 (1999).

13 A. Afseth, J. H. Nordlien, G. M. Scamans, and K. Nisancioglu, *Corrosion Science,* **44**, 2491-2506 (2002).

14 A. Afseth, J. H. Nordlien, G. M. Scamans, and K. Nisancioglu, *Corrosion Science,* **43**, 2093-2109 (2001).

15 K. Nisancioglu, in *Proceedings of 3rd International Conference on Aluminium Alloys*, Trondheim, Norway, L. Arnberg, O. Lohne, E. Nes, and N. Ryum, Editors, **3**, p. 239-259, (1992).

16 K. Nisancioglu, *Journal of the Electrochemical Society,* **137**, 69-77 (1990).

17 M. Zamin, *Corrosion,* **37**, 627-632 (1981).

18 A. Afseth, J. H. Nordlien, G. M. Scamans, and K. Nisancioglu, *Corrosion Science,* **43**, 2359-2377 (2001).

19 K. Nisancioglu, K. Y. Davanger, and O. Strandmyr, *Journal of the Electrochemical Society,* **128**, 1523-1526 (1981).

20 H. Leth-Olsen, J. H. Nordlien, and K. Nisancioglu, *Journal of the Electrochemical Society,* **144**, L196-L197 (1997).

21 P. J. E. Forsyth, *Materials Science and Technology,* **11**, 1025-1033 (1995).

22 P. J. E. Forsyth, *Materials Science and Technology,* **14**, 151-160 (1998).

23 X. Zhou, G. E. Thompson, and G. M. Scamans, *Corrosion Science,* **45**, 1767-1777 (2003).

24 G. W. Critchlow and D. M. Brewis, *Int. J. Adehesion and Adhesives,* **16**, 255-275 (1996).

25 Y. L. Liu, Y. Liu, G. Liao, and J. G. Morris, *Aluminium Transactions,* **2**, 97-106 (2000).

26 S. Ding and J. G. Morris, *Metallurgical and Materials Transactions A,* **28A**, 2715-2721 (1997).

27 X. M. Cheng, Y. Liu, and J. G. Morris, *Aluminum Transactions,* 103-108 (2000).

28 *International Alloy Designations and Chemical Composition Limits for Wrought Aluminum and Wrought Aluminum Alloys*, p. 3-4 and 17, The Aluminum Association, USA, (1998).

29 *The Properties of Aluminium and its Alloys*, p. 8, 20-21 and 84, Aluminium Federation Ltd., UK, (1998).

30 H. H. Uhlig, *Corrosion and Corrosion Control: an introduction to corrosion science and engineering*, p. 295-306, John Wiley & Sons, Inc., USA, (1967).

31 N. Krendelsberger, F. Weitzer, and J. C. Schuster, *Metallurgical and Materials Transactions A,* **33A**, 3311-3319 (2002).

32 J. L. Murray, A. J. McAlister, R. J. Schaefer, L. A. Bendersky, F. S. Biancaniello, and D. L. Moffat, *Metallurgical Transactions A,* **18A**, 385-390 (1987).

33 W. T. Denholm, J. D. Esdaile, N. G. Siviour, and B. W. Wilson, *Metallurgical Transactions A,* **18A**, 393-397 (1987).

34 N. C. W. Kuijpers, J. Tirel, D. N. Hanlon, and S. van der Zwaag, *Journal of Materials Science Letters,* **22**, 1385-1387 (2003).

35 N. C. W. Kuijpers, W. H. Kool, P. T. G. Koenis, K. E. Nilson, I. Todd, and S. van der Zwaag, *Materials Characterization,* **49**, 409-420 (2003).

36 R. G. Kamat and S. Saimoto, *Materials Science and Technology,* **10**, 215-221 (1994).

37 T. Z. Kattamis, H. D. Merchant, S. Skolianos, and G. Scharf, *Aluminium,* **65**, 367-376 (1989).

38 H. D. Merchant, J. G. Morris, and D. S. Hodgson, *Materials Characterization,* **25**, 339-373 (1990).

39 E. V. Koroleva, G. E. Thompson, G. Hollrigl, and M. Bloeck, *Corrosion Science,* **41**, 1475-1495 (1999).

40 D. T. L. Alexander and A. L. Greer, *Acta Materialia,* **50**, 2571-2583 (2002).

41 D. L. Sun, S. B. Kang, and H.S.Koo, *Materials Chemistry and Physics,* **63**, 37-43 (2000).

42 Z. Li, X. Li, and J. G. Morris, in *Aluminum Alloys for Packaging*, Materials Week '92 in Chicago, Illinois, J. G. Morris, H. D. Merchant, E. J. Westerman, and P. L. Morris, Editors, p. 61-69, The Minerals, Metal & Materials Society (TMS), (1992).

43 H. Scott Goodrich, in *Aluminum Alloys for Packaging*, Materials Week '92 in Chicago, Illinois, J. G. Morris, H. D. Merchant, E. J. Westerman, and P. L. Morris, Editors, p. 47-60, The Minerals, Metals & Materials Society (TMS), (1992).

44 L. F. Mondolfo, *Aluminum Alloys: Structure and Properties*, Butterworth & Co (Publishers) Ltd, London, UK, (1976).

45 A. Afseth, J. H. Nordlien, G. M. Scamans, and K. Nisancioglu, *Corrosion Science,* **44**, 2543-2559 (2002).

46 N. J. Luiggi, *Metallurgical and Materials Transactions B,* **28B**, 125-133 (1997).

47 N. J. Luiggi, *Z. Metallkd.,* **88**, 274-277 (1997).

48 N. J. Luiggi, *Metallurgical and Materials Transactions B,* **28B**, 149-159 (1997).

49 O. N. Senkov, F. H. Fores, V. V. Stolyarov, R. Z. Valiev, and J. Liu, *NanoStructured Materials,* **10**, 691-698 (1998).

50 G. M. Scamans, A. Afseth, G. E. Thompson, and X. Zhou, in *Aluminium Surface Science and Technology (ASST 2003) Proceedings*, Bonn, Germany, H. Terryn, Editor. **43 - n 1-2 - 2003**, p. 90-94, (2003).

51 B. A. Parker, G. Wilson, and L. Chok, in *Aluminium Alloys Their Physical and Mechanical Properties,* E. A. Starke and T. H. Sanders, Editors, **1,** p. 545-469, EMAS, U.K., (1986).

52 V. M. Segal, *Plastic Deformation of Crystalline Materials,* in *United State Patent*p. 1-6, USA, (1996).

53 W. H. Huang, L. Chang, P. W. Kao, and C. P. Chang, *Materials Science and Engineering A,* **307**, 113-118 (2001).

54 Y.-L. Yang and S. Lee, *Journal of Materials Processing Technology,* **140**, 583-587 (2003).

55 V. M. Segal, *Materials Science and Engineering A,* **197**, 157-164 (1995).

56 Y. Iwahashi, J. Wang, Z. Horita, M. Nemoto, and T. G. Langdon, *Scripta materialia,* **35**, 143-146 (1996).

57 J. R. Bowen, A. Gholinia, S. M. Roberts, and P. B. Prangnell, *Materials Science and Engineering A,* **287**, 87-99 (2000).

58 S. J. Oh and S. B. Kang, *Materials Science and Engineering A,* **343**, 107-115 (2003).

59 Y. Iwahashi, Z. Horita, M. Nemoto, and T. G. Langdon, *Acta Materialia,* **46**, 3317-3331 (1998).

60 M. Furukawa, Y. Iwahashi, Z. Horita, M. Nemoto, and T. G. Langdon, *Materials Science and Engineering A,* **257**, 328-332 (1998).

61 Y. Iwahashi, Z. Horita, M. Nemoto, and T. G. Langdon, *Acta Materialia,* **45**, 4733 (1997).

62 Y. Iwahashi, M. Furukawa, Z. Horita, M. Nemoto, and T. G. Langdon, *Metallurgical and Materials Transactions A,* **29A**, 2245 (1998).

63 K. Nakashima, Z. Horita, M. Nemoto, and T. G. Langdon, *Materials Science and Engineering A,* **281**, 82-87 (2000).

64 M. Furukawa, Z. Horita, M. Nemoto, and T. G. Langdon, *Journal of Materials Science,* **36**, 2835 (2001).

65 U. Chakkingal and P. E. Thomson, *Journal of Materials Processing Technology,* **117**, 169-177 (2001).

66 J.-Y. Chang, J.-S. Yoon, and G.-H. Kim, *Scripta materialia,* **45**, 347 (2001).

67 A. Gholinia, P. B. Prangnell, and M. V. Markushev, *Acta Materialia,* **48**, 1115-1130 (2000).

68 V. V. Stolyarov and R. Lapovok, *Materials Science Forum,* **426-432**, 2825-2830 (2003).

69 *Metal Handbook*, p. 104-114, 583-589, **13**, ASM International, Metals Park, USA,, (1987).

70 M. Pourbaix, *Atlas of Electrochemical Equilibria in Aqueous Solution*, National Association of Corrosion Engineers, Houston, Texas, USA, (1974).

71 E. A. Starke and T. H. Sanders, *Aluminium Alloys: Their Physical and Mechanical Properties*, p. 1576-1592, **3**, Engineering Materials Advisory Service LTD., Warley, UK, (1986).

72 G. E. Thompson and G. C. Wood, *Anodic Films on Aluminium*, p. 229, London Academic Press, London, (1983).

73 A. Kolics, A. S. Besing, P. Baradlai, R. Haasch, and A. Wieckowski, *Journal of the Electrochemical Society,* **148**, B251-B259 (2001).

74 R. W. Elkington, *Aluminium Industry,* **41**, 19-28 (1986).

75 P. Gimenez, J. J. Rameau, and M. C. Reboul, *Corrosion,* **37**, 673-680 (1981).

76 M. Pourbaix, *Lectures on Electrochemical Corrosion*, Plenum Press, New York, (1973).

77 R. Ambat and E. S. Dwarakadasa, *Journal of Applied Electrochemistry,* **24**, 911-916 (1994).

78 J. O. Park, C.-H. Paik, Y. H. Huang, and R. C. Alkire, *Journal of the Electrochemical Society,* **146**, 517-523 (1999).

79 O. Seri and M. Imaizumi, *Corrosion Science,* **30**, 1124-1133 (1990).

80 T. Suter and R. C. Alkire, *Journal of the Electrochemical Society,* **148**, B36-B42 (2001).

81 R. M. Rynders, C.-H. Paik, R. Ke, and R. C. Alkire, *Journal of the Electrochemical Society,* **141**, 1439-1445 (1994).

82 C.-M. Liao and R. P. Wei, *Electrochimica Acta,* **45**, 881-888 (1999).

83 V. Guillaumin and G. Mankowski, *Corrosion Science,* **42**, 105-125 (2000).

84 O. Seri and K. Furumata, *Materials and Corrosion,* **53**, 1111-120 (2002).

85 M. Verhoff and R. Alkire, *Journal of the Electrochemical Society,* **147**, 1349-1358 (2000).

86 G. S. Frankel, *Corrosion Science,* **30**, 1203-1218 (1990).

87 A. J. Davenport, *Corrosion course*, (2003).

88 D. W. Buzza and R. Alkire, *Journal of the Electrochemical Society,* **142**, 1104-1111 (1995).

89 N. J. Laycock and R. C. Newman, *Corrosion Science,* **39**, 1771-1790 (1997).

90 P. C. Pistorius and G. T. Burstein, *Philosphical Transaction of the Royal Society London Series A-Mathematical Physical and Engineering Sciences,* **341 A**, 531-559 (1992).

91 G. S. Frankel, L. Stockert, F. Hunkeler, and H. Boehni, *Corrosion,* **43**, 429-438 (1987).

92 E. Ernst, N. J. Laycock, M. H. Moayed, and R. C. Newman, *Corrosion Science,* **39**, 1133-1136 (1997).

93 P. C. Pistorius and G. T. Burstein, in *4th International Symposium on Electrochemical Method in Corrosion Research*, Espoo, Finland, **111**, p. 429-452, Material Science Forum, (1991).

94 J. R. Galvele, *Journal of the Electrochemical Society,* **123**, 464-474 (1976).

95 S. T. Pride, J. R. Scully, and J. L. Hudson, *Journal of the Electrochemical Society,* **141**, 3028-3040 (1994).

96 T. R. Beck and R. C. Alkire, *Journal of the Electrochemical Society,* **126**, 1662-1666 (1979).

97 R. C. Newman, M. A. A. Ajjawi, H. Ezuber, and S. Turgoose, *Corrosion Science,* **28**, 471-477 (1988).

98 T. H. Nguyen and R. T. Foley, *Journal of the Electrochemical Society,* **127**, 2563-2566 (1980).

99 T. E. Graedel, *Journal of the Electrochemical Society,* **136**, 204C-212C (1989).

100 K. P. Wong and R. C. Alkire, *Journal of the Electrochemical Society,* **137**, 3010-3015 (1990).

101 R. Alkire and M. Feldman, *Journal of the Electrochemical Society,* **135**, 1850-1851 (1988).

102 T. Beck, *Electrochimica Acta,* **19**, 485 (1984).

103 R. C. Newman, *Corrosion Science,* **37**, 527-533 (1995).

104 R. P. Wei, *Scripta materialia,* **44**, 2647-2652 (2001).

105 D. G. Harlow and R. P. Wei, *Engineering Fracture Mechanics,* **59**, 305-325 (1998).

106 G. S. Chen, M. Gao, and R. P. Wei, *Corrosion,* **52**, 8-15 (1996).

107 G. S. Chen, K.-C. Wan, M. Gao, R. P. Wei, and T. H. Flournoy, *Materials Science and Engineering A,* **219**, 126-132 (1996).

108 C.-M. Liao, J. M. Olive, M. Gao, and R. P. Wei, *Corrosion,* **54**, 451-458 (1998).

109 M. Gao, C. R. Feng, and R. P. Wei, *Metallurgical and Materials Transactions A,* **29**, 1145 (1998).

110 C.-M. Liao, G. S. Chen, and R. P. Wei, *Scripta materialia,* **35**, 1341-1346 (1996).

111 F. Hunkeler and H. Bohni, *Corrosion,* **37**, 645-650 (1981).

112 S.-I. Pyun, K.-H. Na, W.-J. Lee, and J.-J. Park, *Corrosion,* **56**, 1015-1021 (2000).

113 E.-J. Lee and S.-I. Pyun, *Corrosion Science,* **37**, 157-168 (1995).

114 L. Stockert, F. Hunkeler, and H. Boehni, *Corrosion,* **41**, 676 (1985).

115 B. W. Davis, P. J. Moran, and P. M. Natishan, *Corrosion Science,* **42**, 2187-2192 (2000).

116 T. T. Lunt, S. T. Pride, J. R. Scully, and J. L. Hudson, *Journal of the Electrochemical Society,* **144**, 1620-1629 (1997).

117 G. S. Frankel, *Journal of the Electrochemical Society,* **145**, 2186-2198 (1998).

118 C. Y. Chao, L. F. Lin, and D. D. Macdonald, *Journal of the Electrochemical Society,* **128**, 1187-1194 (1981).

119 L. F. Lin, C. Y. Chao, and D. D. Macdonald, *Journal of the Electrochemical Society,* **128**, 1194-1198 (1981).

120 E. McCafferty, *Corrosion Science,* **37**, 481-492 (1995).

121 E. McCafferty, *Corrosion Science,* **45**, 1421-1438 (2003).

122 Z. Szklarska-Smialowska, *Corrosion Science,* **44**, 1143-1149 (2002).

123 H.-H. Strehblow, in *Corrosion Mechanisms in Theory and Practice,* P. Marcus and J. Oudar, Editors, Marcel Dekker Inc., New York, (1995).

124 O. Lunder and K. Nisancioglu, *Corrosion Science,* **24**, 965-975 (1984).

125 A. Barbucci, G. Bruzzone, M. Delucchi, M. Panizza, and G. Cerisola, *Intermetallics,* **8**, 305-312 (2000).

126 O. Seri, *Corrosion Science,* **36**, 1789-1803 (1994).

127 K. Nisancioglu, in *Proceedings of RASELM' 91, the Conference on Science and Engineering of Light Metals*, Sendai, Japan, p. 359-363, (1991).

128 A. Aballe, M. Bethencourt, F. J. Botana, M. J. Cano, and M. Marcos, *Corrosion Science,* **45**, 161-180 (2003).

129 M. Büchler, T. Watari, and W. H. Smyrl, *Corrosion Science,* **42**, 1661-1668 (2000).

130 J. Y. Josefowicz, J. J. DeLuccia, V. S. Agarwala, and G. C. Farrington, *Materials Characterization,* **34**, 73-79 (1995).

131 R. Buchheit, *Journal of the Electrochemical Society,* **142**, 3994-3996 (1995).

132 T. D. Burleigh, R. C. Rennick, and F. S. Bovard, *Corrosion,* **49**, 683-685 (1993).

133 *Aluminum*, p. 212, Properties, Physical Metallurgy and Phase Diagrams, **1**, K. R. Van Horn Editor. ASM, Ohio, (1971).

134 *Aluminium heat exchanger materials*, Corus, (2001).

135 M. Büchler, J. Kerimo, F. Guillaume, and W. H. Smyrl, *Journal of the Electrochemical Society,* **147**, 3691-3699 (2000).

136 T. P. Moffat, G. R. Stafford, and D. E. Hall, *Journal of the Electrochemical Society,* **140**, 2779-2786 (1993).

137 T. Ramgopal and G. S. Frankel, *Corrosion,* **57**, 702-711 (2001).

138 G. S. Frankel, R. C. Newman, C. V. Jahnes, and M. A. Russak, *Journal of the Electrochemical Society,* **140**, 2192-2197 (1993).

139 G. S. Frankel, M. A. Russak, C. V. Jahnes, M. Mirzamaani, and V. A. Brusic, *Journal of the Electrochemical Society,* **136**, 1243-1244 (1989).

140 P. M. Natishan, E. McCafferty, and G. K. Hubler, *Journal of the Electrochemical Society,* **135**, 321-327 (1988).

141 W. C. Moshier, B. W. Davis, J. S. Ahearn, and H. F. Hough, *Journal of the Electrochemical Society,* **134**, 2677-2684 (1987).

142 B. A. Shaw, G. D. Davis, T. L. Fritz, B. J. Rees, and W. C. Moshier, *Journal of the Electrochemical Society,* **138**, 3288-3295 (1991).

143 G. D. Davis, W. C. Moshier, T. L. Fritz, and G. O. Cote, *Journal of the Electrochemical Society,* **137**, 422-427 (1990).

144 M. Yasuda, F. Weinberg, and D. Tromans, *Journal of the Electrochemical Society,* **137**, 3708-3715 (1990).

145 W. C. Moshier, G. D. Davis, and G. O. Cote, *Journal of the Electrochemical Society,* **136**, 356-362 (1989).

146 E. L. Principe, B. A. Shaw, and G. D. Davis, *Corrosion,* **59**, 295-313 (2003).

147 A. Afseth, J. H. Nordlien, G. M. Scamans, and K. Nisancioglu, *Corrosion Science,* **44**, 145-162 (2002).

148 K. Nisancioglu, *A Priliminary Assesment of the Corrosion Resistance of a New AlMn Alloy with a High Manganese Content*, STF34 F38011, SINTEF, (1983).

149 H. Leth-Olsen and K. Nisancioglu, *Corrosion Science,* **40**, 1179-1194 (1998).

150 H. Leth-Olsen, A. Afseth, and K. Nisancioglu, *Corrosion Science,* **40**, 1195-1214 (1998).

151 J. H. Nordlien, A. J. Davenport, and G. M. Scamans, in *Proc. 2nd Int. Symp. Aluminium Surface Science and Technology*, UMIST, Manchester, UK, p. 107-112, (2000).

152 R. Ambat, J. Namahoot, G. M. Scamans, A. Afseth, and A. J. Davenport, in *Aluminium Surface Science and Technology (ASST 2003) Proceedings*, Bonn, Germany, H. Terryn, Editor. p. 396-401, (2003).

153 R. B. Leggat and S. R. Taylor, *Corrosion,* **55**, 984-990 (1999).

154 M. van Loo, D. D. Laiderman, and C. R.R. Bruhn, *Corrosion,* **9**, 277–283 (1953).

155 G. M. Hoch, *Corrosion,* **3**, 134–141 (1974).

156 C. Sharman, *Nature,* **153**, 621 (1944).

157 G. M. Scamans, M. P. Amor, B. R. Ellard, and J. A. Hunter, in *Proceedings International Symposium on Aluminium Surface Science and Technology*, Antwerp, p. 229, (1997).

158 A. Bautista, *Progress in Organic Coatings,* **28**, 49–58 (1996).

159 *Finishing,* 19–22 (1994).

160 Z. Marsh, J. Marsh, and J. D. Scantlebury, *The Journal of Corrosion Science and Engineering,* **2**, 1-7 (1999).

161 G. Grundmeier, W. Schmidt, and M. Stratmann, *Electrochimica Acta,* **45**, 2515-2533 (2000).

162 G. Williams, H. N. McMurray, D. Hayman, and P. C. Morgan, *Phys. Chem. Comm.,* **6**, 1-9 (2001).

163 R. T. Ruggeri and T. R. Beck, *Corrosion,* **39**, 452-465 (1983).

164 J. L. Delplancke, S. Berger, X. Lefèbvre, D. Maetens, A. Pourbaix, and N. Heymans, *Progress in Organic Coatings,* **43**, 64-74 (2001).

165 R. Szymanski, D. N. Jamieson, A. E. Hughes, A. Mol, S. v. d. Zwaag, and C. G. Ryan, *Nuclear Instruments and Methods in Physics Research,* **B 190**, 365–369 (2002).

166 J. Weissenrieder, C. Leygraf, M.Göthelid, and U. O. Karlsson, *Appiled Surface Science,* **218**, 154-161 (2003).

167 W. H. Slabaugh, W. Dejager, S. E. Hoover, and L. L. Hutchinson, *Journal of Paint Technology,* **44**, 76–83 (1972).

168 J. H. W. de Wit, *Electrochimica Acta,* **46**, 3641-3650 (2001).

169 R. J. Higginson, M. Aindow, and P. S. Bate, *Materials Science and Engineering A,* **225**, 9-21 (1997).

170 H. Leth-Olsen and K. Nisancioglu, *Corrosion,* **53**, 705-717 (1997).

171 W. Schmidt and M. Stratmann, *Corrosion Science,* **40**, 1141-1143 (1998).

172 M. H. M. Huisert, J. D. B. Sharman, H. W. Van Rooijen, E. P. M. Van Westing, J. H. W. de Wit, and L. Katgerman, in *Proc. 2nd Int. Symp. Aluminium Surface Science and Technology*, UMIST, Manchester, UK, p. 461-466, (2000).

173 G. M. Scamans, *Unpublished results*, Alcan International, (2001).

174 A. Afseth, J. H. Nordlien, G. M. Scamans, and K. Nisancioglu, *Corrosion Science,* **44**, 2529-2542 (2002).

175 P. G. Sheasby and R. Pinner, *The Surface Treatment and Finishing of Aluminium and its alloys*, **1**, Finishing Publications Ltd., (2001).

176 O. Lunder, B. Olsen, and K. Nisancioglu, *International Journal of Adhesion & Adhesives,* **22**, 143-150 (2002).

177 O. Lunder, F. Lapique, B. Johnsen, and K. Nisancioglu, *International Journal of Adhesion & Adhesives,* **24**, 107-117 (2004).

178 K. J. H. Nelson, A. E. Hughes, R. J. Taylor, B. R. W. Hinton, L. Wilson, and M. Henderson, *Materials Science and Technology,* **17**, 1211-1221 (2001).

179 C. E. Moffitt, D. M. Wieliczka, and H. K. Yasuda, *Surface and Coatings Technology,* **137**, 188-196 (2001).

180 J. M. C. Mol, A. E. Hughes, B. R. W. Hinton, and S. van der Zwaag, *Corrosion Science,* **46**, 1201-1224 (2004).

181 B. Liu, *Surface cleaning of high strength aluminium alloys and its effect on fatigue*, The University of Birmingham, (2003).

182 O. Lunder and K. Nisancioglu, *Corrosion Science,* **44**, 414-422 (1988).

183 N. Dimitrov, J. A. Mann, and K. Sieradzki, *Journal of the Electrochemical Society,* **146**, 98-102 (1999).

184 E. V. Koroleva, G. E. Thompson, G. Hollrigl, G. Smith, and G. Flukes, in *Proc. 2nd Int. Symp. Aluminium Surface Science and Technology*, UMIST, Manchester, UK, p. 342-347, (2000).

185 A. E. Hughes, G. Theodossiou, S. Elliott, T. G. Harvey, P. R. Miller, J. D. Gorman, and P. J. K. Paterson, *Materials Science and Technology,* **17**, 1642-1652 (2001).

186 R. Borrelly, P. Merle, and D. Adenis, *Light Metals,* **1989**, 703-712 (1989).

187 C. S. Lin, C. C. Chang, and S. H. Hsieh, *Journal of the Electrochemical Society,* **147**, 3647-3653 (2000).

188 K. Nisancioglu, O. Lunder, and H. Holtan, *Corrosion,* **41**, 247-257 (1985).

189 M. G. Fontana, *Corrosion Engineering*, p. 39-139, McGraw-Hill, Inc., Singapore, (1987).

190 G. T. Burstein and S. P. Vines, *Journal of the Electrochemical Society,* **148**, B504-B516 (2001).

191 K. Sasaki and G. T. Burstein, *Corrosion Science,* **38**, 2111-2120 (1996).

192 A. P. Kayes, M. J. Robinson, and S. Impey, *The Journal of Corrosion Science and Engineering,* **2**, (1999).

193 A. Afseth, *Metallurgical Control of Filiform Corrosion of Aluminium Alloys*, Norwegian University of Science and Technology, (1999).

194 R. Ambat and A. J. Davenport, *Unpublished results*, The University of Birmingham, (2002).

195 R. V. Tilak, *Materials Science and Engineering,* **73**, 139-150 (1985).

196 R. E. Smallman and R. J. Bishop, *Modern Physical Metallurgy & Materials Engineering*, p. 224, Butterworth-Heinemann, Oxford, (1999).